



**Atomic Physics Modeling in Support of
Sandia Light Ion Beam Fusion Experiments**

J.J. MacFarlane, P. Wang, H.-K. Chung, G.A. Moses

July 1996

UWFDM-1033

***FUSION TECHNOLOGY INSTITUTE
UNIVERSITY OF WISCONSIN
MADISON WISCONSIN***

DISCLAIMER

This report was prepared as an account of work sponsored by an agency of the United States Government. Neither the United States Government, nor any agency thereof, nor any of their employees, makes any warranty, express or implied, or assumes any legal liability or responsibility for the accuracy, completeness, or usefulness of any information, apparatus, product, or process disclosed, or represents that its use would not infringe privately owned rights. Reference herein to any specific commercial product, process, or service by trade name, trademark, manufacturer, or otherwise, does not necessarily constitute or imply its endorsement, recommendation, or favoring by the United States Government or any agency thereof. The views and opinions of authors expressed herein do not necessarily state or reflect those of the United States Government or any agency thereof.

Atomic Physics Modeling in Support of Sandia Light Ion Beam Fusion Experiments

J. J. MacFarlane, P. Wang, H.-K. Chung, and G. A. Moses

Fusion Technology Institute
University of Wisconsin-Madison
1500 Engineering Drive
Madison, WI 53706

July 1996

UWFDM-1033

Contents

1. Introduction	1-1
2. Ionization Dynamics for Light Ion Transport Experiments	2-1
2.1. Collisional-Radiative Model for Transport Plasma Simulations	2-1
2.2. Calculation of Collisional Rates for Energetic Electrons	2-3
2.3. Investigation of Non-Thermal Particle Effects on Ionization Dynamics in High Current Density Ion Beam Transport Experiments	2-6
2.3.1. Introduction	2-6
2.3.2. Theoretical Models	2-7
2.3.3. Results	2-8
2.3.4. Summary	2-16
3. A Time-Dependent Collisional-Radiative Model for IPROP	3-1
4. Atomic Data Calculations	4-1
4.1. Dielectronic Recombination	4-2
4.2. Charge Exchange	4-5
5. A Unified Self-Consistent Model for Calculating Ion Stopping Powers in ICF Plasmas	5-1
5.1. Introduction	5-1
5.2. General Formalism of the Unified Ion Stopping Power Model	5-3
5.3. Electron Density Distributions in Plasmas	5-6
5.4. The Random-Phase-Approximation Stopping Interaction Function	5-9
5.5. Effective Charge Theory	5-15
5.6. Numerical Results	5-19
5.7. Analytic Fits	5-29
5.8. Summary	5-31

6. Analysis of K_α Satellite Emission Spectra	6-1
6.1. Improvements to Radiation-Hydrodynamics Modeling	6-1
6.2. Improvements to Collisional-Radiative Modeling	6-6
6.3. Simulation of PBFA-II Experiments	6-13
6.4. Absolute Flux Estimate for K_α Satellites	6-25

1. Introduction

In this report we summarize work performed at the University of Wisconsin Fusion Technology Institute in support of ion beam-plasma interaction experiments at Sandia National Laboratories during the period April 1995-June 1996. This work has focussed primarily on: (1) collisional-radiative and spectral modeling of moderate density plasmas; (2) calculation of basic atomic cross section data; (3) developing a “simple” time-dependent collisional-radiative model for the IPROP simulation code; (4) calculation of ion stopping powers, and (5) analysis of K_α satellite emission spectra.

The tasks for the April 1995-June 1996 period are listed in Table 1.1. The results of this work are discussed in the report as follows. In Section 2, we discuss model development and calculations to investigate atomic processes affecting the ionization dynamics and spectral properties of plasmas generated during light ion beam transport experiments. Calculations to date have focussed on Ar plasmas at densities relevant to the PBFA-II gas cell. This section also includes a paper presented at the 11th Topical Conference on High-Temperature Plasma Diagnostics in May 1996 (see Section 2.3).

In Section 3, a time-dependent collisional-radiative model developed for the IPROP transport code is described. Atomic physics cross section models and calculations are discussed in Section 4.

In Section 5, final results are presented from our calculation of ion stopping powers based on a finite-temperature random phase approximation model and a self-consistent treatment of the electron distribution. Finally, in Section 6 we describe recent work on the analysis of K_α spectra. Here, we also document several improvements and benchmarkings of both our radiation-hydrodynamics and collisional-radiative equilibrium codes.

Table 1.1. Tasks for April 1995–June 1996

-
1. Generate time-dependent atomic physics models for ion beam transport and supply relevant cross sections in a report.
 2. Help couple the atomic physics model into the IPROP transport code and assist in comparisons with experimental data.
 3. Develop a unified stopping power computer code based on the finite temperature RPA stopping power model and a self-consistent treatment of the electron distribution function.
 4. Calculate ion stopping powers for Li on Au and Al using the self-consistent unified stopping power model.
 5. Perform detailed CRE calculations to estimate the effects of heating of thin Al layers by Au radiation in flat-foil K_{α} experiments.
 6. Document results in a report to Sandia National Laboratories
-

2. Ionization Dynamics for Light Ion Transport Experiments

In this section we describe our modeling for ion beam transport plasmas. This work represents an extension of our previous CRE modeling in the following ways: (1) *time-dependent* multilevel atomic rate equations are solved to determine the atomic level populations; and (2) excitation and ionization by energetic (non-Maxwellian) electrons are considered.

The goals of this work are to develop a detailed understanding of the physical processes affecting the ionization dynamics of light ion transport plasmas. In addition, the spectral characteristics of these plasmas are being studied to determine which processes most affect the visible, VUV, XUV, and x-ray portions of the spectrum. The goal here is to identify spectral signatures which may help diagnose the properties of the various particle distributions (thermal electrons, energetic electrons, beam ions). Finally, our ionization dynamics calculations are being compared with IPROP ionization simulations in order to benchmark the codes.

In this section, the time-dependent collisional-radiative model used in studying ion beam transport plasmas is summarized (Section 2.1), followed by a description of the model used to compute energetic electron collisional rates. Section 2.3 contains a paper recently presented at the 11th Topical Conference on High-Temperature Plasma Diagnostics in Monterey, CA.

2.1. Collisional-Radiative Model for Transport Plasma Simulations

In our simulations of the ionization dynamics of transport plasmas, atomic level populations are calculated by solving a system of multilevel atomic rate equations of the form:

$$\frac{dn_i}{dt} = \sum_{j \neq i}^{N_L} n_j W_{ji} - n_i \sum_{j \neq i}^{N_L} W_{ij} \quad (i = 1, \dots, N_L) \quad (2.1)$$

where n_i is the number density of atoms (ions) in state i , W_{ij} is the transition rate for $i \rightarrow j$, and N_L is the total number of levels in the atomic model. To ensure mass conservation, one of the above equations (e.g., for $i = 1$) is replaced by the particle conservation equation

$$\frac{dn_i}{dt} = - \sum_{j \neq i} \frac{dn_j}{dt} \quad (2.2)$$

which assumes the number of atoms is fixed (i.e., $\sum_{i=1}^{N_L} n_i = N_{\text{tot}} = \text{constant}$). The initial state of the plasma must be specified by the user. For example, one could specify that all atoms are in the ground state of the neutral stage (a cold gas).

The processes included in the rate equations are:

- collisional excitation and ionization by thermal electrons, energetic electrons, and beam ions;
- collisional deexcitation by thermal electrons and energetic electrons;
- collisional, radiative, and dielectronic recombination by thermal electrons;
- spontaneous emission; and
- autoionization.

At present photon-induced processes are not included. Although it can be expected that photoionization is unimportant in the transport plasmas being considered, photoexcitation (resonant self-absorption) will be important for some transitions. It is anticipated that this effect will be included into our models in the near future.

The populating (W_{ji}) and depopulating (W_{ij}) rates in Eq. (2.1) are given by:

$$W_{lu} = n_e^0 C_{lu} + n_e^H \left(\frac{2}{m_e} \right)^{1/2} \int_{\Delta E_{ul}}^{\infty} \varepsilon^{1/2} \sigma_{lu}(\varepsilon) f(\varepsilon) d\varepsilon + J_B \sigma'_{lu}(E_B) \quad (2.3)$$

for excitation ($l < u$),

$$W_{ul} = n_e^0 C_{ul} + A_{ul} + n_e^H \left(\frac{2}{m_e} \right)^{1/2} \int_0^{\infty} \varepsilon^{1/2} \sigma_{ul}(\varepsilon) f(\varepsilon) d\varepsilon \quad (2.4)$$

for deexcitation ($u > l$),

$$W_{l\kappa} = n_e^0 C_{l\kappa} + n_e^H \left(\frac{2}{m_e} \right)^{1/2} \int_{\Delta E_{l\kappa}}^{\infty} \varepsilon^{1/2} \sigma_{l\kappa}(\varepsilon) f(\varepsilon) d\varepsilon + J_B \sigma'_{l\kappa}(E_B) + A_{l\kappa} \quad (2.5)$$

for ionization ($l < \kappa$), and

$$W_{\kappa l} = (n_e^0)^2 C_{\kappa l} + n_e^0 (\alpha_{\kappa l}^{RR} + \alpha_{\kappa l}^{DR}) \quad (2.6)$$

for recombination ($\kappa > l$). Quantities in the above equations are defined as:

ℓ	=	lower state index
u	=	upper state index
κ	=	continuum state index
n_e^0	=	density of thermalized electron component
n_e^H	=	density of hot (energetic) electrons
$C_{\ell u}$	=	collisional excitation rate coefficient
$C_{u\ell}$	=	collisional deexcitation rate coefficient
$A_{u\ell}$	=	spontaneous emission rate
$C_{\ell\kappa}$	=	collisional ionization rate coefficient
$C_{\kappa\ell}$	=	collisional (3-body) recombination rate coefficient
$\alpha_{\kappa\ell}^{RR}$	=	radiative recombination rate coefficient
$\alpha_{\kappa\ell}^{DR}$	=	dielectronic recombination rate coefficient
$A_{\ell\kappa}$	=	autoionization (Auger) rate
J_B	=	ion beam current density
σ'_{ij}	=	ion-impact excitation or ionization cross section at beam voltage E_B
$f(\varepsilon)$	=	distribution of non-Maxwellian (hot) electrons
σ_{ij}	=	electron-impact excitation or ionization cross section.

Note that the collisional rate coefficients (C_{ij}) are for a thermalized (Maxwellian) electron distribution. In practice, these are computed and tabulated as a function of the electron temperature prior to the collisional-radiative calculation.

A description of how collisional rates due to the non-Maxwellian electron component are computed is provided in the next section. Calculations of the other atomic parameters are described in Section 2.3.2 and Section 4.

2.2. Calculation of Collisional Rates for Energetic Electrons

Energetic electrons can significantly affect the ionization dynamics in ion beam transport plasmas. To treat non-Maxwellian electron distributions in our collisional-radiative simulations we use a hybrid electron model composed of a thermal (Maxwellian) component and a high energy tail. This approach is similar to that used in the IPROP simulation code. In our model, the energetic electron component affects the ionization dynamics through the following processes: collisional excitation and deexcitation, collisional ionization, and radiative recombination.

The collisional ionization rate is given by:

$$C_{\ell\kappa} = n_e^H \left(\frac{2}{m_e} \right)^{1/2} \int_{\Delta E_{\ell\kappa}}^{\infty} \varepsilon^{1/2} \sigma_{\ell\kappa}(\varepsilon) f(\varepsilon) d\varepsilon, \quad (2.7)$$

where the integral is over the kinetic energy of the incident electron and has a lower bound of $\Delta E_{\ell\kappa}$ (= ionization potential for the bound electron being ionized). The electron

distribution, $f(\varepsilon)$, is normalized such that

$$\int_0^\infty f(\varepsilon)d\varepsilon = 1. \quad (2.8)$$

For a Maxwellian distribution,

$$f(\varepsilon)d\varepsilon = 2\pi(\pi kT)^{-3/2}e^{-\varepsilon/kT}\varepsilon^{1/2}d\varepsilon, \quad (2.9)$$

where T is the electron temperature.

For the ionization cross section, we use the semi-empirical formula of Burgess and Chidichimo [7]:

$$\sigma_{i\kappa,j}(\varepsilon) = C'\xi_j \left(\frac{I_H}{I_j}\right)^2 \frac{\ln(x)}{x} W(x)(\pi a_0^2) \quad (2.10)$$

where $x \equiv \varepsilon/I_j$, I_j is the ionization potential for an electron in the j th subshell ($I_j = \Delta E_{i\kappa}$), ξ_j is the number of electrons in the j th subshell, a_0 is the Bohr radius, and I_H is the ionization potential of hydrogen (= 13.6 eV). The value of C' is finite and slowly varying for all ε . For argon ions, C' is taken to be 2.3. $W(x)$ is a function which provides a correction near the threshold region and is given by:

$$W(x) = [\ln(x)]^{\beta/x} \quad (x > 1) \quad (2.11)$$

where

$$\beta = \frac{1}{4} \left\{ \left[\frac{(100z + 91)}{(4z + 3)} \right]^{1/2} - 5 \right\}, \quad (2.12)$$

z is the charge state (e.g., $z = 0$ for neutrals). Note that $W(x < 1) = 0$.

The collisional excitation rate is given by Eq. (2.7), with an excitation cross section given by the Burgess and Summer formula [8]:

$$\sigma_{\ell u}(\varepsilon) = \frac{8\pi}{\sqrt{3}} \left(\frac{I_H}{\varepsilon}\right) \left(\frac{I_H}{\Delta E}\right) f_{\ell u} \bar{g}(\pi a_0^2), \quad (2.13)$$

where ΔE is the transition energy between the lower state (ℓ) and upper state (u), $f_{\ell u}$ is the oscillator strength, and \bar{g} is the effective Gaunt factor which accounts for near-threshold behavior.

The collisional deexcitation rate for a non-Maxwellian electron distribution is given by:

$$C_{u\ell} = n_e^H \left(\frac{2}{m_e}\right)^{1/2} \int_0^\infty \varepsilon^{1/2} \sigma_{u\ell}(\varepsilon) f(\varepsilon) d\varepsilon, \quad (2.14)$$

where $\sigma_{u\ell}(\varepsilon)$ is the deexcitation cross section. Note that unlike Eq. (2.7), the lower bound for this integral is zero. The deexcitation cross section is obtained from the “microreversibility” relation [12]:

$$\sigma_{u\ell}(\varepsilon) = \frac{G_\ell}{G_u} \left(\frac{\varepsilon + \Delta E}{\varepsilon} \right) \sigma_{\ell u}(\varepsilon + \Delta E), \quad (2.15)$$

where G_ℓ and G_u are the statistical weights of the lower and upper state configurations, respectively.

Note that the cross sections in Eq. (2.10) and (2.13) refer to the *configuration-averaged* cross sections. In more detailed atomic models which account for term splitting or fine structure splitting, the cross sections must be adjusted accordingly. This can be done using the relations:

$$\sigma_{\ell u}(\varepsilon) = \sigma_{LU}(\varepsilon) \frac{g_u}{G_U} \quad (2.16)$$

and

$$\sigma_{u\ell}(\varepsilon) = \sigma_{UL}(\varepsilon) \frac{g_\ell}{G_L}, \quad (2.17)$$

where upper case symbols refer to configuration-averaged values and lower case symbols refer to “fine structure” values. Note that

$$G_L = \sum_{\ell \ni L} g_\ell \quad \text{and} \quad G_U = \sum_{u \ni U} g_u, \quad (2.18)$$

where the sums are over all fine structure levels (u or ℓ) within a configuration (U or L). Note also that for the excitation rate this is automatically accounted for when using the fine structure oscillator strength, $f_{\ell u}$ (see Eq. 2.13).

The cross section for radiative recombination in a non-Maxwellian distribution can be obtained from the Milne formula:

$$\sigma_{\kappa i}(\varepsilon) = \frac{g_i}{g_\kappa} \frac{h^2 \nu^2}{2m_e c^2} \frac{1}{\varepsilon} \sigma_{i\kappa}(\nu) \quad (2.19)$$

where $h\nu = \varepsilon + I_j$ is the photon energy, ε is the kinetic energy of the incident electron, and $\sigma_{i\kappa}(\nu)$ is the photoionization cross section.

2.3. Investigation of Non-Thermal Particle Effects on Ionization Dynamics in High Current Density Ion Beam Transport Experiments

H.-K. Chung, J. J. MacFarlane, P. Wang, and G. A. Moses (Fusion Technology Institute); J. E. Bailey, C. L. Olson (Sandia National Laboratories); D. R. Welch (Mission Research Corporation)

Abstract

Light ion inertial fusion experiments require the presence of a moderate density background gas in the transport region to provide charge and current neutralization for a high current density ion beam. In this paper, we investigate the effects of non-thermal particles such as beam ions or non-Maxwellian electron distributions on the ionization dynamics of the background gas. In particular, we focus on the case of Li beams being transported in an argon gas. Non-thermal particles as well as thermal electrons are included in time-dependent collisional-radiative calculations to determine time-dependent atomic level populations and charge state distributions in a beam-produced plasma. We also briefly discuss the effects of beam ions and energetic electrons on the visible and VUV spectral regions. It is found that the mean charge state of the gas, and hence the electron density, is significantly increased by collisions with energetic particles. This higher ionization significantly impacts the VUV spectral region, where numerous resonance lines occur. On the other hand, the visible spectrum tends to be less affected because the closely spaced excited states are populated by lower energy thermal electrons.

2.3.1. Introduction

In light ion beam transport experiments, high energy, high current beam ions ionize a background gas during the transport towards a target. The beam space charge is partly or completely neutralized by the electrons from the gas, and the beam current is partly or completely neutralized by an induced plasma return current [1]. During the breakdown process, energetic electrons are produced from ion impact ionization collisions with gas atoms, knock-on collisions of beam ions with free electrons, and by free electrons being accelerated by electric fields. These non-Maxwellian electrons are predicted to form a hot electron “halo” around the beam, which leads to an increase in plasma conductivity and return current fraction *outside* the beams; this results in higher *net* currents inside the beam channel [2]. It is predicted that the thermalization of these energetic electrons through electron-electron and electron-neutral collisions is sufficiently slow that about 1% of the free electrons reside in a high energy tail. Since the evolution of the plasma conductivity

is dependent on the ionization state of the gas, an improved understanding of the physics of ion beam transport can be achieved by studying ionization dynamics, or breakdown physics, of the background gas.

In this paper, we consider the case of Li ion beams incident on an Ar gas. Visible spectra resulting from transitions between excited states of Ar II have been measured in PBFA-II gas cell beam transport experiments [3]. These data have been used to infer the temperature of the relatively cold, “thermal” component of the free electron distribution. The purpose of this current study is to understand the effects of energetic electrons and Li beam ions on the ionization dynamics of these moderate-density Ar plasmas. To do this, we use a time-dependent collisional radiative model which includes collisional excitation and ionization effects due to energetic electrons, Li beam ions, and thermal electrons. The implications for spectroscopic diagnostics are also briefly addressed.

2.3.2. Theoretical Models

In our time-dependent collisional-radiative (CR) model, ionization and excitation populations are computed by solving multilevel atomic rate equations. The population of each atomic level is determined by computing collisional and radiative transition rates between each level. The ionization and recombination processes considered are: collisional ionization by thermal electrons, Li beam ions and energetic electrons; three-body recombination by thermal electrons; and radiative recombination by thermal and energetic electrons. Three-body recombination by energetic electrons is neglected since energetic particles are less important for the three-body recombination processes [4]. Inner-shell ionization and autoionization processes are included since energetic particles can induce such processes even in a low electron temperature plasma. The excitation and deexcitation processes considered in our calculations are: collisional excitation and deexcitation by thermal and non-thermal electrons, and spontaneous radiative decay. At present, photoexcitation and photoionization are neglected in our calculations. Although photoionization for the Ar gas cell plasmas discussed here should be unimportant, photoexcitation due to resonant self-absorption could lead to lower effective spontaneous decay rates. This will be explored in future calculations.

The rate coefficients for collisional and radiative processes involving thermal electrons and ion beam particles have been described elsewhere [5,6]. The energetic electron collisional excitation and ionization rate coefficients are obtained by integrating collisional cross-sections taken from semi-empirical formulae [7,8]. The form of the energetic electron energy distribution function (which is based on results from particle-in-cell simulations)

is assumed to be inversely proportional to electron energy. Particle-in-cell simulations will give more detailed form of the energetic electron distribution function for our future study. The total number of energetic electrons is taken to be 1% of thermal electrons. The non-thermal electron collisional excitation cross-sections and radiative recombination cross-sections are obtained, respectively, from collisional ionization and photoionization cross-sections by reciprocity relations [9]. The corresponding rate coefficients are computed by integrating the cross-sections with the energetic electron energy function. In our time-dependent collisional-radiative calculations, 270 atomic levels distributed over 7 ionization stages from Ar I to Ar VII are considered. A configuration averaged atomic model is used in determining populations and charge state distributions. Separate calculations based on a fine-structure atomic model are used to compute spectra. Calculated spectra include contributions from bound-bound, bound-free, and free-free transitions. Opacity effects are included in the spectral calculations. Voigt profiles are used for line profiles.

The plasma and beam conditions used in our calculations are as follows. We assume a constant thermal electron temperature of 3 eV. The 9 MeV Li ion beam current increases linearly with time to 20 kA/cm² at 18 ns, and then abruptly falls to zero. The thermal electron density is determined from the effective charge state of the Ar gas, which is updated via the time-dependent collisional-radiative equations. The energetic electron density is assumed to be 1% of the thermal electron density during the beam rise time. The argon gas has a density of 7×10^{16} ions/cm³ (2 torr at room temperature), and at $t = 0$ the electron density is assumed to be equal to the ion density.

2.3.3. Results

First we investigate the effects of energetic particles on collisional rates. The collisional rates considered are an ionization transition from Ar II (singly ionized argon) ground state to Ar III (doubly ionized) ground state, and an excitation transition between Ar II 4p and Ar II 4s (see Figure 2.1(a) and (b)). The transition between Ar II 4p and Ar II 4s was selected since line emission from transitions of this type have been observed in PBFA-II experiments.

At the low temperatures typical of experimental conditions ($T \sim 3$ eV), energetic particles provide the dominant source of ionization for large energy transitions. Ionization and excitation due to the energetic electron component exceeds that of the low temperature Maxwellian component for $\Delta E \gtrsim 20$ eV transitions because relatively few particles in the $T = 3$ eV Maxwellian tail have energies greater than the threshold energy. On the other hand, for small ΔE transitions (e.g., 4s \rightarrow 4p) a large fraction of the low temperature

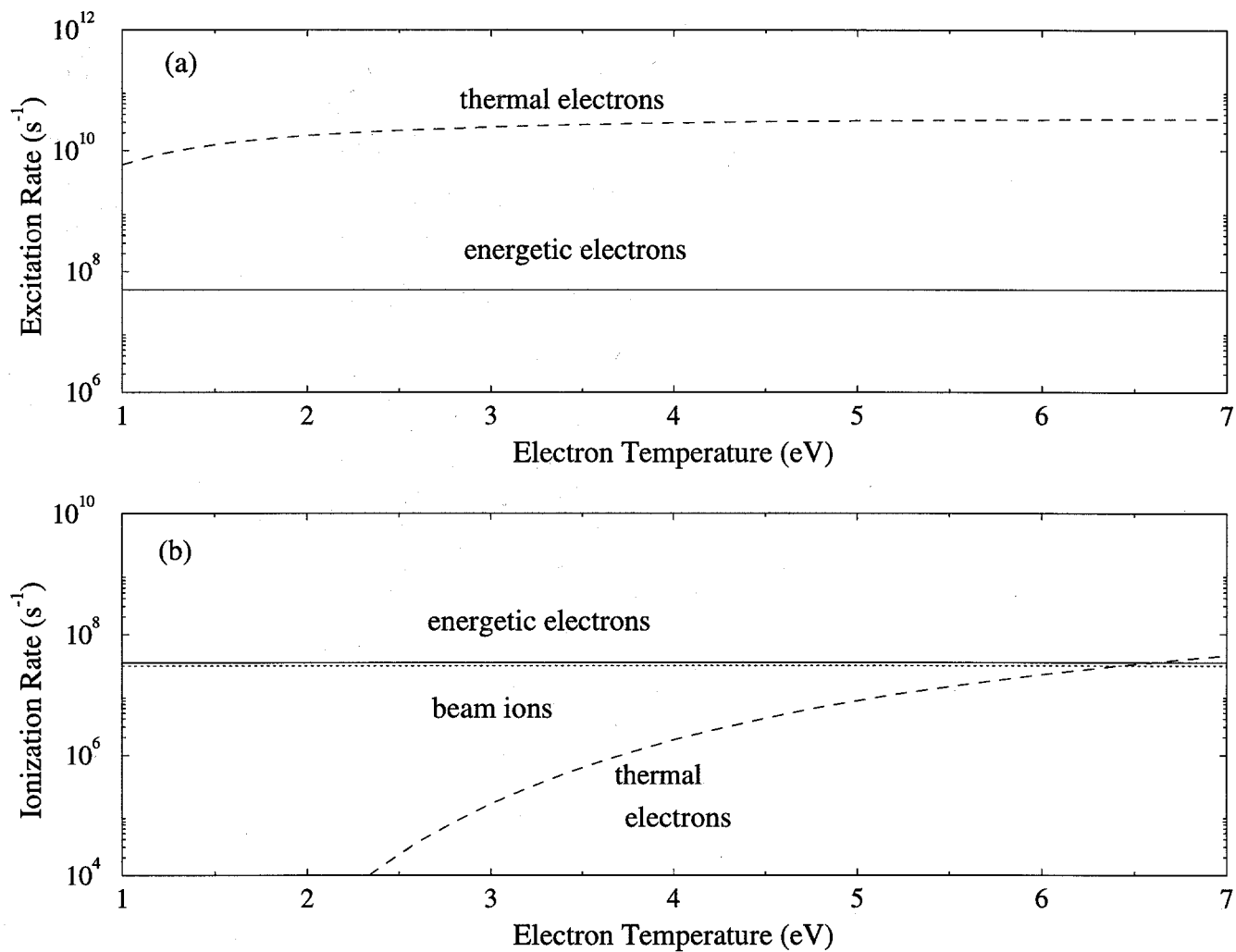


Figure 2.1. Ionization and excitation rate coefficients for thermal electrons, Li beam ions and energetic electrons plotted as a function of electron temperature : (a) excitation between Ar II 4p and 4s states ($\Delta E = 2.7$ eV) (b) ionization between Ar II ground state and Ar III ground state ($\Delta E = 27.7$ eV). Solid line: energetic electron rate. Dotted line: Li beam ion rate. Dashed line: thermal electron rate.

Maxwellian electrons can participate in the excitation process. Thus, since there are significantly more electrons in the low temperature component of our model, excitation and deexcitation in small ΔE transitions (which produce lines in the visible or UV portion of the spectrum) are driven by the thermal electron component.

Due to high excitation and ionization rates for high-energy transitions, beam ions and non-thermal electrons populate high-lying levels. In Figure 2.2, the population ratio of Ar II 4p to Ar II 4s levels and the ratio of the Ar II ground state to Ar III ground state are shown as a function of time. The population ratios are scaled to their Local Thermodynamic Equilibrium (LTE) values. The LTE population ratios between two levels are based on an electron temperature of 3 eV and an electron density of $7 \times 10^{16} \text{ cm}^{-3}$. If the ratio $f(\text{CR})/f(\text{LTE})$ is unity, the collisional processes are in a detailed balance between the two levels. Figure 2.2 shows that the relative populations of the two ground states eventually reach a steady-state ratio in which the Ar II is slightly enhanced relative to its LTE value. On the other hand, the relative populations of two excited states, which have a small transition energy, equilibrate very quickly and maintain an LTE ratio. This results from the fact that excitation processes have such a transition energy comparable to or smaller than the electron temperature, and that a detailed balance between collisional processes is established between the two levels in a very short time by thermal electrons. The equilibration time scale for these excited states is $\sim 10^{-11} \text{ s}$.

It should be noted that the energetic particles do not significantly affect the relative populations of the two excited states of a low transition energy [10]. However, the energetic particles do play a significant role in larger ΔE transitions. The fact that energetic particles do not cause the relative populations between two closely spaced excited states to deviate significantly from their LTE value has implications for visible spectral measurements. For instance, a Boltzmann plot analysis can be used to infer the temperature of the thermal component of the electron distribution [11].

We next present the results of four simulations which illustrate the effects of energetic particles on the mean charge state of the Ar plasma. Case A refers to a calculation which includes contributions from thermal electrons, Li beam ions, and non-thermal electrons on the Ar ionization dynamics. Case B neglects Li beam ions, but includes thermal and energetic electrons. Case C neglects energetic electrons, but includes thermal electrons and Li beam ions. Case D includes only thermal electrons. For each case, the thermal electron temperature is assumed to be constant at 3 eV and the initial thermal electron density is assumed to correspond to the ion density ($n_e^{\text{cold}} = 7 \times 10^{16} \text{ cm}^{-3}$); that is, all populations are in Ar II ground state at $t = 0$. Thus, the calculations provide insight into the processes

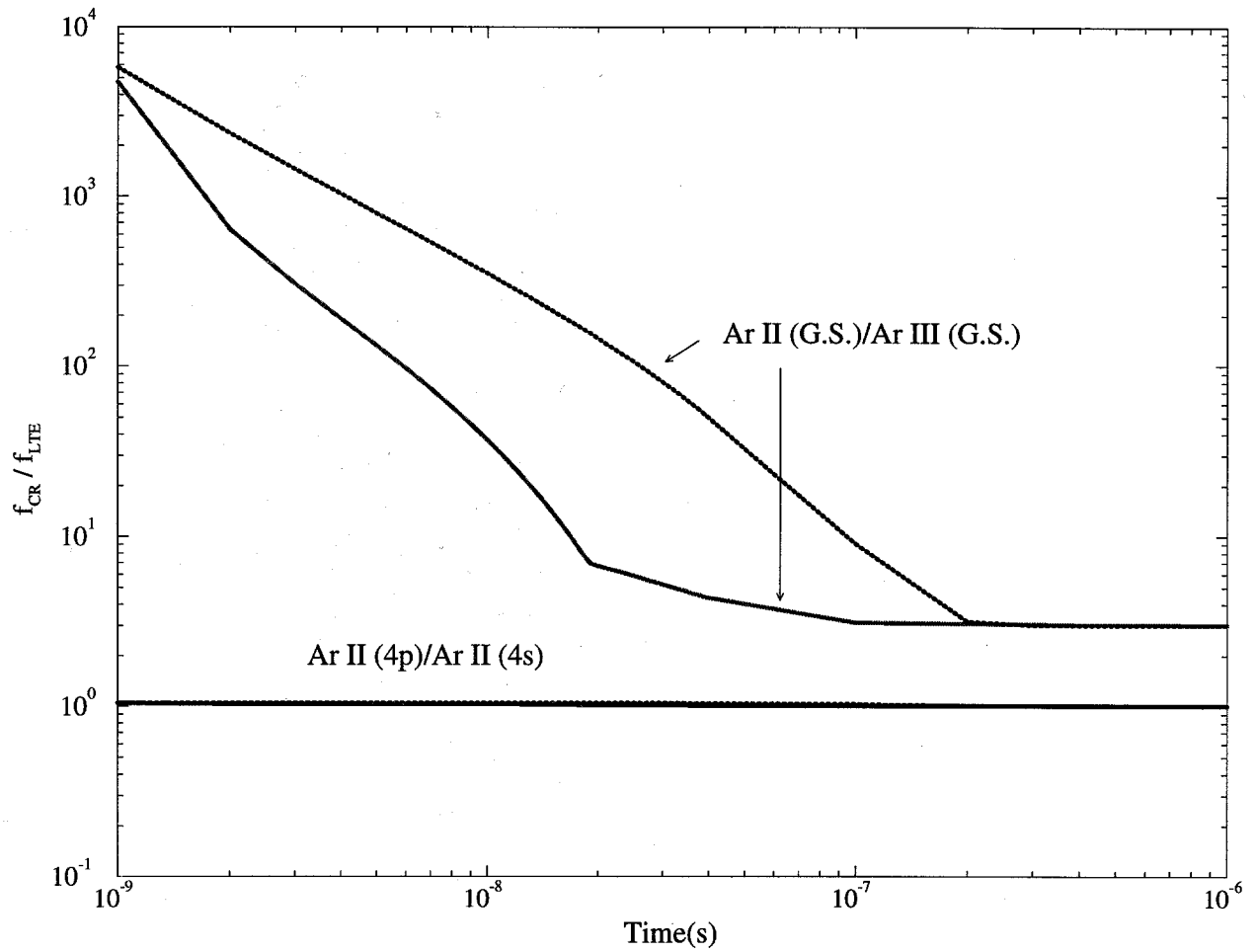


Figure 2.2. Population ratios for Ar II 4p to 4s ($\Delta E = 2.7$ eV) and for the Ar II ground state to Ar III ground state ($\Delta E = 27.7$ eV). Both ratios are scaled to their LTE values. Solid line: the case in which energetic particles are included for the first 18 ns. Dotted line: without energetic particles.

which affect the growth of the electron density after it has become partially ionized. The Li ion beam and energetic electrons are assumed to rise linearly between $t = 0$ and 18 ns, and then abruptly falls to zero. Figure 2.3 shows that the energetic particles can significantly affect the mean charge state. At 18 ns where the Li beam current and non-thermal electron density reach their peak value, the mean charge state for case A differs from the value for case D by a factor of two. For this particular set of plasma and beam conditions, the energetic electrons are seen to be more effective than the Li beam ions in ionizing the singly ionized Argon gas. After the energetic particle pulse is removed at 18 ns, the mean charge state for case A stays near its peak value before going into a recombining stage. The mean charge state for case D, however, continues to increase before reaching its steady state value. These results clearly indicate that energetic particle effects play a key role in affecting the ionization dynamics of these moderate-density transport plasmas.

It is of interest to investigate the implications of the above results for spectral diagnostics. Figures 2.4 and 2.5 show how energetic particles can affect the visible and VUV spectral region. The visible spectrum results from small ΔE transitions is shown and, as stated above, is more influenced by thermal electrons. The energetic particles can affect the spectrum in the sense that they influence the absolute population of the excited states, but not their relative populations. Absolute fluxes of many visible lines are close to Planck function-limited values of πB_ν . This is due to the fact that: (1) the upper and the lower levels of the transition are in LTE with respect to each other; and (2) optical depths for the line cores exceed unity for both cases A and D. It should be noted that if these two conditions are not met, the absolute intensities for the two cases would not necessarily be similar as they are in Figure 2.4.

In the VUV region, where resonance lines are prominent, the line spectrum can be very significantly affected by energetic particles. Several VUV lines are identified in Figure 2.5 as coming from high ionization stages such as Ar III, IV or even V when energetic particles are included in the calculation. In simulations which neglect energetic particles, emission lines from the relatively high ionization stages of Ar are not seen. Thus, either emission or absorption spectroscopic measurements could provide valuable information on the ionization dynamics of these transport plasmas. We are also presently investigating whether EUV and x-ray spectral lines resulting from inner-shell transitions can be used to diagnose energetic particle characteristics. This work will be presented elsewhere.

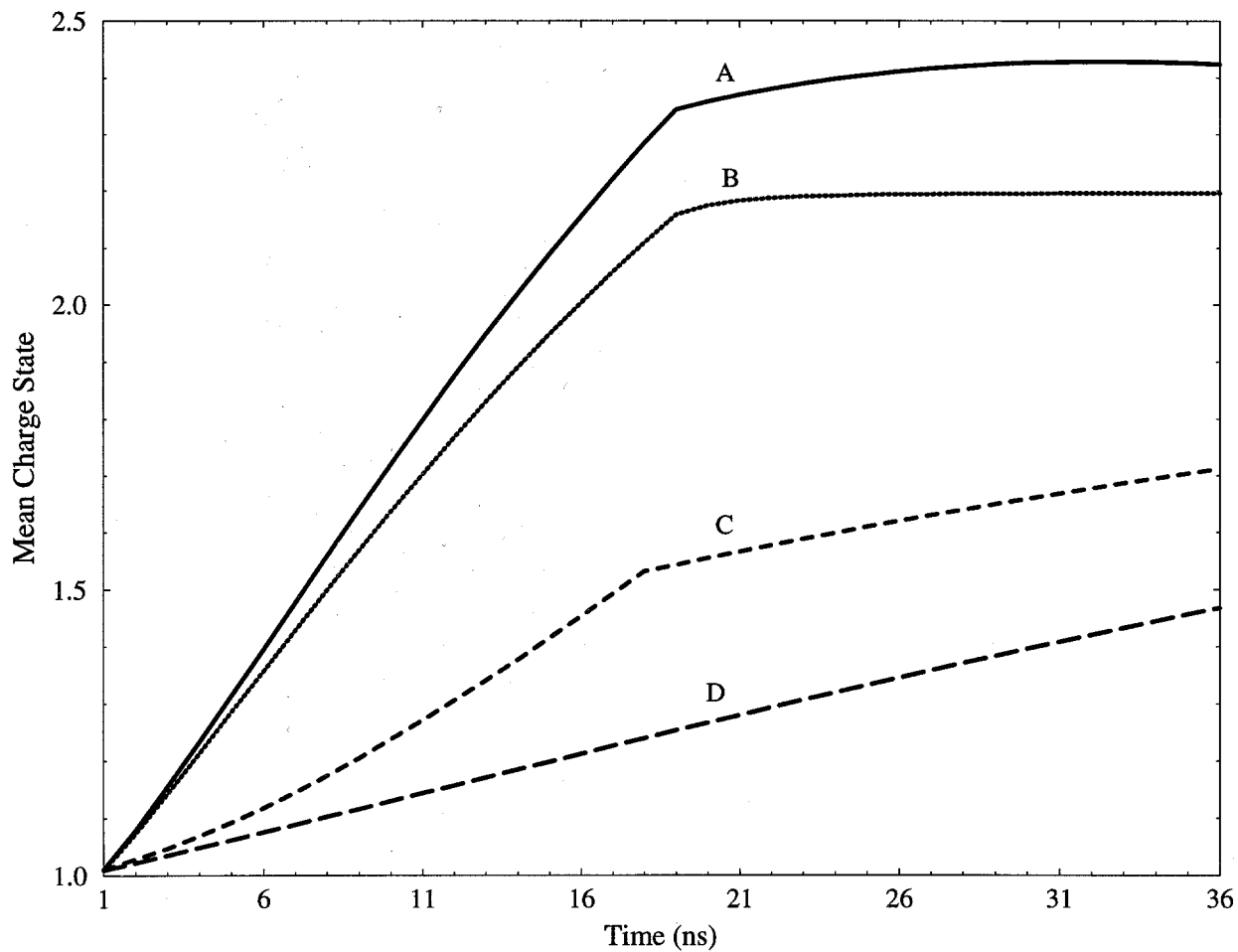


Figure 2.3. Mean charge state is plotted as a function of time for 4 cases. (A) Includes all energetic particles, Li beam and energetic electrons. (B) Includes energetic electrons but no beam ions. (C) Includes Li beam without energetic electrons. (D) Includes no energetic particles.

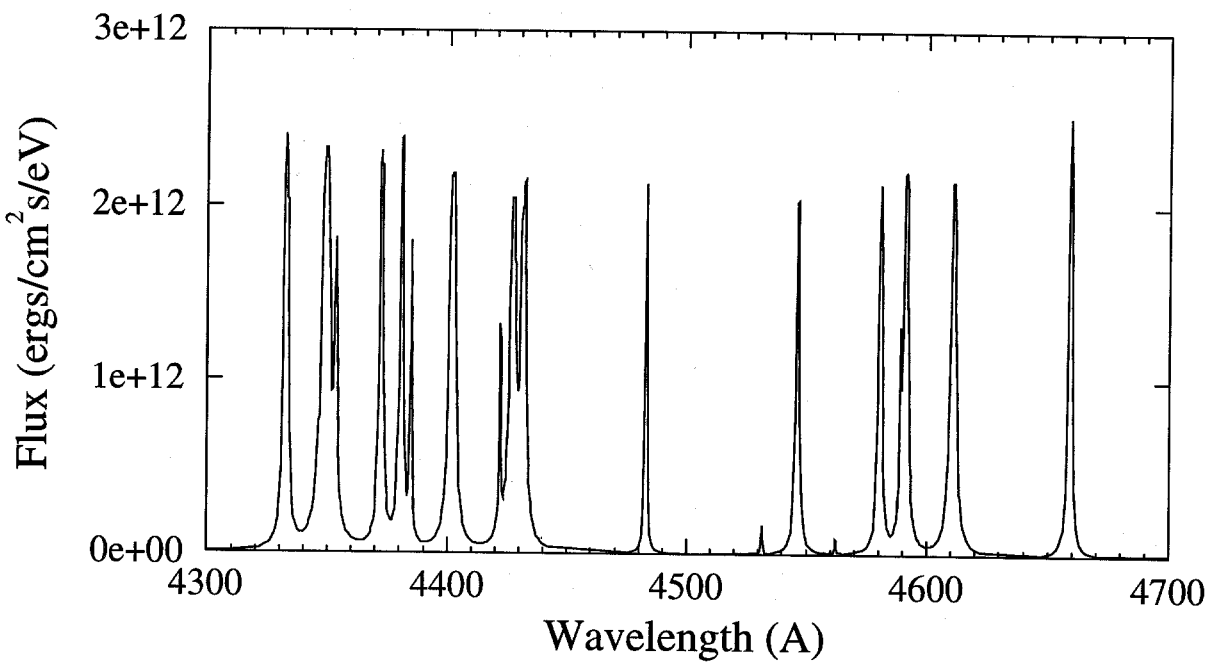
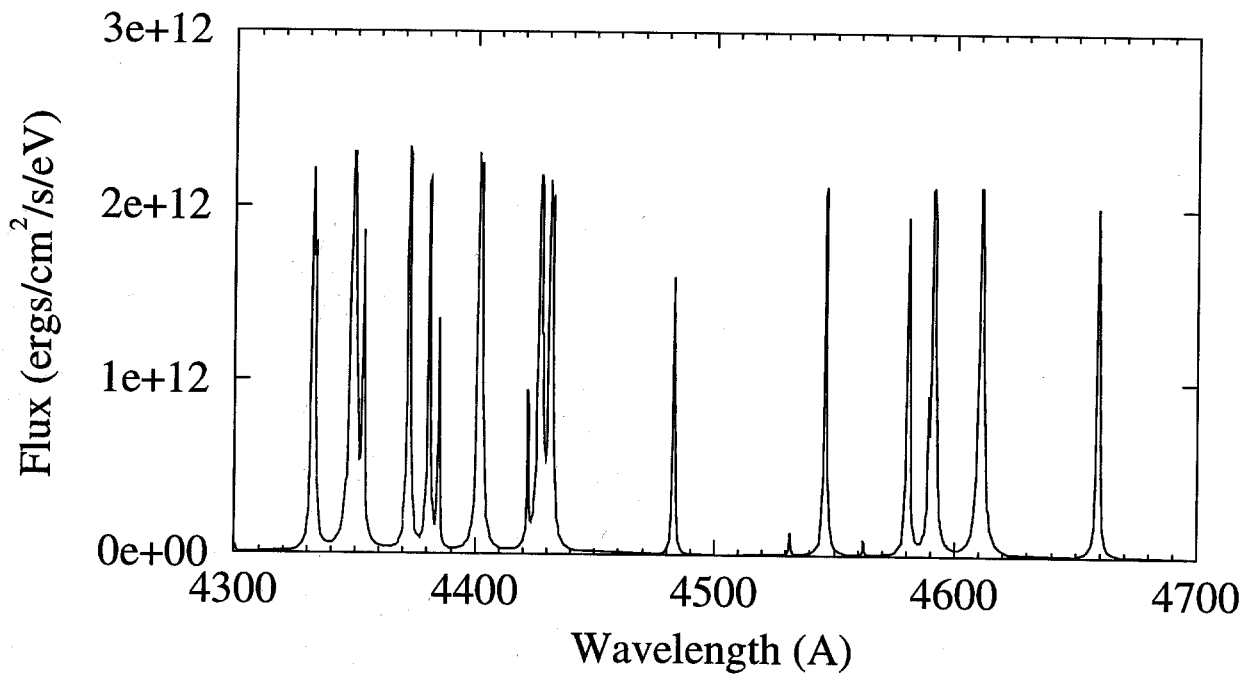


Figure 2.4. Visible spectra at 18 ns for Case A (top) where energetic particles are included; Case D (bottom) where no energetic particles are included.

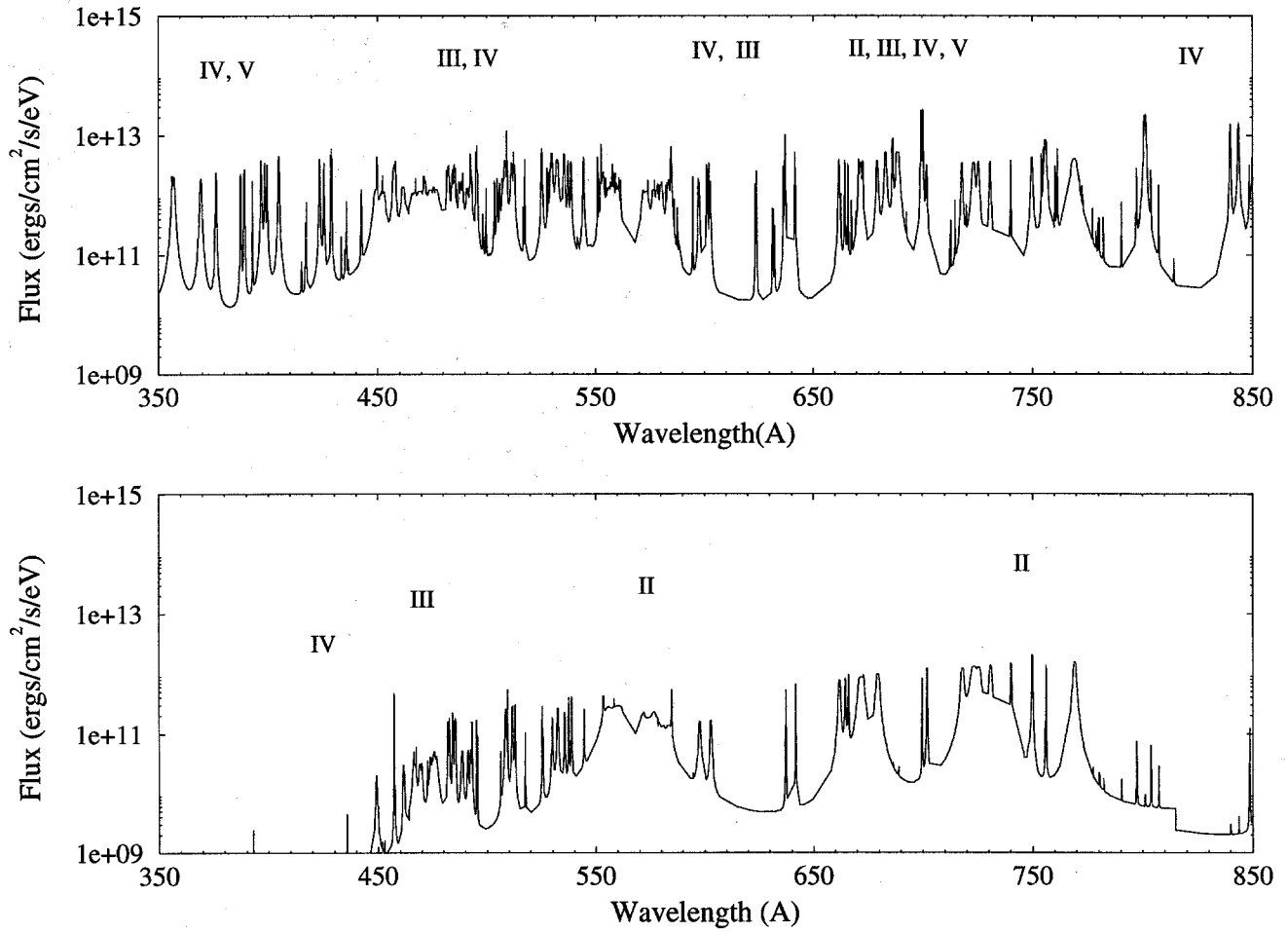


Figure 2.5. VUV spectral region at 18 ns for Case A (top) and Case D (bottom). Several of the argon lines are identified by their ionization stage.

2.3.4. Summary

Time-dependent collisional-radiative calculations have been performed to investigate the effects of Li beam ions and energetic electrons on the ionization dynamics of light ion beam transport plasmas. We find that energetic particles play a significant role in affecting the ionization dynamics, leading to a higher charge state and a higher electron density in the background plasma. We have also briefly investigated the role of energetic particles in affecting the visible and VUV spectral regions. We find the visible transitions are strongly influenced by thermal electrons, while energetic particles can significantly affect the VUV spectral region.

References for Section 2

1. J. A. Sweigle and S. A. Slutz, *J. Appl. Phys.* **60**, 3444 (1986).
2. D. R. Welch, C. L. Olson and T. W. L. Sanford, *Phys. Plasmas* **1**, 763 (1994).
3. J. E. Bailey, A. L. Carlson, D. J. Johnson, E. J. McGuire, T. Nash, C. L. Olson, J. J. MacFarlane, and P. Wang, 9th International Conference on High Power Particle Beams, Washington D.C., p. 903 (1992).
4. J. P. Matte, J. C. Kieffer, S. Ethier, M. Chaker, and O. Peyrusse, *Phy. Rev. Lett.* **72**, 1208 (1994).
5. J. J. MacFarlane, P. Wang, J. Bailey, T. A. Mehlhorn, and R. J. Dukart, and R. C. Mancini, *Phys. Rev. E* **47**, 2748 (1993).
6. P. Wang, "ATBASE User's Guide," Univ. of Wisconsin Fusion Technology Institute Report UWFD-942 (December 1993).
7. A. Burgess, and M. C. Chidichimo, *Mon. Not. R. Astr. Soc.* **203**, 1269 (1982).
8. A. Burgess, and H. P. Summers, *Mon. Not. R. Astr. Soc.* **174**, 345 (1976).
9. I. I. Sobelman, L. S. Vainshtein and E. A. Yukov, *Excitation of Atoms and Broadening of Spectral Lines*, Springer-Verlag, NY (1981).
10. R. Jayakumar and H. H. Fleischmann, *J. Quant. Spectrosc. Radiat. Transfer* **33**, 177 (1985).
11. J. E. Bailey, et al., presented at the Seventh International Workshop on Atomic Physics for Ion-Driven Fusion, Madrid, Spain (October 1995).
12. Lamoureux, M., "Atomic Physics and Non-Maxwellian Plasmas," in *Advances in Atomic, Molecular, and Optical Physics*, Vol. 31, p. 233 (1993).

3. A Time-Dependent Collisional-Radiative Model for IPROP

A “simple” time-dependent collisional-radiative model has been developed for IPROP. It is based on models from both NLTERT [1], the CRE code used in our analysis of K_α satellite spectra, and models developed to study the ionization dynamics of transport plasmas [2]. It is simple in the sense that: (1) the atomic physics is based on a “local” approximation; that is, the state of a plasma mass element depends only on the history of its own *local* electron temperature and density and ion beam flux, but is not coupled to other parts of the plasma (by radiation-induced processes, for example); (2) photoexcitation and photoionization are presently neglected, although a resonance self-absorption model based on a local approximation could be added if warranted; and (3) emergent spectra are not calculated. Although the model is being set up to handle an arbitrary number of energy levels (up to $\sim 10^3$), it is anticipated that within IPROP a relatively small number ($\lesssim 100$) of atomic energy levels will be used. This is typically done by using configuration-averaged levels, as opposed to term-split or fine structure atomic level models.

This model is currently being implemented within IPROP. Substantial progress was made during a recent visit by Dale Welch to the University of Wisconsin. The interface has been developed in a manner such that additional improvements in the atomic modeling can be readily incorporated into IPROP.

Below, we provide a description of the processes included in the collisional-radiative model. Atomic cross section data utilized by the model is described in Sections 2 and 4 of this report.

The atomic level populations are calculated from the set of coupled atomic rate equations of the form shown in Eqs. (2.1) through (2.19). Atomic processes considered in the model include:

- collisional excitation and ionization by thermal electrons, energetic electrons and beam ions
- collisional deexcitation by thermal and energetic electrons
- collisional (3-body) recombination by thermal electrons
- spontaneous emission
- radiative and dielectronic recombination
- autoionization.

It is anticipated that IPROP should be able to fully utilize this model within the next several months. Computational timing studies should be performed to determine the extent to which the C-R model increases the overall simulation time of IPROP, particularly when using large atomic models. This will provide guidance on whether less detailed models should be used, or whether one can use more sophisticated atomic modeling.

References for Section 3

1. MacFarlane, J.J., "NLTERT – A Code for Computing the Radiative Properties of Non-LTE Plasma," University of Wisconsin Fusion Technology Institute Report UWFD-930.
2. Chung, H.K., MacFarlane, J.J., Wang, P., Moses, G.A., Bailey, J.E., Olson, C.L., and Welch, D.R., "Investigation of Non-Thermal Particle Effects on Ionization Dynamics in High Current Density Ion Beam Transport Experiments," Review of Scientific Instruments, in press (1996).

4. Atomic Data Calculations

In this section, we summarize some of the atomic data calculations for basic atomic processes occurring in transport plasmas. In particular, this section focuses on dielectronic recombination and charge exchange.

The first practical problem one will face in atomic model setup is how to specify atomic level structure for a specific problem. The analysis of atomic spectroscopy diagnostics requires a detailed specific classification of the level structure of ions (e.g., LS or LSJ resolution), whereas to cope with the very many excited states participating in plasma ionization equilibrium calculations necessitates a less detailed viewpoint (for example nl or even a ‘bundle- n ’ average). In our atomic models, fine-structure (LSJ) is resolved for those levels principally responsible for the dominant spectral lines which can provide potential diagnostic information; term structure (LS) is used for levels which are not responsible for important spectral lines, but strongly couple to the relevant transition levels; configuration average structure (nl) is used for levels which can have an important effect on the ionization distribution and are necessary for providing a reasonable representation of radiation energy balance; and finally, hydrogenic structure is used for a few high levels to represent a large number of highly excited states.

For IPROP it is expected that a small set of configuration-averaged (nl) levels will be used to represent the lower levels and hydrogenic levels to represent higher excited levels. The accuracy of this kind of simple atomic model depends on the calculations of the corresponding average quantities, i.e., average energies, average oscillator strengths, and average radiative and collisional cross sections. In our calculations, a configuration-interaction approach with Hartree-Fock wavefunctions is used to calculate the baseline data (e.g., energy levels, oscillator strengths, and photoionization cross sections). These baseline data are fine-structure resolved and quite accurate. From these baseline data, we evaluate the corresponding average quantities with the use of the standard sum rules [1].

The background theory and the methods for our calculations of electron impact excitation/deexcitation, electron impact ionization/recombination, radiative recombination, ion impact excitation/ionization have been described elsewhere [2]. In the following we outline the new features of our calculations of rate coefficients for dielectronic recombination and charge exchange.

4.1. Dielectronic Recombination

A dielectronic recombination is the reaction



where $E_i + \varepsilon = E_{j,nl} = E_k + \hbar\omega$. The initial state of the recombining ion X^{Z+1} is denoted i and is called the ‘‘target state’’. Target states whose populations are of sufficient abundance in a plasma to be relevant starting points for recombination events only include the ground state of the $Z + 1$ ion and a few of the lowest metastable states. For a low density plasma, where the electron collisional stabilization process is not important, the dielectronic recombination rate coefficient for the reaction from the initial state X_i^{Z+1} to the final state X_k^{+Z} can be evaluated from the Auger transition probability $A_{j,nl}^a$ and the radiative transition probability $A_{j,nl \rightarrow k}^r$:

$$\alpha^{DR}(i \rightarrow k) = \frac{4\pi^{3/2}a_0^3}{T^{3/2}} \sum_d \left[\frac{g_d e^{-E_{di}/kT} A_{d \rightarrow i}^a \frac{A_{d \rightarrow R}^r}{\sum_{i'} A_{d \rightarrow i'}^a + \sum_{k'} A_{d \rightarrow k'}^r}}{g_i} \right] \quad (4.2)$$

where d denotes all possible autoionizing states connecting the initial target state i and the final stabilization state k , $E_{di} = E_d - E_i = \varepsilon$ is the kinetic energy of the recombining electron, and g_i and g_d are the statistical weights of the state X_i^{Z+1} and $X_d^Z(j, nl)$, respectively. Both the temperature and energy are in rydbergs and a_0 is the Bohr radius. In our previous calculations an approximate Burgess-Merts formula [3] is used:

$$\begin{aligned} \alpha^{DR}(i) &= \sum_k \alpha^{DR}(i \rightarrow k) \\ &= 4.8 \times 10^{-11} \frac{B(z)}{T^{3/2}} \sum_{j=i+1}^{n_t} \bar{f}_{ij} A(x) e^{-E_s^\infty/aT} \quad (\text{cm}^3/\text{s}), \end{aligned} \quad (4.3)$$

where E_s^∞ and T are in rydbergs, with $E_s^\infty = E_j - E_i$

$$z = Z - N + 1, \quad x = E_s^\infty/(z + 1), \quad B(z) = z^{1/2}(z + 1)^{5/2}/(z^2 + 13.4)^{1/2},$$

$$A(x) = \begin{cases} X^{1/2}/(1 + 0.105X + 0.015X^2) & \Delta n = 0 \\ 0.5X^{1/2}/(1 + 0.210X + 0.030X^2) & \Delta n > 0 \end{cases}$$

and

$$a = 1.0 + 0.015z^3/(z + 1)^2.$$

The summation over j is to be carried out from the minimum energetically allowed value n_0 up to a value n_t at which the highly excited nl electron is collisionally ionized faster than it decays radiatively. The value of n_t can be estimated from the expression

$$n_t^7 = 5.6 \times 10^{17} Z^6 T^{1/2} / n_e,$$

where n_e is the electron density in cm^{-3} . Although the Burgess-Merts formula has been widely used in many CRE calculations, it is very difficult to assess its accuracy for a specific application. The Burgess-Merts formula only represents the total rate coefficient and does not indicate how the total should be split up into n or nl -shell components. To achieve this, we have developed a program starting from first principles to calculate dielectronic recombination rate coefficients.

In our new calculations, we start from Eq. (4.2) which defines the rate coefficient $\alpha^{DR}(i \rightarrow k)$. The major effort of doing such detailed calculations is to calculate a large number of autoionization rates $A_{d-i'}^a$ and radiative decay rates $A_{d-k'}^r$. We calculate fine-structure resolved autoionization and radiative decay rates for doubly excited levels up to principal quantum number $n = 6$ for isoelectronic systems of Na-like to He-like. For example, for a Li-like system, Table 4.1 lists the autoionization configurations considered explicitly in a DR calculation:

Table 4.1.

Target states:	$1s^2 2s^1$	$1s^2 2p^1$	$1s^2 3s^1$	$1s^2 3p^1$
Autoionization states:	$1s^2 3s^2$	$1s^2 3s^1 4s^1$	$1s^2 3s^1 5s^1$	$1s^2 3s^1 6s^1$
	$1s^2 3s^1 3p^1$	$1s^2 3s^1 4p^1$	$1s^2 3s^1 5p^1$	$1s^2 3s^1 6p^1$
	$1s^2 3s^1 3d^1$	$1s^2 3s^1 4d^1$	$1s^2 3s^1 5d^1$	$1s^2 3s^1 6d^1$
		$1s^2 3s^1 4f^1$	$1s^2 3s^1 5f^1$	$1s^2 3s^1 6f^1$
			$1s^2 3s^1 5g^1$	$1s^2 3s^1 6g^1$
		$1s^2 3p^1 4s^1$	$1s^2 3p^1 5s^1$	$1s^2 3p^1 6s^1$
	$1s^2 3p^2$	$1s^2 3p^1 4p^1$	$1s^2 3p^1 5p^1$	$1s^2 3p^1 6p^1$
	$1s^2 3p^1 3d^1$	$1s^2 3p^1 4d^1$	$1s^2 3p^1 5d^1$	$1s^2 3p^1 6d^1$
		$1s^2 3p^1 4f^1$	$1s^2 3p^1 5f^1$	$1s^2 3p^1 6f^1$
			$1s^2 3p^1 5g^1$	$1s^2 3p^1 6g^1$
		$1s^2 3d^1 4s^1$	$1s^2 3d^1 5s^1$	$1s^2 3d^1 6s^1$
		$1s^2 3d^1 4p^1$	$1s^2 3d^1 5p^1$	$1s^2 3d^1 6p^1$
	$1s^2 3d^2$	$1s^2 3d^1 4d^1$	$1s^2 3d^1 5d^1$	$1s^2 3d^1 6d^1$
		$1s^2 3d^1 4f^1$	$1s^2 3d^1 5f^1$	$1s^2 3d^1 6f^1$
			$1s^2 3d^1 5g^1$	$1s^2 3d^1 6g^1$

Autoionization states (cont.):		$1s^2 4s^2$	$1s^2 4s^1 5s^1$	$1s^2 4s^1 6s^1$
		$1s^2 4s^1 4p^1$	$1s^2 4s^1 5p^1$	$1s^2 4s^1 6p^1$
		$1s^2 4s^1 4d^1$	$1s^2 4s^1 5d^1$	$1s^2 4s^1 6d^1$
		$1s^2 4s^1 4f^1$	$1s^2 4s^1 5f^1$	$1s^2 4s^1 6f^1$
			$1s^2 4s^1 5g^1$	$1s^2 4s^1 6g^1$
			$1s^2 4p^1 5s^1$	$1s^2 4p^1 6s^1$
		$1s^2 4p^2$	$1s^2 4p^1 5p^1$	$1s^2 4p^1 6p^1$
		$1s^2 4p^1 4d^1$	$1s^2 4p^1 5d^1$	$1s^2 4p^1 6d^1$
		$1s^2 4p^1 4f^1$	$1s^2 4p^1 5f^1$	$1s^2 4p^1 6f^1$
			$1s^2 4p^1 5g^1$	$1s^2 4p^1 6g^1$
			$1s^2 4d^1 5s^1$	$1s^2 4d^1 6s^1$
			$1s^2 4d^1 5p^1$	$1s^2 4d^1 6p^1$
		$1s^2 4d^2$	$1s^2 4d^1 5d^1$	$1s^2 4d^1 6d^1$
		$1s^2 4d^1 4f^1$	$1s^2 4d^1 5f^1$	$1s^2 4d^1 6f^1$
			$1s^2 4d^1 5g^1$	$1s^2 4d^1 6g^1$
			$1s^2 4f^1 5s^1$	$1s^2 4f^1 6s^1$
			$1s^2 4f^1 5p^1$	$1s^2 4f^1 6p^1$
			$1s^2 4f^1 5d^1$	$1s^2 4f^1 6d^1$
		$1s^2 4f^2$	$1s^2 4f^1 5f^1$	$1s^2 4f^1 6f^1$
			$1s^2 4f^1 5g^1$	$1s^2 4f^1 6g^1$
			$1s^2 5s^2$	$1s^2 5s^1 6s^1$
			$1s^2 5s^1 5p^1$	$1s^2 5s^1 6p^1$
			$1s^2 5s^1 5d^1$	$1s^2 5s^1 6d^1$
			$1s^2 5s^1 5f^1$	$1s^2 5s^1 6f^1$
		$1s^2 5s^1 5g^1$	$1s^2 5s^1 6g^1$	
		$1s^2 5p^1$	$1s^2 5p^1 6s^1$	
		$1s^2 5p^1 5d^1$	$1s^2 5p^1 6p^1$	
		$1s^2 5p^1 5f^1$	$1s^2 5p^1 6d^1$	
		$1s^2 5p^1 5g^1$	$1s^2 5p^1 6f^1$	
			$1s^2 5p^1 6g^1$	
			$1s^2 5d^1 6s^1$	
			$1s^2 5d^1 6p^1$	
		$1s^2 5d^2$	$1s^2 5d^1 6d^1$	
		$1s^2 5d^1 5f^1$	$1s^2 5d^1 6f^1$	
		$1s^2 5d^1 5g^1$	$1s^2 5d^1 6g^1$	

Final stabilization states:	$1s^2 2s^1 2p^1$	$1s^2 2s^1 3s^1$	$1s^2 2s^1 3p^1$	$1s^2 2s^1 3d^1$
	$1s^2 2s^1 4s^1$	$1s^2 2s^1 4p^1$	$1s^2 2s^1 4d^1$	$1s^2 2s^1 4f^1$
	$1s^2 2s^1 5s^1$	$1s^2 2s^1 5p^1$	$1s^2 2s^1 5d^1$	$1s^2 2s^1 5f^1$
	$1s^2 2s^1 6s^1$	$1s^2 2s^1 6p^1$	$1s^2 2s^1 6d^1$	
	$1s^2 2p^2$	$1s^2 2p^1 2s^1$	$1s^2 2p^1 3p^1$	$1s^2 2p^1 4s^1$

It should be noted that the ground configuration of Be-like systems cannot directly couple to the Li-like ion through the dielectronic recombination reaction in the two-step process model.

For the autoionization states with principal quantum number $n > 6$, we use the following formula to estimate their contribution to the total rate coefficient:

$$\sum_{n_2=n_c}^{\infty} \alpha^{DR}(n_2) \simeq \frac{\alpha^{DR}(n_c - 1)}{2} n_c \left(\frac{n_c - 1}{n_1} \right)^3 \left(1 + \frac{1}{n_c} + \frac{1}{2n_c^2} \right),$$

where n_c has the value of 7 in our calculations, and n_1 and n_2 are the principal quantum numbers in autoionization configurations of type

$$\text{Core} + (n_1 l_1)(n_2 l_2).$$

For the higher excited target states (e.g., $1s^2 4p^1$, $1s^2 5s^1$, etc.), their contribution to the dielectronic recombination is very small. We use the Burgess-Merts formula to estimate the rate coefficients when necessary. We believe that our new calculations for dielectronic recombination rate coefficients are more accurate and can be used for better atomic spectroscopy modeling for ICF related plasmas.

4.2. Charge Exchange

A charge exchange process is the reaction



in which an electron goes from the atom A to the ion B^{z+1} .

In IPROP, the concern is with charge exchange capture by beam ions for ground and excited states of neutral species in the background. Considering that the relative velocity of the colliding particles, i.e., beam ions and background atoms, will not be very low, perturbation theory can be used. In the framework of perturbation theory, the velocity dependence of the charge-exchange cross section is given by the Brinkman-Kramers formula [4]:

$$\alpha(n_a l_a^N - n) = \pi a_0^2 \frac{2^8 \eta}{5} N \frac{(2I)^{5/2} (2I_n)^{5/2} n^2}{f(v)} \left(\frac{v_0}{v} \right)^2, \quad (4.5)$$

where $\eta = 1/3$, N is the number of electrons in the $n_a l_a$ shell of the neutral atom, I is the ionization potential of the shell $n_a l_a$, n is the principal quantum number of a level of ion B^{+z} with the corresponding ionization potential of $I_n = Z^2/2n^2$, $v_0 = e^2/h$ is the atomic unit of velocity, and v is the relative velocity. The function $f(v)$ is given by

$$f(v) \left\{ \left[\left(\frac{v_0}{v} \right) \Delta I + \frac{1}{2} \left(\frac{v_0}{v} \right) \right]^2 + 2I_n \right\}^5 \quad (4.6)$$

where $\Delta I = I - I_n$.

At low velocities, the cross section decreases more rapidly than follows from Eq. (4.5); in fact, exponential decrease occurs:

$$\sigma(n_a l_a^n - n) = \pi a_0^2 N \frac{\pi^2}{8\gamma^2} \exp \left[-\frac{\pi \Delta I v_0}{2\gamma v} \right] \quad (4.7)$$

where

$$\gamma = \frac{1}{2} \left\{ \sqrt{N2I + \frac{1}{4} \left(\frac{v}{v_0} \right)^2} + \sqrt{2I_n + \frac{1}{4} \left(\frac{v}{v_0} \right)^2} \right\}. \quad (4.8)$$

Combining Eq. (4.5) and Eq. (4.7), we have

$$\sigma(n_a l_a^N - n) = \begin{cases} \pi a_0^2 \frac{n^8 \eta}{5} N \frac{(2I)^{5/2} (2I_n)^{5/2} n^2}{f(v)} \left(\frac{v_n}{v} \right)^2 & v > v_c \\ \pi a_0^2 \frac{\pi^2}{8\gamma} N \exp \left[-\frac{\pi \Delta I v_0}{2\gamma v} \right] & v \leq v_c \end{cases}$$

where V_c is determined from $\sigma_{\text{high}}(v_c) = \sigma_{\text{low}}(v_c)$.

The total charge-exchange cross section can be obtained by summing $\sigma(n_a l_a^N - n)$ over all $n_a l_a$ and n :

$$\sigma_{cx}(v) = \sum_{(n_a l_a)} \sum_n \sigma(n_a l_a^N - n).$$

References for Section 4

1. Cowan, R.D., "The Theory of Atomic Structure and Spectra," University of California Press, Berkeley, 1981.
2. Wang, P., Ph.D. Dissertation, Dept. of Nuclear Engineering and Engineering Physics, University of Wisconsin-Madison, 1991.
3. Merts, A.L., Cowan, R.D., and Megee, N.H., Jr., Los Alamos Scientific Laboratory Report LA-6220-MS, March 1976.
4. Sobelman, I.I., Vainstein, L.A., and Yukov, E.A., "Excitation of Atoms and Broadening of Spectral Lines," Springer-Verlag, New York, 1981.

5. A Unified Self-Consistent Model for Calculating Ion Stopping Powers in ICF Plasmas

P. Wang and T. A. Mehlhorn

Abstract

We have developed a new unified self-consistent ion stopping power model for use in ion-driven inertial confinement fusion (ICF) target design. This model includes sophisticated treatments for the electron density distribution of an atom in plasmas and a full Random Phase Approximation stopping function which extrapolates the zero temperature Lindhard stopping function to arbitrary temperatures. We have shown that this model provides accurate ion stopping powers for cold materials, including both low-Z and high-Z elements. For finite temperature plasmas, the model accounts for the stopping effects due to electrons in ground states, excited states, resonance states and continuum states in a self-consistent manner. There is no separate treatment for “bound” and “free” electrons. Hence, our approach allows for ion stopping powers to be calculated using a single unified model over a wide range of beam and target conditions relevant to ICF studies.

5.1. Introduction

For many years, the stopping of energetic ions in matter has been a subject of great interest. In the context of ion driven inertial confinement fusion (ICF) experiments, the stopping power of ions in matter of both solid and plasma states is crucial for target designs. For reliable diagnostics and evaluation of ion beam and target parameters such as beam intensity, target temperature, and density, one must know the stopping power accurately. Comprehensive reviews of calculations and measurements of ion stopping power in ICF targets have been well documented [1-4].

For typical plasma conditions in ion beam-target interaction experiments, the target plasmas are often only partially ionized. Both bound and free electrons make contributions to the stopping power. The most commonly used approach for calculating ion stopping power in partially ionized plasmas is to divide the stopping electrons into two groups: those bound to the plasma ions and those which constitute the plasma free electrons. The number of free electrons in the plasma is determined by solving the Saha equation. The contribution of each group of electrons to the stopping power is calculated separately. For example, most of the stopping power calculations [1,3,5] use the Bethe equation [6] for the bound electrons and use a separate term for the plasma free electrons. Although this kind of combined stopping power model has provided a reasonably accurate description of the

energy deposition of both light and heavy ions in ICF plasmas, one significant weakness is that the combined stopping power models abruptly switch electrons from “bound” states to “free” states with the use of a quantum treatment for bound electrons and a statistical model for the free electrons. Because of the complexity of the calculation, most of the combined models make the further assumption that all the bound electrons are in their ground states.

The response of the strongly bound orbital electrons to the ion projectiles is different from that of the free plasma electrons. The models which abruptly switch an electron from “bound” states to “free” states may produce undesirable discontinuities in the results of stopping power as a function of target temperature and density. In fact, for an ion in the plasma the transition between “bound” and “free” states is physically continuous. One can represent the effect of the plasma by a fluctuating microfield; the perturbations of this microfield to the bound states can cause an orbital electron to have some nonzero probability of becoming unbound from its original nucleus. However, an electron which is unbound in a one-center system may still be bound in a two-center system consisting of the original nucleus and a neighboring ion. Moreover, the electron may also be bound in a 3,4,..., center system which includes additional neighboring ions. Such complexes have lifetimes on the order of the mean interionic distance divided by mean thermal ion speed, which is long enough for electronic energy to be well specified, although adiabatically varying in time. A relevant discussion of these quasi-free electrons has been given by More [7], who makes use of formal collision theory to describe these electrons in terms of “shape resonance” in the short-range effective potentials arising from neighboring particles. More studied this problem within the framework of the ion-sphere model which is appropriate for atomic systems in plasmas at the conditions of our interest. In ion stopping power calculations, these quasi-free electrons should be treated properly because they provide a smooth interpolation between strongly bound orbital electrons and freely moving plasma electrons.

Another drawback of the combined stopping power models is that they use different models for different ion velocity regimes, and the separation boundary of “low” and “high” velocity regimes is usually somewhat ambiguous.

For better understanding of ion stopping power in ICF plasmas, it is necessary to make more precise treatment of electronic stopping. We describe a unified ion stopping power model which treats the “bound” and “free” target electrons in a self-consistent manner. We present the model in detail, describe the computational implementation, and give a detailed and critical evaluation of the calculation results.

5.2. General Formalism of the Unified Ion Stopping Power Model

The dielectric formulation of ion stopping theory pioneered by Lindhard and his associates [8,9,10] combined with the local density approximation [11] has proven to be a powerful and flexible tool for ion stopping power calculations. Our model is developed within this framework.

A charged particle passing through an ionized medium will induce an electric field by polarizing the medium. The induced electric field will then act back on the particle, resisting its motion, and cause it to lose energy. This induced electric field can be related to the dielectric function $\varepsilon(k, \omega)$ of the medium through its Fourier transform. For a fast ion with charge $Z_1 e$ moving in a straight line in the x direction with velocity V , the stopping power dE/dx is given by

$$\frac{dE}{dx} = -\frac{4\pi}{m} \left(\frac{Z_1 e^2}{V} \right)^2 \rho L(\rho, V), \quad (5.1)$$

where ρ and m denote, respectively, the electron density and the electron mass, and L is the stopping function which is related to the dielectric function $\varepsilon(k, \omega)$ through

$$L(\rho, V) = \frac{i}{\pi \omega_0^2} \int_0^\infty \frac{dk}{k} \int_{-kV}^{kV} \omega d\omega \left[\frac{1}{\varepsilon(k, \omega)} - 1 \right], \quad (5.2)$$

where ω_0 is the plasma frequency, i.e.,

$$\omega_0^2 = \frac{4\pi e^2 \rho}{m}. \quad (5.3)$$

Eq. (1) can be extended to calculate the stopping power of a nonuniform electron cloud with the use of the local density approximation [11]. In the local-density approximation, the nonuniform electron cloud is divided into small independent volume elements, and the electron density distribution in each volume element is assumed to be uniform. The stopping power is calculated for a charged particle in a free electron gas of each volume element's density, and the final stopping power is computed by averaging over these values, weighted by their distribution in the nonuniform electron cloud:

$$\left(\frac{dE}{dx} \right) = -\frac{4\pi}{m} \left(\frac{Z e^2}{V} \right)^2 \int_0^\infty \rho(r) L(\rho, V) 4\pi r^2 dr, \quad (5.4)$$

where $\rho(r)$ is the radial electron density distribution function of the stopping medium.

Since the stopping medium of interest are solids and partially ionized plasmas, because of atomic shell structure, the spatial variation of electron distribution is very

dramatic. It is therefore necessary to examine the assumption that the local density approximation is applicable for these targets. Consider a fast charged particle with velocity V passing through a nonuniform electron gas with a spatial distribution function $\rho(r)$. The spatial variation of the electron gas is determined by

$$\frac{\rho(r)}{|d\rho(r)/dr|}. \quad (5.5)$$

Then the interaction between the charged particle and the “local” electron gas can be characterized by the effective interaction time

$$T_{eff} = \frac{\rho(r)}{|d\rho(r)/dr|} \frac{1}{V}. \quad (5.6)$$

On the other hand, the plasma oscillation causes an intrinsic variation of the electron density distribution which is characterized by the plasma frequency $\omega_0 = (4\pi\rho(r)e^2/m_e)^{1/2}$. This intrinsic variation is *seen* by the incident charged particle in both uniform and nonuniform electron gases in the time scale of $1/\omega_0$. If the effective interaction time between the incident charged particle and “local” electrons in a target with nonuniform electron density distribution is smaller than the local plasma oscillation period, then the local density approximation is applicable for such a target. Figure 5.1 shows the comparison of these two parameters for a proton with various energies passing through a gold target. The radial charge density profile of a gold atom is also shown at the top of the figure. Note that the wave feature in the curves of the effective interaction time and plasma oscillation period result from the shell structure in the electron density profile. We see that for protons with energies above 1 MeV, the effective interaction times are always smaller than the local plasma oscillation period. For protons with lower energies, the effective interaction time becomes larger than the local plasma oscillation period in the interior region because of the extreme large density gradient. This means that the local density approximation may not be appropriate for slow ions at this region. However, it is known that the slow ions are largely stopped by the outer region of electrons where the condition $T_{eff} < \omega_0^{-1}$ is always true. We therefore use the local density approximation in the development of our stopping power model.

To develop a unified model for electronic stopping, the stopping power in general is

$$\left(\frac{dE}{dx}\right) = -\frac{4\pi}{m} \left(\frac{Ze^2}{V}\right)^2 \int_0^\infty \rho(T, N, r) L(T, \rho, V) 4\pi r^2 dr, \quad (5.7)$$

where T and N denote, respectively, the temperature and particle number density of the target, V is the projectile velocity, ρ is the electron density function of the target, and L is a

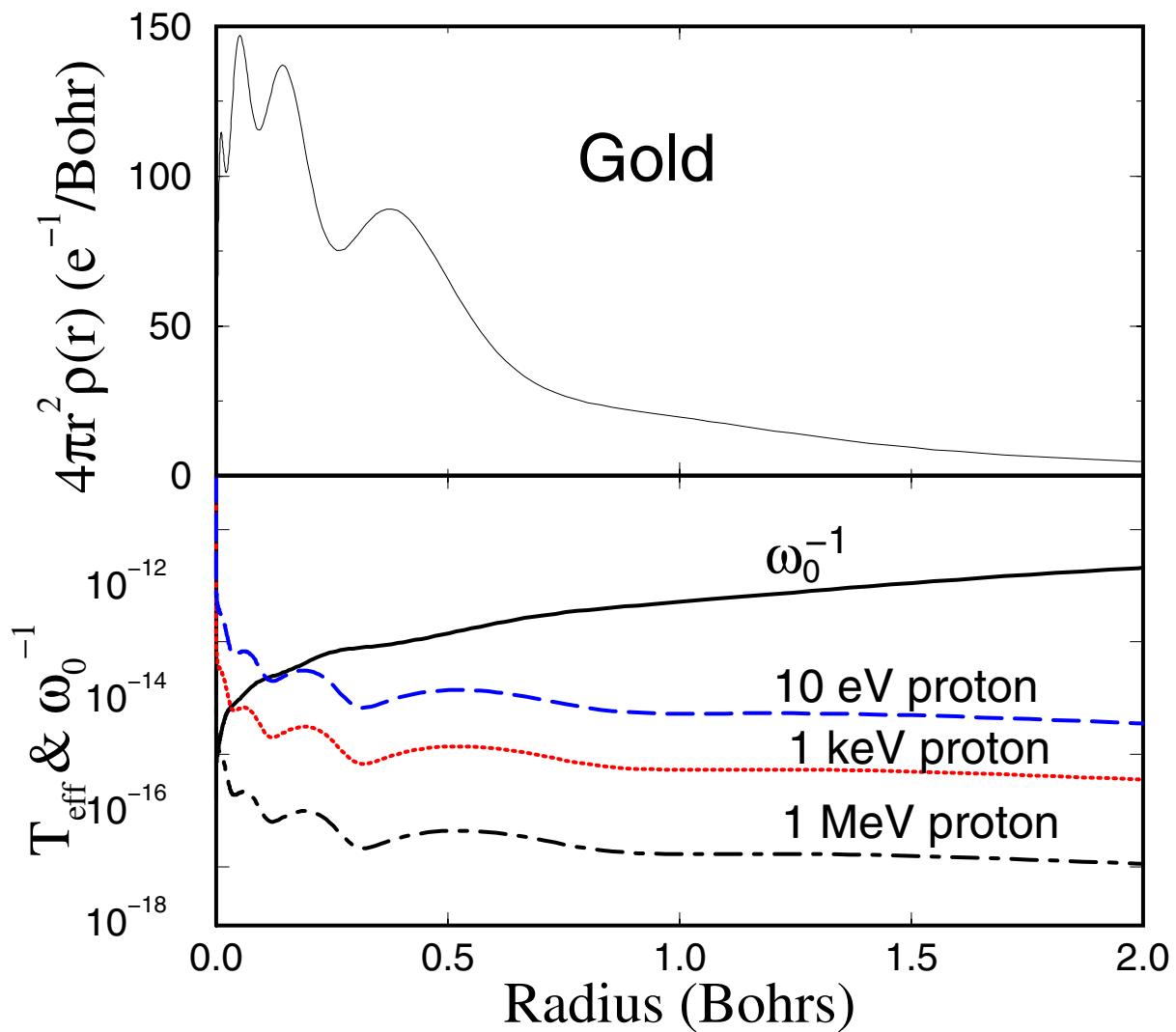


Figure 5.1. Comparison of the local plasma oscillation period and the effective interaction times for the interaction of a proton and a cold gold target. (Top) Radial electron density profile for neutral gold atom. (Bottom) The corresponding local plasma oscillation period and the effective interaction times for protons with three different energies.

generalized stopping function which is temperature dependent. Using this general formula as a starting point, our present work is concerned with establishing two main points.

The first main point is how to choose an atomic model with which we can determine the electron density distribution accurately over a wide range of temperature and density conditions relevant to ion-driven inertial confinement fusion targets. The conventional isolated atom Hartree-Fock model has been widely used to calculate electron density distributions for various purposes, but its results are feasible only for low density plasmas. The self-consistent-field (SCF) band-structure model [12,13] can provide a very accurate electron density distribution for solids. However, because of its complexity, this model is rather difficult to extend to high-Z materials (where relativity plays an important role) and to finite temperatures. In 1979 Liberman developed a self-consistent-field “atom-in-jellium” model [14] to study atomic properties in high temperature and high density plasmas. This model has much of the simplicity of an isolated atom but captures much of the physics of the band-structure model. More importantly, it provides a self-consistent treatment for both “bound” and “free” electrons in finite temperature plasma conditions. Its accuracy and simplicity make it attractive for large scale calculations of electron density distributions for materials containing either low- or high-Z atoms and either zero- or finite temperatures. We therefore choose this atomic model to determine the electron density distribution for ICF targets of our interest.

The second main point of this work concerns the stopping characteristics of pointlike and nonrelativistic positive ions with arbitrary velocity in ICF targets at any temperature. Here we take advantage of the exact Random Phase Approximation (RPA) dielectric function developed by Maynard and Deutsch [15], which is not constrained by projectile velocities and target temperatures.

5.3. Electron Density Distributions in Plasmas

In a partially ionized plasma, the electron density distribution function, $\rho(r)$, is determined by summing over electron population densities in a strongly bound ground state, loosely bound excited states, quasi-free resonance states, and free states. In the “atom-in-jellium” model, electrons in all these different states are treated in a self-consistent manner. The transition between localized bound states and freely moving continuum states is smoothly continuous.

The schematic illustration of the “atom-in-jellium” model [14] is given in Figure 5.2, where the atom is represented as a point nucleus embedded in a spherical cavity in a continuous background positive charge. The cavity radius R is determined either by the

matter density ($\rho = 3M/4\pi R^3$, where $M =$ atomic mass) or by other physical considerations (e.g., chemical potential). There are sufficient electrons to neutralize both the nucleus and the surrounding positive charge. Electrical neutrality is also required inside the atomic cavity. Outside the cavity, a “muffin-tin” approximation is used, i.e., the electron density is replaced with its volume average in all potential-energy expressions.

The electrons are governed by a set of self-consistent-field one-electron Dirac equations:

$$[c\vec{\alpha} \cdot \vec{p} + \beta c^2 - c^2 + V(r)] \phi_i(\vec{r}) = \epsilon_i \phi_i(\vec{r}), \quad (5.8)$$

where $\phi_i(\vec{r})$ is the normalized one-electron orbital function, ϵ_i is the energy eigenvalue, and $V(r)$ is the potential function which can be expressed as

$$V(r) = \begin{cases} -\frac{Z}{r} + \int_{r' < R} \frac{\rho(r')}{|\vec{r} - \vec{r}'|} - \frac{[3\pi^2 \rho(r)]^{1/3}}{\pi} - \nu & r < R \\ -\frac{(3\pi^2 \bar{\rho})^{1/3}}{\pi} & r > R, \end{cases} \quad (5.9)$$

where the Lagrangian multiplier ν is given by

$$\nu = \left\{ \left[4 - \frac{\bar{\rho}}{\rho(R)} \right] (3\pi^2 \bar{\rho})^{1/3} - 3[3\pi^2 \rho(R)]^{1/3} \right\} / 4\pi. \quad (5.10)$$

The electron density itself is given in terms of normalized one-electron orbital functions and the muffin-tin approximation:

$$\rho(r) = \begin{cases} \frac{\int \rho_-(\vec{r}) \sin \theta d\theta d\varphi}{4\pi} & r < R \\ \frac{\int_{x>R} \rho_-(\vec{x}) d\vec{x}}{\int_{x>R} d\vec{x}} = \bar{\rho} & r > R \end{cases} \quad (5.11)$$

$$\rho_-(\vec{r}) = \sum_i n_i |\phi_i(\vec{r})|^2.$$

The orbital occupation number, n_i , is determined by the Fermi-Dirac distribution function:

$$n_i = \frac{1}{\exp \left[\frac{(\epsilon_i - \mu)}{kT} \right] + 1}, \quad (5.12)$$

where μ is the chemical potential of the plasma. The sum in Eq. (11) includes electrons in ground states, excited states, and an integral over the continuum.

Figure 5.3 shows the calculated electron radial density profiles for aluminum at room temperature and various densities. Also shown are the SCF band-structure calculation [13] result at normal density and the isolated atom Hartree-Fock (HF) result. We note that the

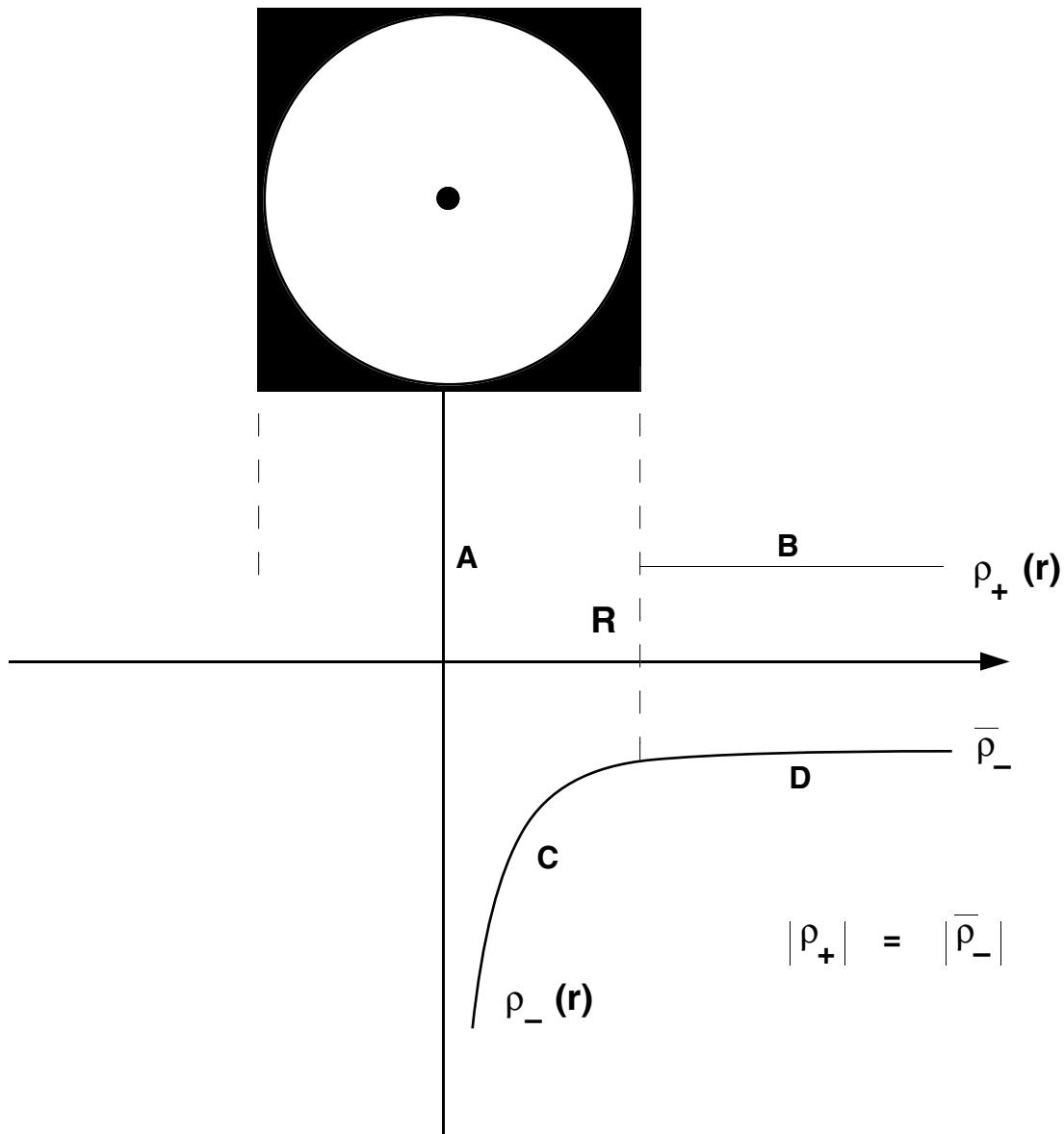


Figure 5.2. A schematic charge distribution for the “muffin-tin” atomic model: (a) a point nucleus at the center of a spherical cavity; (b) a constant positive charge density outside the cavity which represents surrounding ions; (c) a spherically symmetric electronic charge density inside the cavity; (d) a volume averaged electronic charge density outside the cavity. R is the radius of the cavity.

electron density distributions show the same shell structure in all the cases, but significant differences appear away from the interior region at different matter densities. At normal density, our calculated result is very close to that of the SCF band-structure calculation, and as density decreases, our calculated results converge to the isolated atom Hartree-Fock result. This indicates that to some degree the “atom-in-jellium” model correctly accounts for the environmental effects on the electron density distributions. This model smoothly connects the solid-state band-structure model and the isolated atom Hartree-Fock model, and naturally extends the solid-state band-structure model into finite temperature high density plasmas. On the other hand, for low density regimes this model describes an isolated atom or an ion in equilibrium with an electron sea.

The temperature effect on electron density distributions is shown in Figure 5.4, where the radial electron density profiles for gold at a density of 1.93 g/cm³ and three different temperatures are plotted. The charged states of the plasma are determined by summing over all the “resonance” and “free” electrons within the atomic cavity. As temperature increases, more and more electrons are excited and ionized. Therefore we see the electron density decrease in the inner regime and increase in the outer regime. It is important to note that the “atom-in-jellium” model uses the same quantum treatment for both bound and continuum states, and as a result there is a smooth transition from bound state to narrow resonance and then to broad resonance as the density or temperature is changed.

5.4. The Random-Phase-Approximation Stopping Interaction Function

The stopping interaction function, $L(\rho, V)$, describes the response of an electron gas to the perturbation of a charged projectile. It includes the polarization of the electrons by the charged particle and the resultant charge-screening and plasma density fluctuations. In the Lindhard theory, both individual electron excitation and collective plasmon excitation are treated smoothly without separate “distant” and “close” collision processes. The conventional zero-temperature Lindhard stopping interaction function takes the form [16]

$$L = \frac{6}{\pi} \int_0^{V/V_F} u du \int_0^\infty dz \frac{z^3 f_2(u, z)}{[z^2 + \chi^2 f_1(u, z)]^2 + [\chi^2 F_2(u, z)]^2} \quad (5.13)$$

where

$$f_1(u, z) = \frac{1}{2} + \frac{1}{8z} [1 - (z - u)^2] \left| \ln \frac{z - u + 1}{z - u - 1} \right| + \frac{1}{8z} [1 - (z + u)^2] \left| \ln \frac{z + u + 1}{z + u - 1} \right|, \quad (5.14)$$

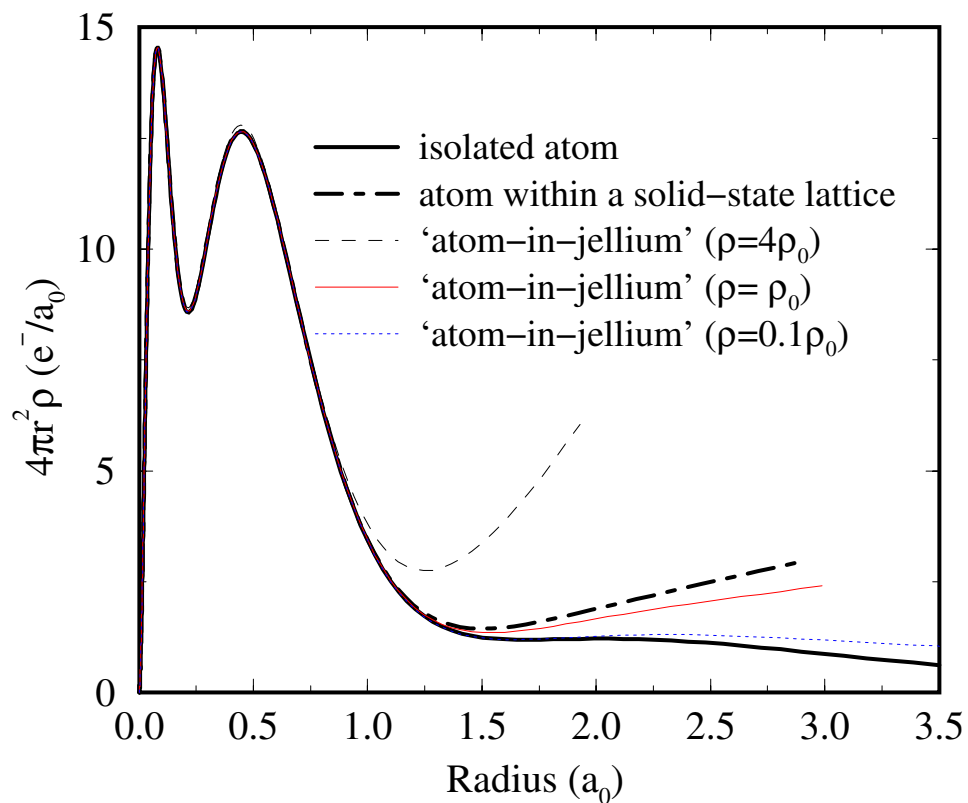


Figure 5.3. Calculated radial electron density profiles for aluminum atoms at room temperature and three different densities. Results for isolated atom and SCF band-structure calculations [13] are also shown.

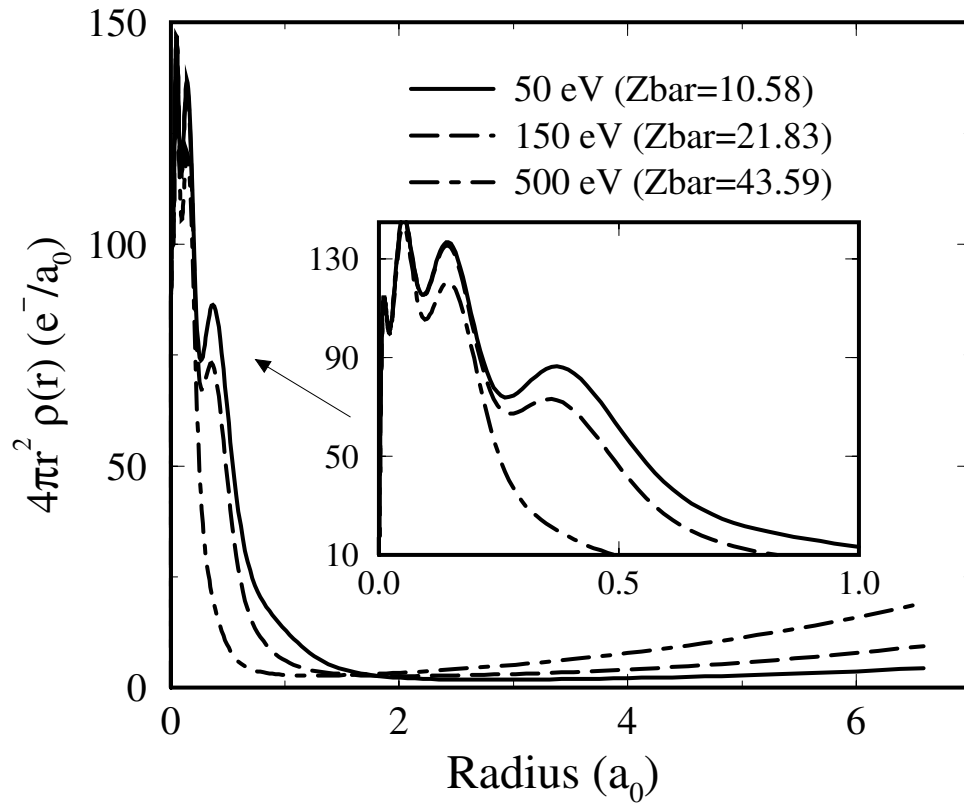


Figure 5.4. Calculated radial electron density profiles for a gold atom in plasmas with $\rho = 1.93 \text{ g/cm}^3$ and at three different temperatures.

and

$$f_2(u, z) = \begin{cases} \frac{1}{2}\pi u & \text{for } z + u < 1 \\ (\frac{\pi}{8z})[1 - (z - u)^2] & \text{for } |z - u| < 1 < z + u \\ 0 & \text{for } |z - u| > 1. \end{cases} \quad (5.15)$$

The variables z and u are the reduced wave number and frequency:

$$z = \frac{k}{2k_F} \quad \text{and} \quad u = \frac{\omega}{kV_F} \quad (5.16)$$

with k_F and V_F denoting Fermi wave number and velocity:

$$E_F = \frac{1}{2} m V_F^2 \equiv \frac{\hbar^2 k_F^2}{2m} = \frac{\hbar^2}{2m} (3\pi^2 \rho)^{2/3}. \quad (5.17)$$

The dimensionless quantity χ^2 is defined by

$$\chi^2 = \frac{V_0}{\pi V_F} \quad (5.18)$$

with $V_0 = e^2/\hbar$ denoting the Bohr velocity.

Some typical illustrations of the variation of Lindhard stopping interaction function with electron density and the ion velocity are presented in Figure 5.5. We see that each curve has a flat section at low electron densities where the ion is going much faster than the mean electron velocity. Each curve bends down where the ion velocity becomes equal to the Fermi velocity, V_F , of the free electron gas. The interaction between the free electron gas and ion is reduced at higher electron densities because some of the electrons of the free electron gas have higher velocities and can respond adiabatically to the ion.

Lindhard's result is only feasible for cold targets. For finite temperature cases, the increase of the electron thermal motion results in the decrease of ion stopping. In order to study ion stopping in ICF-relevant hot dense plasmas, it is necessary to extrapolate the zero-temperature Lindhard stopping quantity to plasmas at any temperature. Maynard and Deutsch [15] have developed a model which makes use of the full RPA dielectric function to give formulae for the temperature-dependent stopping function of the electronic stopping:

$$L = \frac{6}{\pi\chi^2} \int_0^{V/V_F} u du \int_0^\infty dz \frac{z^3 \chi^2 f_2(u, z)}{[z^2 + \chi^2 f_1(u, z)]^2 + [\chi^2 f_2(u, z)]^2} \quad (5.19)$$

where

$$f_1(u, z) = \int_0^\infty dk n^0(k) + \pi T_e \sum_{n=0}^\infty \left\{ \frac{b_n}{\gamma_n} - \frac{1}{4z} \left[\tan^{-1} \left(\frac{P_+ + a_n}{b_n} \right) + \tan^{-1} \left(\frac{P_+ - a_n}{b_n} \right) - \tan^{-1} \left(\frac{P_- + a_n}{b_n} \right) - \tan^{-1} \left(\frac{P_- - a_n}{b_n} \right) \right] \right\}, \quad (5.20)$$

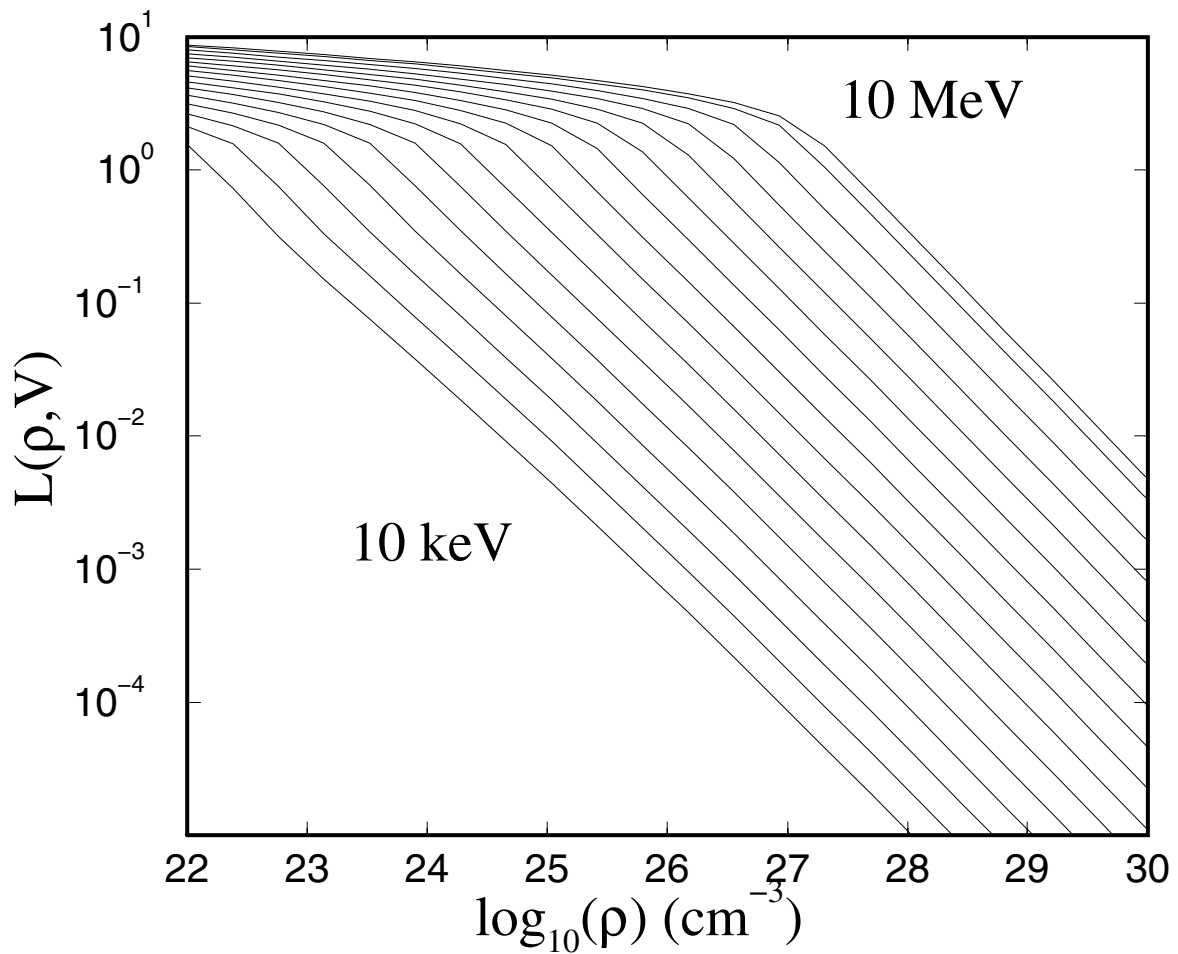


Figure 5.5. Plot of variation in zero-temperature Lindhard stopping function with electron density for various projectile energies.

$$f_2 = -\frac{\pi T_e}{8z} \ln \left\{ \frac{1 + \exp \left[\frac{\gamma - P_+^2}{T_e} \right]}{1 + \exp \left[\frac{\gamma - P_-^2}{T_e} \right]} \right\}, \quad (5.21)$$

with

$$\begin{aligned} n^0(k) &= \left[\exp \left(\frac{k^2 - \gamma}{T_e} \right) + 1 \right]^{-1}, \\ T_e &= \frac{T}{T_F}, \\ P_{\pm} &= u \pm z, \\ \gamma &= \alpha T_e. \end{aligned} \quad (5.22)$$

The quantity α is determined from

$$F_{1/2}(\alpha) = \frac{2}{3} T_e^{-3/2}, \quad (5.23)$$

where $F_n(\alpha)$ denotes the Fermi function. The coefficients a_n and b_n in Eq. (20) are given by

$$\begin{aligned} a_n &= \pm \frac{1}{2} \{ \gamma + [\gamma^2 + (2n+1)^2 \pi^2 T_e^2]^{1/2} \}^{1/2} \\ \text{and} & \\ b_n &= \pm \frac{1}{2} \{ \gamma + [\gamma^2 + (2n+1)^2 \pi^2 T_e^2]^{1/2} \}^{1/2}. \end{aligned} \quad (5.24)$$

It is important to note that with these equations, one can recover the Lindhard result at the low-temperature limit ($T = 0$) and make a quantitative connection to the well-known Jackson procedure [17] at the high-temperature limit ($T \rightarrow \infty$):

$$L_{RPA} = L_e^J + \psi(x) \Delta(x) \quad (5.25)$$

where

$$\begin{aligned} x &= V/V_{th}, \\ \psi(x) &= \text{erf}(x) - \frac{2x}{\sqrt{\pi}} e^{-x^2}, \\ \Delta(x) &= \Delta_1(x) + \frac{1}{2} \Delta_2(x) + \frac{1}{2} - \ln(0.764x^2 \sqrt{1 + 1/x^2}). \end{aligned}$$

The functions $\Delta_1(x)$ and $\Delta_2(x)$ have been tabulated by May [18].

Direct application of the RPA stopping number to large scale stopping power calculations is a formidable task since f_1 is a very slowly converging quantity. We

have chosen an interpolation formula of $L(T, \rho, V)$ which bridges the accurate asymptotic expression of Eq. (19) in both the small and large projectile velocity limits [15]:

$$L(T, \rho, V) = \begin{cases} L^1 = \left(\frac{V}{V_F}\right)^3 C(\chi^2, \alpha) \frac{1}{1+GV^2} & V \leq V_{\text{int}} \\ L^2 = \ln\left(\frac{2mV^2}{T\omega_0}\right) - \frac{\langle V_e^2 \rangle}{V^2} - \frac{\langle V_e^4 \rangle}{2V^4} & V \geq V_{\text{int}}, \end{cases} \quad (5.26)$$

where

$$\left\langle \frac{V_e^{2n}}{V_F^2} \right\rangle = \frac{T_e^n F_{n+1/2}(\alpha)}{F_{1/2}(\alpha)}, \quad (5.27)$$

$$C(\chi^2, \alpha) = \int_0^\infty \frac{dz z^3}{(z^2 + \chi^2 f_1(z, 0))^2 \left[1 + \exp\left(\frac{z^2}{T_e} - \alpha\right)\right]}. \quad (5.28)$$

The interpolation boundary velocity, V_{int} , can be determined from

$$V_{\text{int}} = \left[\frac{3\langle V_e^2 \rangle}{2} + \frac{3\bar{h}\omega_0}{2m} \right]^{1/2}, \quad (5.29)$$

and G is fixed by $L^1(V_{\text{int}}) = L^2(V_{\text{int}})$. Detailed numerical calculations have shown that the relative error of this interpolation formula is smaller than a few percent at any temperature.

The values of the exact RPA stopping function for ions of various energies stopped in uniform electron gases with different densities and temperatures are shown in Figures 5.6 and 5.7. It is seen that as temperature increases, the interaction strength decreases. This temperature effect can be seen more clearly from Figure 5.8, where stopping powers calculated from two different stopping functions for protons in a gold plasma with $T = 1$ keV and $\rho = 0.193$ g/cm³ are compared. We see that the use of the Lindhard stopping function significantly overestimates the stopping power in the low energy regime. With the exact RPA stopping function, we have an accurate description for ion stopping in plasmas over the whole temperature range.

5.5. Effective Charge Theory

The effective charge of an ion is usually inferred by comparing the stopping power of a higher- Z ion to that of a proton. Any deviation from a Z^2 dependence is attributed to an effective charge. In our calculations, we use the expression given by Brown and Moak [19]:

$$\bar{Z}_1/Z_1 = 1. - 1.034 \exp(-137.04 \beta / (Z_1)^{0.69}). \quad (5.30)$$

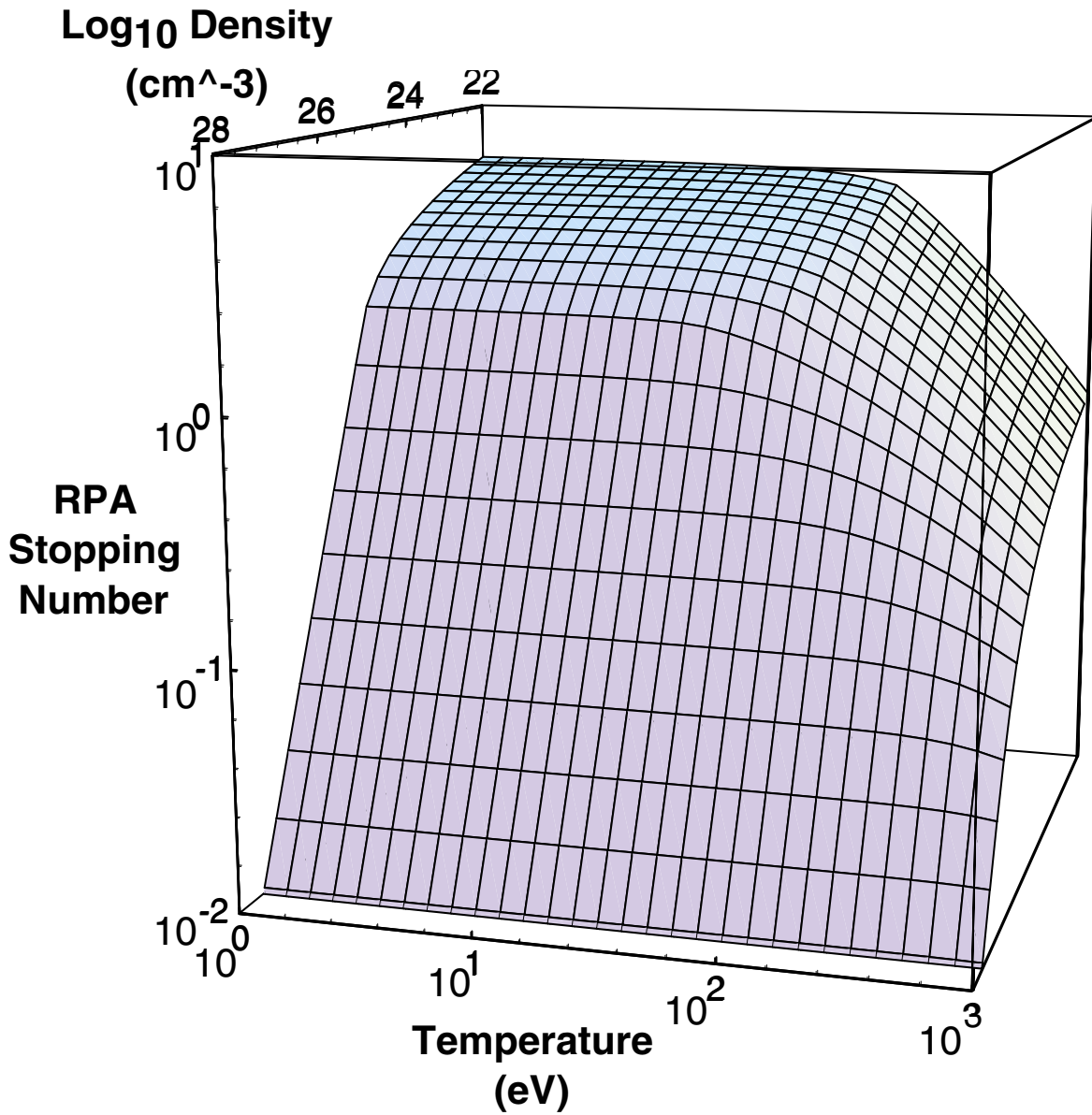


Figure 5.6. Plot of variation in the full RPA stopping function with electron density and temperature for ions with $E = 1$ MeV/amu.

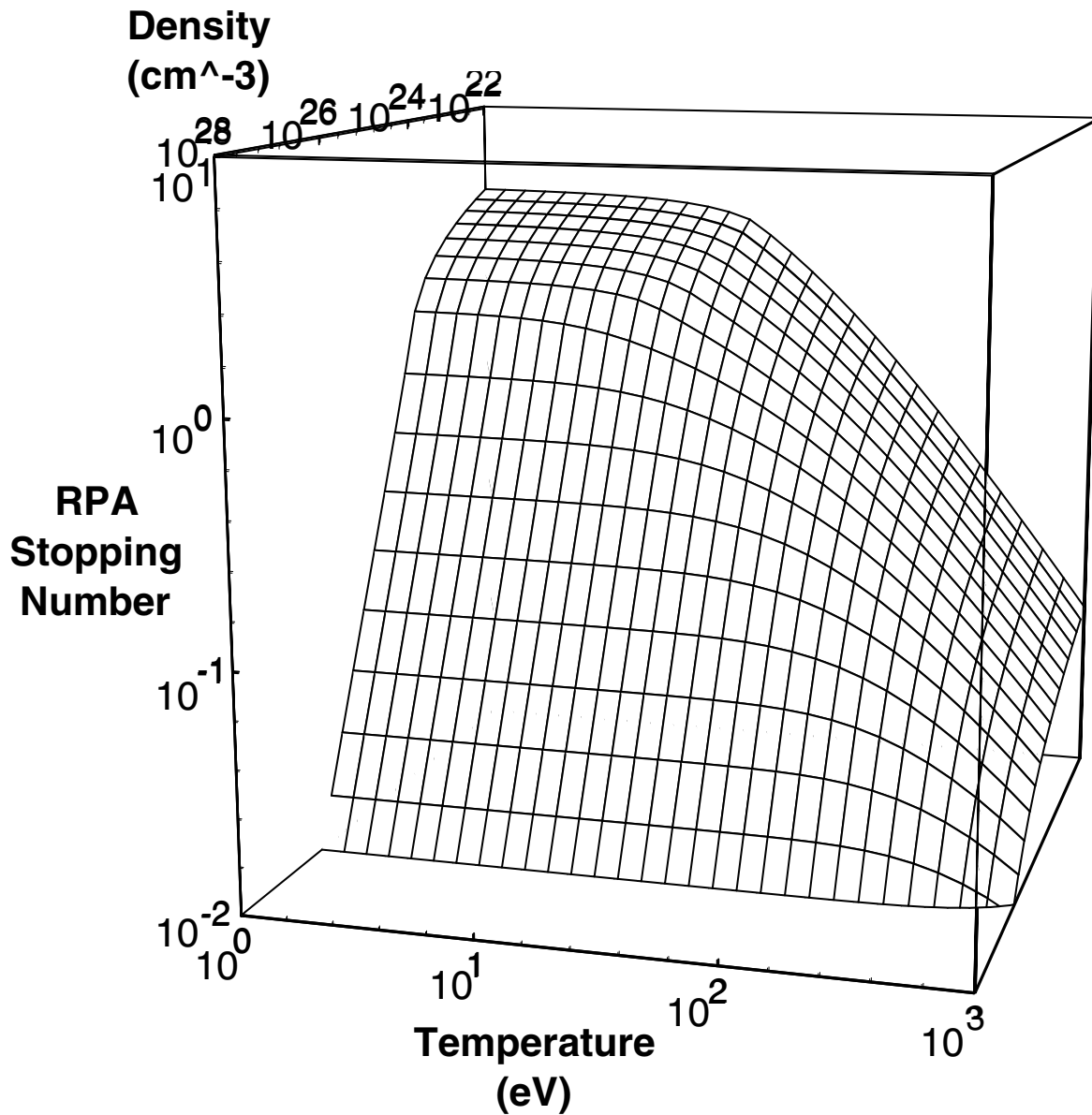


Figure 5.7. Plot of variation in the full RPA stopping function with electron density and temperature for ions with $E = 0.1$ MeV/amu.

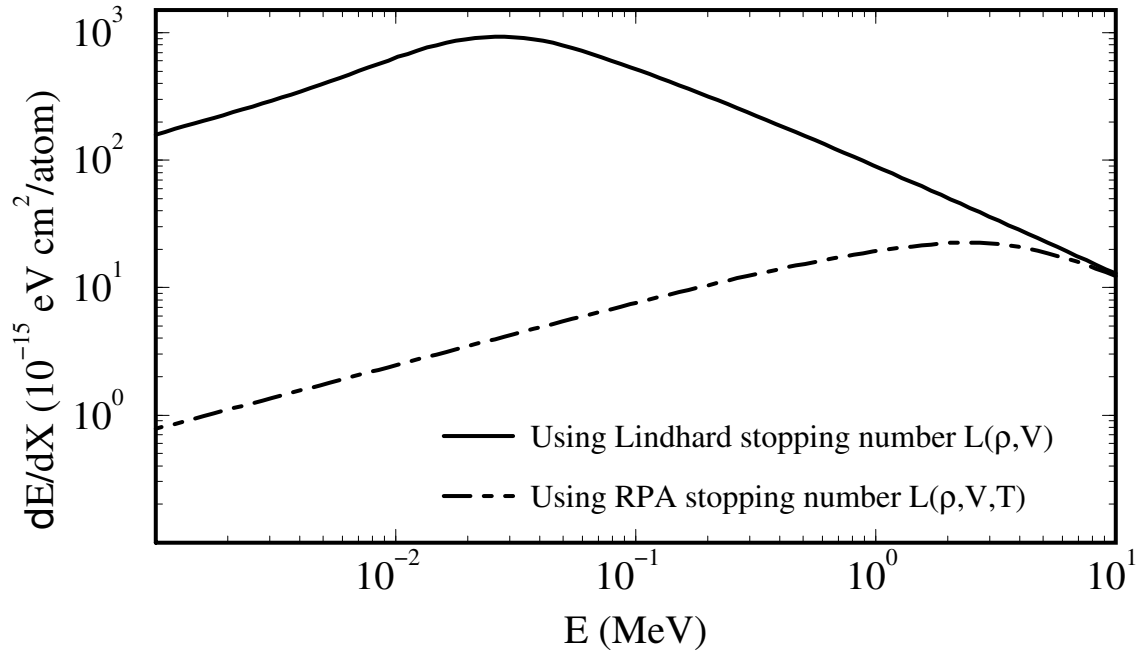


Figure 5.8. Stopping power for protons in a gold target with $T = 1$ keV and $\rho = 0.193$ g/cm³. Shown are results calculated with the Lindhard stopping function and the full RPA stopping function.

where β is the ion velocity in the units of the speed of light. Figure 5.9 displays the effect of the effective charge of the projectile ion on the stopping power. In the figure we compare the stopping powers for carbon in a cold gold target with $\bar{Z}_1 = 6$ and \bar{Z}_1 determined by Eq. (30). It can be seen that the effective charge of the projectile ion has a very important impact on the stopping power result.

We emphasize that it is very important to have reasonable expressions for \bar{Z}_1 for the ion stopping power in cold materials where experimental data is available since a scaled form of these expressions is used in heated materials where no experimental data is currently available. Furthermore, special care is required in distinguishing between charge state data that is obtained by comparison of stopping powers as mentioned above and data obtained in transmission experiments. Brandt [20] points out that the charge state of an ion can be substantially altered upon exiting a foil. Consequently, transmission data does not accurately reflect the charge state of an ion when it is inside the stopping medium.

5.6. Numerical Results

The stopping of protons on cold aluminum has been well studied. We begin by studying the case of a monoenergetic beam of proton ions incident on a planar aluminum target so that we can check the validity of the electron density distribution represented by the “atom-in-jellium” atomic model. Figure 5.10 shows the related change in the calculated proton stopping power in neutral aluminum as compared to experimental data using the isolated atom Hartree-Fock-Slater (HFS) electron density distribution and the “atom-in-jellium” electron density distribution discussed above. It can be seen that while in the high energy regime both atomic models give good agreement with the experimental data, the low energy stopping power is over-predicted for isolated atoms. It has been known that the low energy ion and high energy ion are mainly stopped by two different parts of electrons of the target atom. Most of the energy of the low energy ion is lost to outer shell electrons, while the inner shell electrons play a major role in stopping high energy ions. As mentioned above, while outer shell electrons are strongly affected by the surrounding environment, the inner shell electron distribution is relatively stable. Significant difference is seen in the spatial variation of the “atom-in-jellium” electron densities and isolated atom HFS electron densities away from the interior of the target atom due to solid state bonding effects. For inner shell electrons, especially for K-shell electrons, the density distributions of the two models are almost identical. The difference of the outer region electron density distributions of the two atomic models results in a significant discrepancy for the low energy ion stopping power. The good overall agreement of the calculated stopping power with the

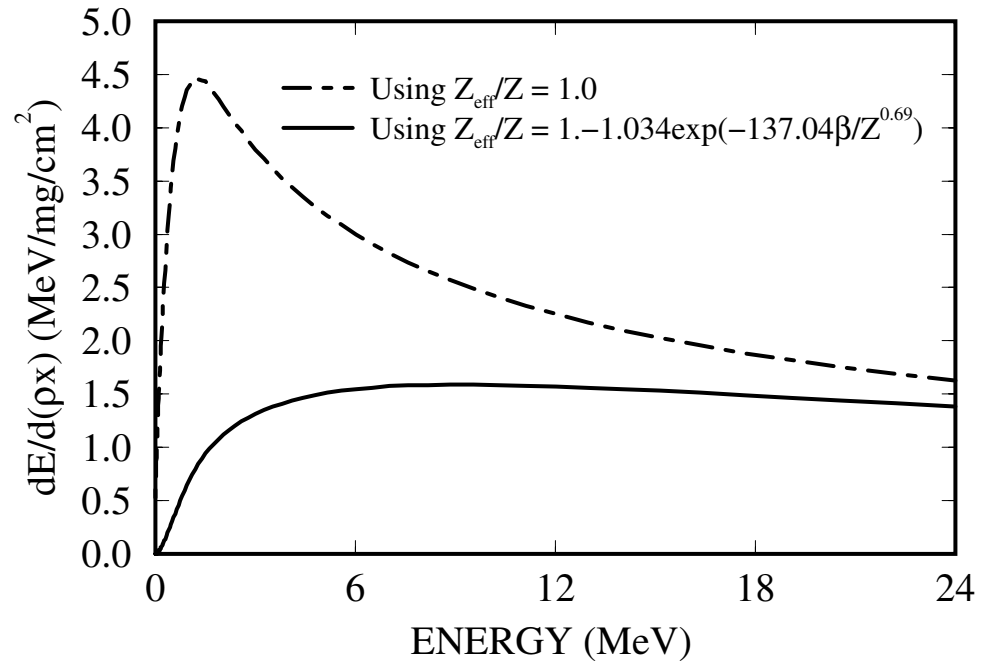


Figure 5.9. Stopping power for carbon in a gold target at room temperature and normal density. Shown are results predicted from two different effective charge models.

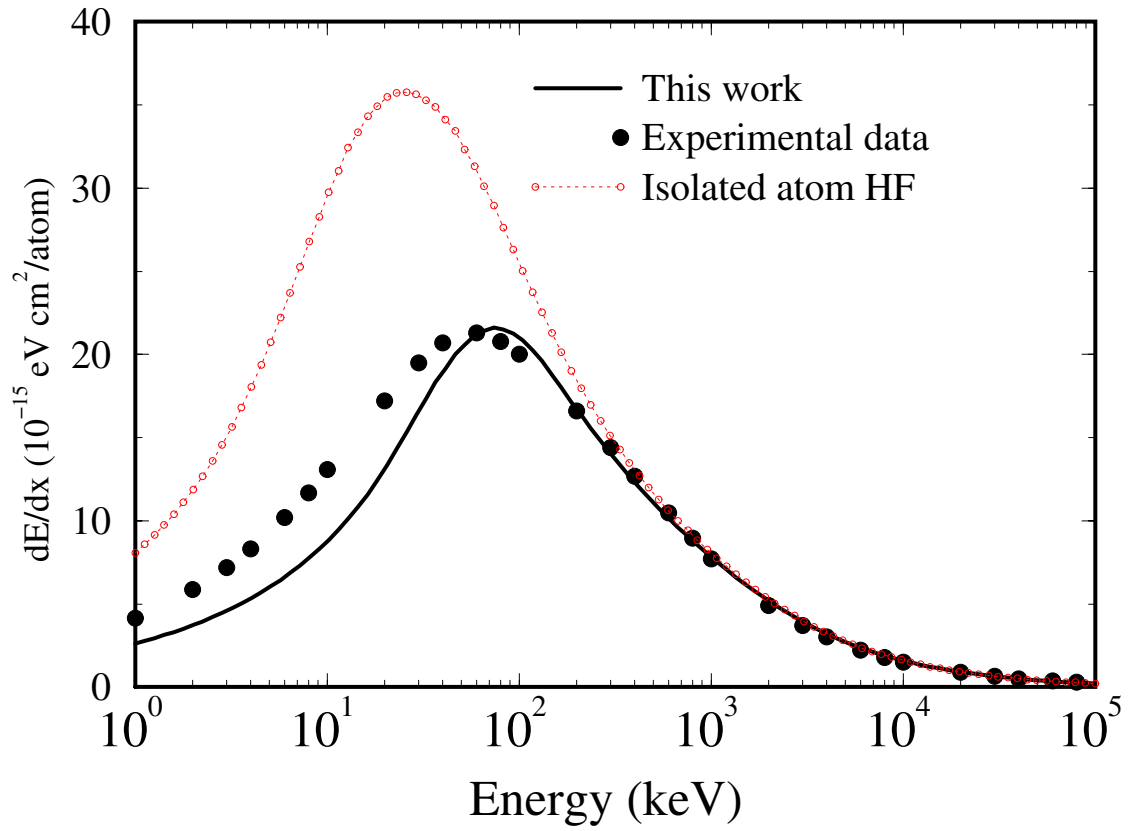


Figure 5.10. Stopping power for protons in neutral aluminum as a function of energy. Experimental data are compared with results calculated from two different electron density distributions.

experimental data [21] demonstrates that the electron distribution of the “atom-in-jellium” atomic model is quite accurate for both outer and inner shell electrons.

In Figure 5.11 the calculated proton stopping powers for a cold gold target with two different atomic electron density distributions are shown together with the experimental data [21]. We see that for this high Z target, the calculated stopping power with the “atom-in-jellium” electron density distribution shows good overall agreement with the experimental data.

Figure 5.12 shows the stopping power of a monoenergetic beam of carbon ions incident on a planar gold target. Our calculated result is compared with Northcliffe’s tabulated data [22] and the results of two other different models [1]. It can be seen that the Bethe model is only valid for the high energy range, while the LSS model is accurate in the low energy range. Our result shows good agreement with the tabulated data over the whole energy range.

Figures 5.13 and 5.14 show the stopping powers for protons in hot gold plasmas. Figure 13 represents the case of a gold target having $T_e = 1$ keV, $\rho = 0.193$ g/cm³, and Figure 14 considers the case of a gold target having $T_e = 50$ eV, $\rho = 1.93$ g/cm³. In the first case, there are about 270 electrons/Debye sphere, while in the second case, this number is only about 2.5. In both cases there is fairly good agreement between our result and that of three other commonly used models. These two cases correspond to two completely different plasma conditions. The first case represents a weakly coupling plasma, while the second case is a strongly coupling plasma. The good agreement of our results with the results of other commonly used models for these extreme cases indicates that our stopping model is valid for a wide range of target conditions.

Finally, we come to the main point of this work: studying the ion stopping characteristics of hot targets using a self-consistent treatment for both bound and free electrons. We have calculated the proton range in a hot gold target with the model discussed in previous sections and made comparisons with the results of the Generalized Oscillator Strength (GOS) model [23] and that of the scaled-Bethe model [24]. Figures 5.15 and 5.16 demonstrate the variation of the range in gold with ionization for protons of various energies. Results of this work, GOS results and those using the scaled-Bethe model are shown. There are two points of interest in this comparison. First, the range is predicted to decrease more slowly with ionization for the GOS results. Our results lie somewhere between the GOS results and the scaled-Bethe results. Secondly, our results show a smooth decrease with ionization in all the cases, while the GOS model predicts that the range for high energy projectiles can initially increase with ionization of the atom.

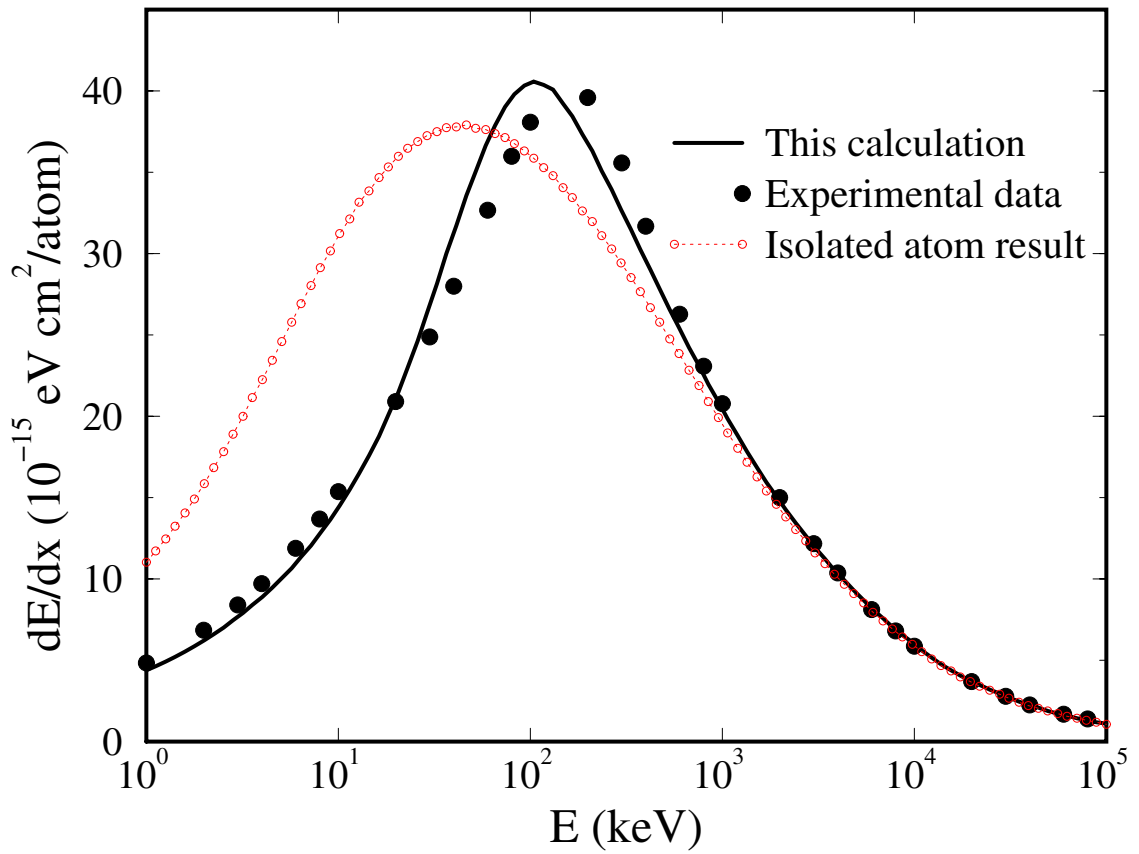


Figure 5.11. Stopping power for protons in neutral gold as a function of energy. Experimental data are compared with results calculated from two different electron density distributions.

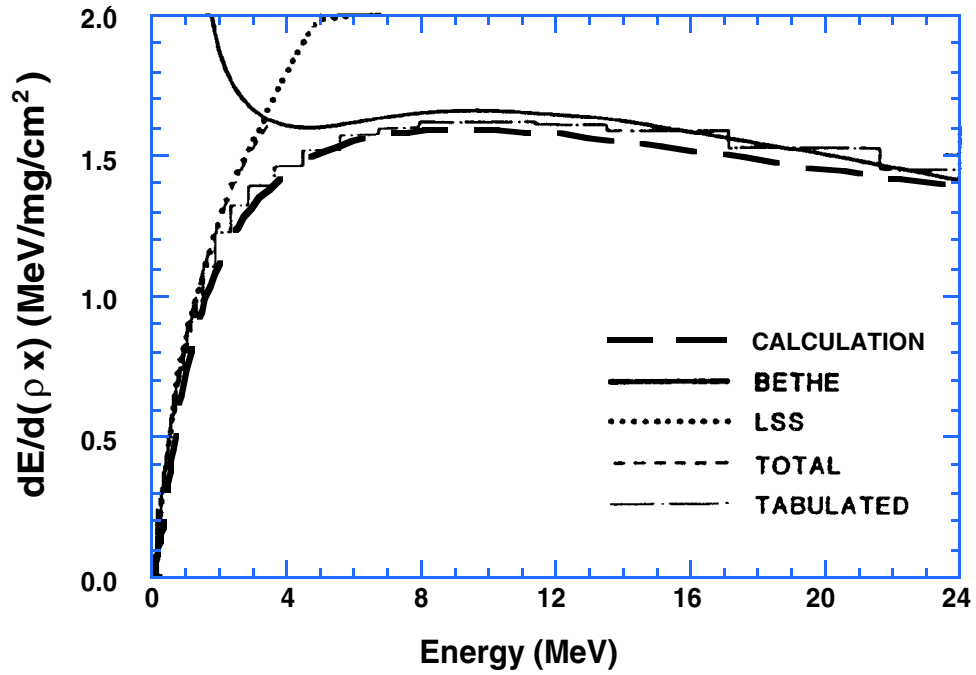


Figure 5.12. Stopping power of solid density room temperature gold for carbon ions. (Top) Calculated result from the model developed in this paper. (Bottom) Results from the LSS model, the Bethe model, and Northcliffe's tabulated values.

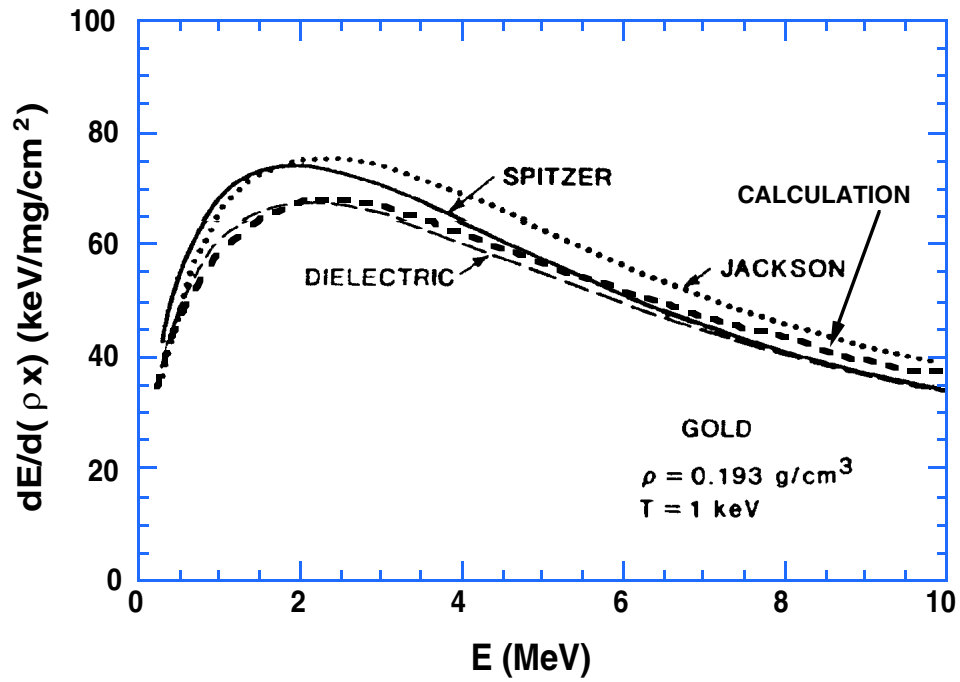


Figure 5.13. Stopping power for protons in a gold plasma with $T_e = 1 \text{ keV}$, $\rho = 0.193 \text{ g/cm}^3$. (Top) Calculated result from the model developed in this paper. (Bottom) Free electron stopping power calculated from the polarization response model (Spitzer), the simple binary model (Jackson), and the binary+collective model (Dielectric).

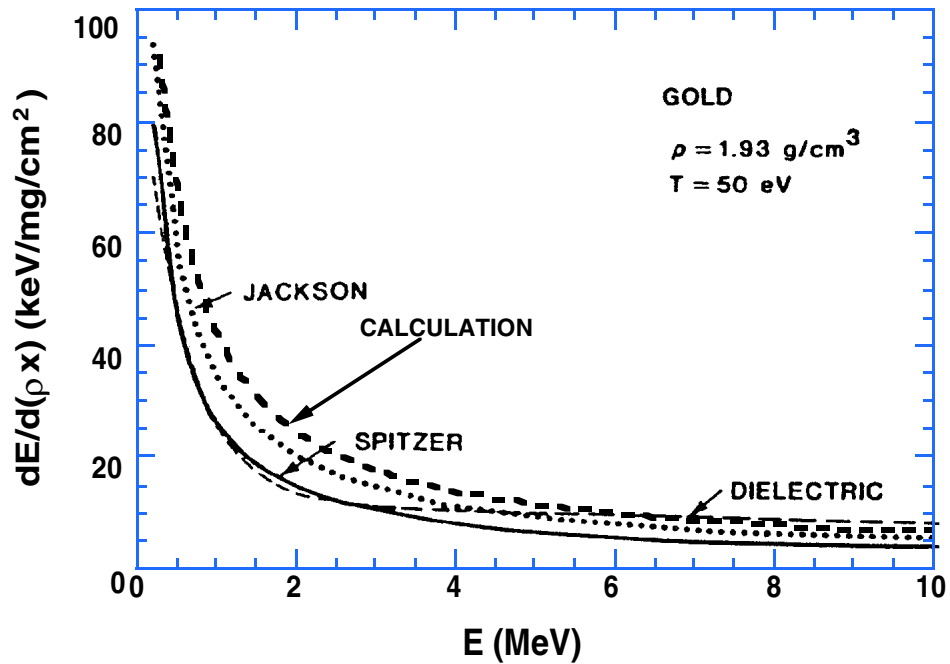


Figure 5.14. Stopping power for protons in a gold plasma with $T_e = 50 \text{ eV}$, $\rho = 1.93 \text{ g/cm}^3$. (Top) Calculated result from the model developed in this paper. (Bottom) Free electron stopping power calculated from the polarization response model (Spitzer), the simple binary model (Jackson), and the binary+collective model (Dielectric).

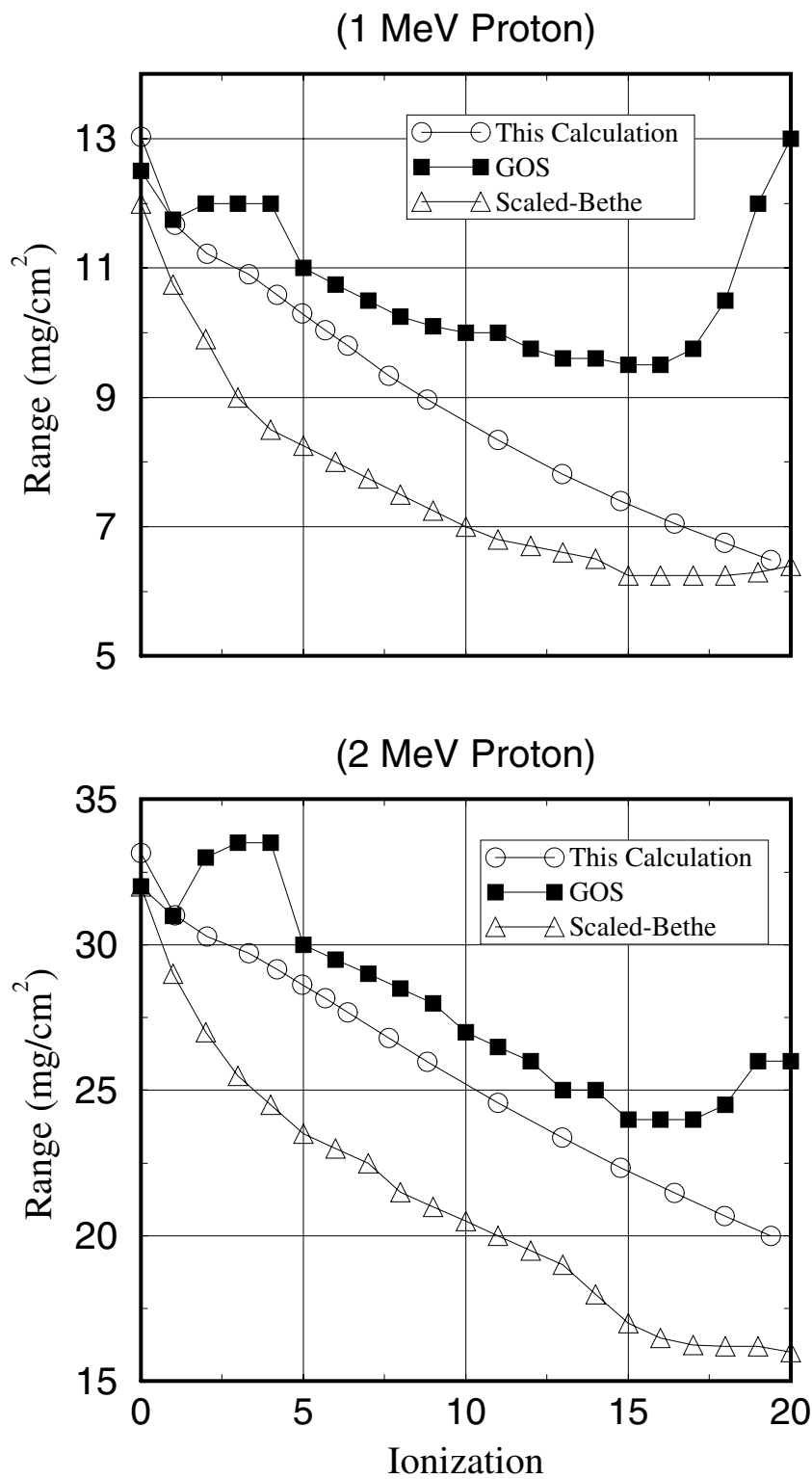


Figure 5.15. Stopping range of 1 MeV and 2 MeV protons in gold as a function of ionization state of the target. Results predicted by three different models are presented.

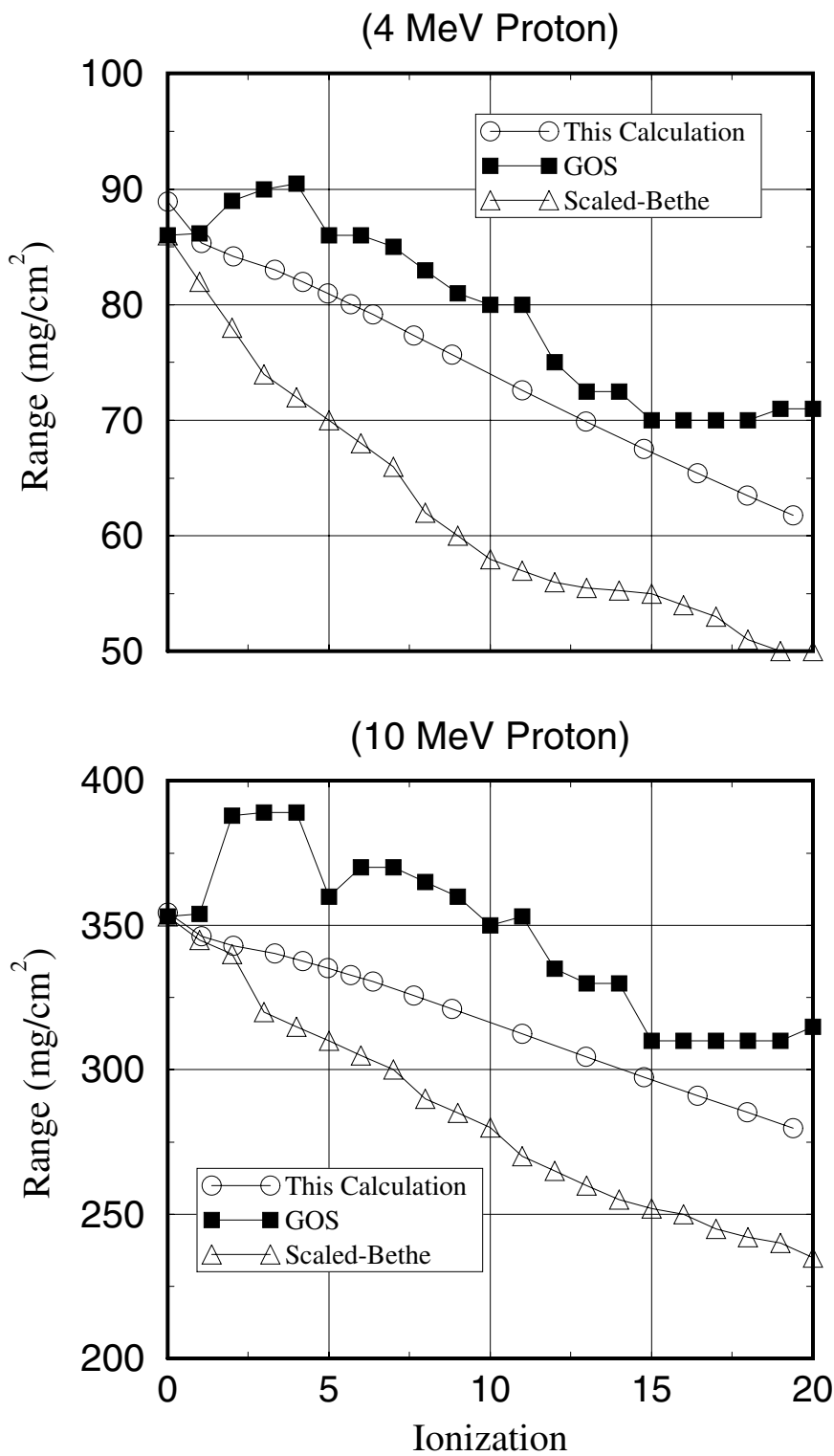


Figure 5.16. Stopping range of 4 MeV and 10 MeV protons in gold as a function of ionization state of the target. Results predicted by three different models are presented.

It has been argued [24] that such an initial range lengthening characteristic in high Z targets occurs because the interaction velocities for bound electrons are different from those of free electrons. The characteristic velocity of a bound electron is given by the local Fermi velocity and the characteristic velocity of a free electron is the thermal velocity. We note that these GOS results were calculated by assuming that all the bound electrons are in ground configurations. Hence, the physical picture for these GOS calculations is that the projectile ion interacts with two completely different groups of electrons: strongly bound ground state electrons and free plasma electrons. The bound electron interacts more strongly with the fast projectile ion than the free electron does until the plasma thermal velocity becomes comparable to or greater than the relevant Fermi velocity of the bound electron. Therefore we see the range of a slightly ionized ion can increase over that of the neutral atom in the GOS results. However, in reality we have a different physical picture for the interaction between the projectile ion and plasma. The target electrons continuously distribute over strongly bound ground states, weakly bound excited states, “quasi-bound” resonance states, and free states. The interaction velocities for electrons in different states are different. But instead of switching abruptly from the local Fermi velocity to the thermal velocity, the transitions between the electron interaction velocities in different states are smoothly continuous. Therefore the GOS results could overestimate the effect of different electron interaction velocities on the ion range. If the stopping effect from excited electrons is included in the GOS calculation, we expect that the initial range lengthening features in the GOS results could be reduced. This needs to be verified in future investigations. In our calculations, contributions from electrons in all states (ground, excited, and continuum states) are essentially taken into account in a self-consistent manner. This characteristic of the model is reflected in Eq. (11). The sum in Eq. (11) runs through the ground state and all excited states and continuum states. The population of each state is determined by the Fermi-Dirac distribution. The difference between our results and the GOS results demonstrates that the contributions from electrons in excited states and resonance states, which can be interpreted as “quasi-bound” electrons in high density plasmas, is important in stopping power calculations and should be treated carefully.

5.7. Analytic Fits

In order to provide input data for hydrodynamic codes, we have fitted the calculated stopping power data to simple analytic functions. The value of the total ion stopping power of a plasma target depends on the following parameters:

- (1) charge of the projectile,

- (2) energy (velocity) of the projectile,
- (3) nuclear charge of the target,
- (4) temperature of the target,
- (5) particle density of the target.

Hence, an ideal data table for ion stopping powers would require five dimensions. In practice, a 5-dimensional table lookup is too complicated to implement. To reduce the complexity, the following points were considered:

- A. A different data table is set up for each combination of projectile species and target plasma.
- B. For given projectile and target conditions, the stopping power is a very smooth function of projectile energy. A 10-parameter function is used for fitting the energy dependence.
- C. Our calculations show that stopping power and target charge state (\bar{Z}) are not in one-to-one correspondence. Hence, instead of using \bar{Z} , we do a curve fit for each (T, ρ) point.

At low energies, the electron stopping power is proportional to projectile velocity, while the high energy behavior of the stopping power is very well described by the Bethe formula [6]. Based on these asymptotic functional forms, we used the following functions to fit the energy dependence of stopping power, which is similar to that used by Ziegler, et al. [21]:

$$\begin{aligned}
\frac{dE}{dx} &= A_1 \cdot E^{A_2} & 0 < E \leq 0.1 E_0 \\
\left. \begin{aligned}
\frac{dE}{dx} &= S_1 \cdot S_2 / (S_1 + S_2) \\
S_1 &= A_3 \cdot E^{A_4} \\
S_2 &= (A_5/E) \cdot \ln(1 + A_6/E + A_7 E)
\end{aligned} \right\} & 0.1 E_0 < E \leq 10 E_0 \\
\frac{dE}{dx} &= (A_8/E) \cdot \ln(1 + A_9/E + A_{10} E) & E > 10 E_0.
\end{aligned} \tag{5.31}$$

The fit is divided into three parts, one for the low energy regime ($E \leq 0.1 E_0$), one for the high energy regime ($E > 10 E_0$), and one for bridging the gap between low- and high-energy regimes. The energy E_0 corresponds to the maximum of the stopping power at each temperature and density point. It has been found that this fitting procedure works very well for all cases. Typical errors in the fit are only a few percent. Figure 5.17 shows a typical comparison of calculated data and its fitting curve. It can be seen that the fit well-represents the data over the entire energy range.

5.8. Summary

We have developed a model to study the energy deposition of an arbitrary ion in a material of arbitrary composition, density, and temperature. This model includes sophisticated treatments of the electron density distribution of an atom in plasmas and a full Random Phase Approximation stopping function which extrapolates the zero temperature Lindhard stopping function to arbitrary temperatures. Therefore, it can accommodate a wide range of temperatures and densities relevant to ICF plasmas. We have shown that this model provides quite accurate ion stopping powers in cold materials, including both low-Z and high-Z targets. For finite temperature plasmas, the model accounts for the stopping effects due to electrons in ground states, excited states and continuum states in a self-consistent manner. We have compared our calculated results of proton range in a gold plasma with those of the GOS model and scaled-Bethe model. Our results lie between the results of these two different models. No initial range lengthening feature is seen in our calculated results, which appears in the GOS results. We conclude that this difference could be caused by the different treatment of less-bound electrons in excited states and resonance states.

It is worthwhile pointing out that this model is in the framework of the first-Born approximation for the projectile. For low energy heavy ions, the first-Born approximation

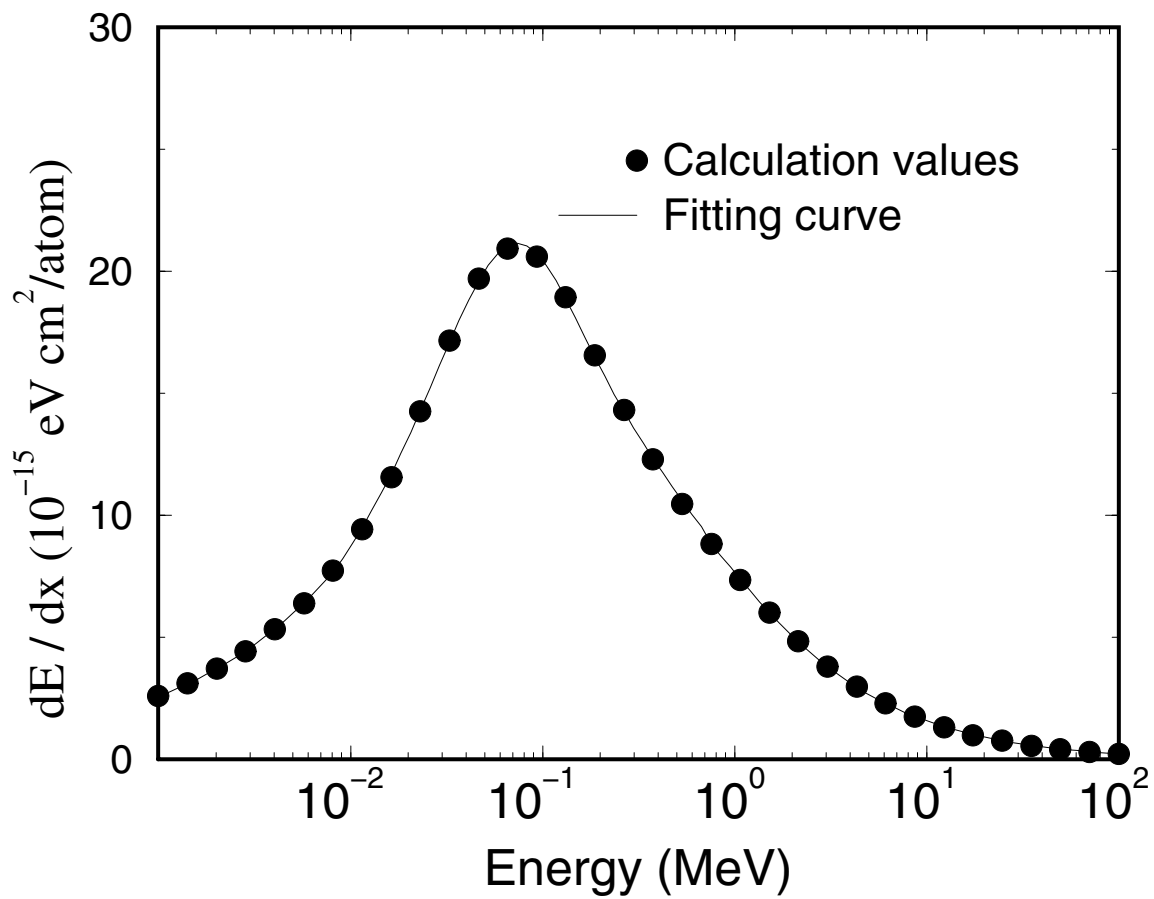


Figure 5.17. Stopping power for protons in aluminum at room temperature and normal density. Both calculated data points and the curve fit are shown.

is no longer appropriate and higher-order Born corrections should be included [15]. This can be done by directly including the Barkas term [25] and Bloch term [26] into our model. Further development of the model in this direction is currently under way.

References for Section 5

1. Mehlhorn, T.A., *J. Appl. Phys.* **52**, 6522 (1981).
2. Deutsch, C., *Laser Part. Beams* **2**, 449 (1984).
3. Nardi, E., Peleg, E., and Zinamon, Z., *Phys. Fluids* **21**, 574 (1978).
4. Peter, T. and Meyer-Ter-Vehn, J., *Phys. Rev.* **A43**, 1998 (1990).
5. Brueckner, K. A., Senbetu, L., and Metzler, N., *Phys. Rev.* **B25**, 4377 (1981).
6. Bethe, H.A., *Handbuch Der Physik*, Edited by S. Flugge, Springer-Verlag, Berlin, Vol. 24, 273 (1933).
7. More, R. M., *Adv. Atomic Molec. Phys.* **21**, 305 (1985).
8. Lindhard, J., *Mat. Fys. Medd. Dan. Vid. Selsk.* **28**, 8 (1954).
9. Lindhard, J., Scharff, M., Schiott, H.E., *Mat. Fys. Medd. Dan. Vid. Selsk.* **33**, 14 (1963).
10. Lindhard, J., Winther, A., *Mat. Fys. Medd. Dan. Vid. Selsk.* **34**, 4 (1964).
11. Lindhard, J. and Scharff, M., *Mat. Fys. Medd. Dan. Vid. Selsk.* **27**, 1 (1953).
12. Moruzzi, V. L., Williams, A. R., and Janak, J. F., *Phys. Rev* **B15**, 2854 (1977).
13. Moruzzi, V. L., Janak, J. F., and Williams, A. R., *Calculated Electronic Properties of Metals* (Pergamon, New York, 1978).
14. Liberman D. A., *Phys. Rev.* **B20**, 4981 (1979).
15. Maynard, G, and Deutsch, C., *J. Physique* **46**, 71 (1985).
16. Jackson, J.D, *Classical Electrodynamics* (Wiley, New York, 1975).
17. May, R.M., *Aust. J. Phys.* **22**, 687 (1969).

18. Iafrate, G.J. and Ziegler, J.F., *J. Appl. Phys.* **50**, 5579 (1979).
19. Brown, M.D. and Moak, C.D., *Phys. Rev.* **B6**, 90 (1972).
20. Brandt, W., *Atomic Collisions in Solids*, Edited by S. Datz, B. Appleton, and C. Moak Vol. 1, 261 (Plenum, New York, 1975).
21. Ziegler, J.F., *Stopping Cross Sections for Energetic Ions In All Elements*, Vol. 5 (Pergamon, New York, 1980).
22. Northcliffe, L. and Schilling, R., *Nucl. Data Tables* **A7**, 233 (1970).
23. McGuire, E.J., *Phys. Rev.* **A26**, 1871 (1982).
24. Mehlhorn, T.A., Peek, J.M., McGuire, E.J., Olsen, J.N., and Yong, F.C., *J. Physique* **44**, 8 (1983).
25. Barkas, W.H., Dyer, J.W., and Heckmann, H.H., *Phys. Rev. Lett.* **11**, 26 (1963).
26. Bloch, F., *Ann. Phys.* **16**, 285 (1933).

6. Analysis of K_α Satellite Emission Spectra

6.1. Improvements to Radiation-Hydrodynamics Modeling

The purpose of this section is to summarize simulations regarding the analysis of the K_α spectroscopy experiments on PBFA-II.

A fairly substantial effort was recently made to understand the effects of line radiation on the overall energetics and temperature of the expanding foil targets. The CRE line transport model within the hydrocode was improved to take into account the effects of the radiation emitted by the gold (as well as other layers) on heating the Al due to the Al line opacity. Thus, when using the “full” radiation model in calculations described in this section, the following are taken into account:

1. The continuum is transported using a multigroup (100 groups), multiangle integral radiation transport model; the opacities for the continuum are tabulated ahead of time using EOSOPA code of P. Wang; the continuum opacities are computed using CRE populations which neglect photoexcitation/photoionization (LTE is not assumed).
2. Line radiation effects are modeled using a CRE model which includes resonant self-absorption effects on the NLTE atomic level populations; a total of 269 levels were used (222 for Al, 43 for CH, 4 for H); 1368 lines were transported; after the populations are obtained, zone-to-zone escape probability (EP) coupling coefficients are obtained to get the heating/cooling in each zone; the net heating rate for each line also takes into account the radiation due to an external continuum source (e.g., the gold); this is done within the context of the escape probability model and introduces no more assumptions than those already in the EP modeling.

The CRE model within the hydrocode was benchmarked using the standalone CRE model. In the standalone calculation, a more refined treatment of the radiation effects on the populations and heating/cooling rates is done. For example, the effects of the Al continuum radiation field on photoexcitations is modeled, as are its effects on heating/cooling rates. (In short, the emissivities and opacities computed before doing the radiation transport include all Al transitions as well as a blackbody radiation field due to the external source).

Figures 6.1 and 6.2 show the net heating rates computed using the standalone CRE code (NLTE) and the hydrocode (BUCKY/CRE), respectively. In each case, results for an electron temperature of $T_e = 25$ eV for the Al are plotted at the top, and $T_e = 35$ eV are

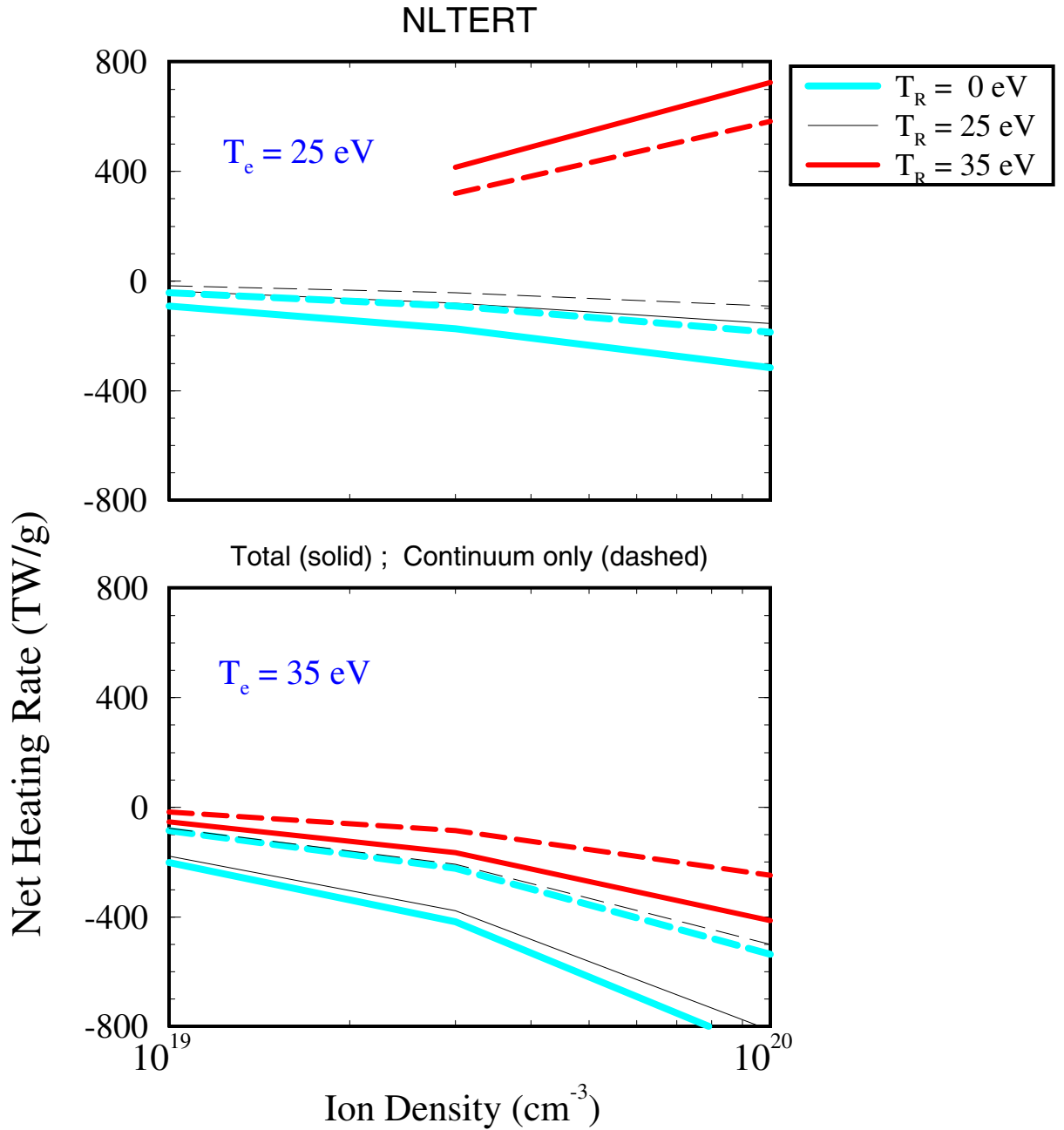


Figure 6.1. Calculated using standalone CRE code (NLTERT): net radiative heating rates for an Al plasma at electron temperatures of $T_e = 25$ eV (top) and $T_e = 35$ eV (bottom). The plasma is exposed on one side to a blackbody radiation source with $T_R = 0, 25,$ and 35 eV. The total (lines + continuum) net heating is represented by solid curves. The continuum contribution is represented by dashed curves.

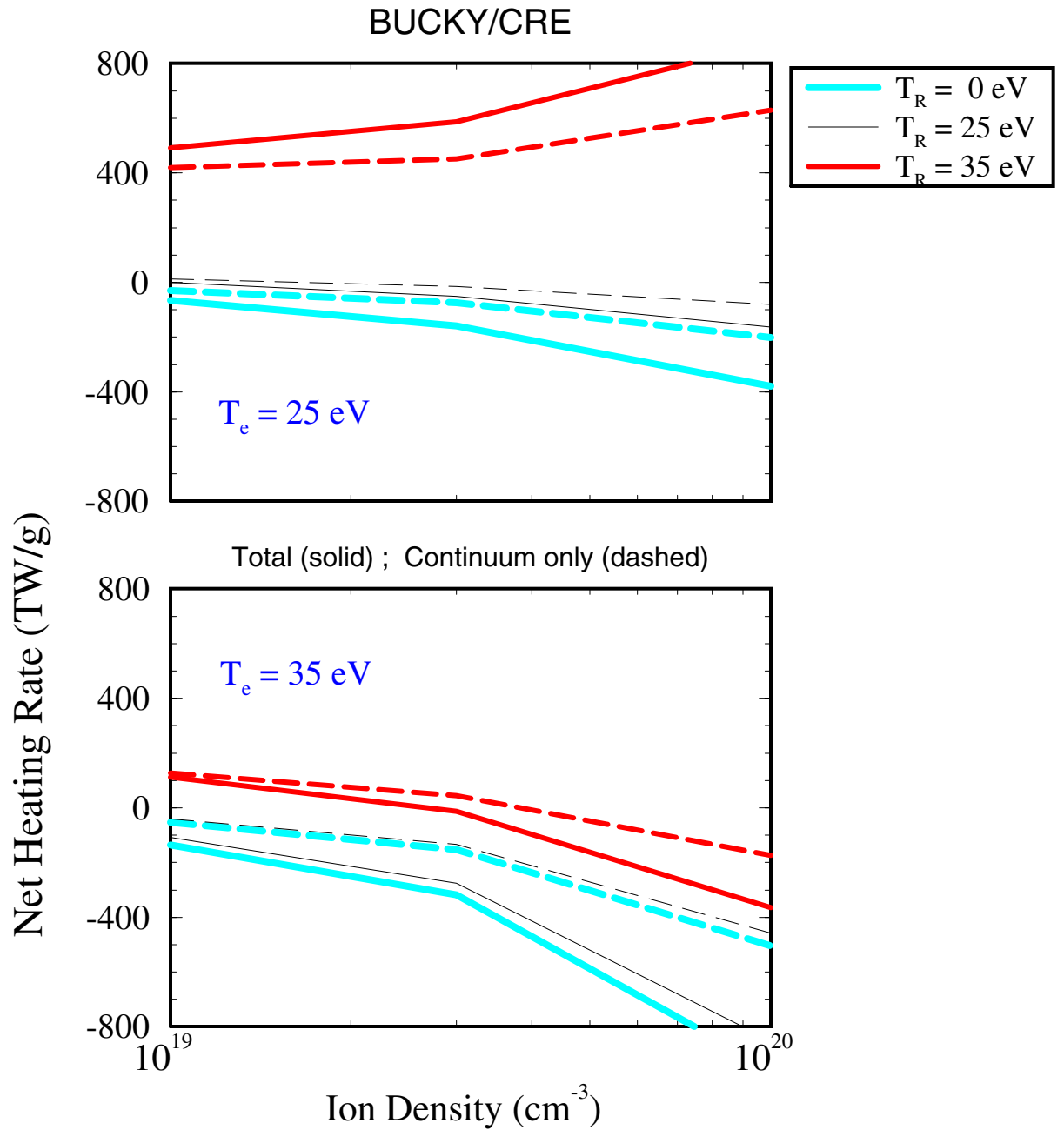


Figure 6.2. Same as Fig. 6.1, but results are from CRE and continuum radiation transport models in BUCKY-1 radiation-hydrodynamics code.

plotted at the bottom. All plots are as a function of Al ion density. The different curves in each plot correspond to 3 different radiation temperatures due to an external source ($T_R = 0, 25,$ and 35 eV). The solid curves represent total net radiative heating, while the dashed curves represent the contribution from the continuum only.

Looking at the bottom plot in Figure 6.1, one can see that for no external radiation source ($T_R = 0$), the net cooling rate (< 0 indicates cooling) for a 35 eV Al plasma is 893 TW/g at 10^{20} ions/cc and 202 TW/g at 10^{19} ions/cc. Clearly, there is a very strong density dependence on the net cooling rate. We next look at the case when the external radiation field is $T_R = 25$ eV (thin dark line). Note that this is an important case because this is typically what is predicted by the hydrodynamics simulations of the flat-foil experiments in the $t = 20$ to 30 ns regime. During this phase the Al must continue to be heated so that the He- and Li-like satellites produce observable fluxes. In this case, the total net cooling rate is 814 TW/g at 10^{20} ions/cc, and 178 TW/g at 10^{19} ions/cc. Thus, there is a reduction $\sim 10\%$ or so due to the $T_R = 25$ eV external radiation field. As the external radiation temperature becomes closer to the plasma temperature, the net cooling rate decreases substantially, and would go to zero at $T_R = 35$ eV if it were applied at both sides of the Al plasma (this would represent a case of true radiative equilibrium; populations would be LTE; and there would be zero net heating). Note that in the upper plot where $T_e = 25$ eV, when $T_R = 35$ eV the plasma is being radiatively *heated* (net heating > 0) by the external source. This situation, however, does not occur in the flat-foil experiments.

Looking now at Figure 6.2, one can see that there is reasonably good agreement between the net heating rates predicted by the hydrocode model (Fig. 6.2) and the standalone code (Fig. 6.1). Typical differences between the two calculations are $\sim 50 - 100$ TW/g for the total net heating and about half of that for the line contributions. By comparison, the Li ion beam heating rate is $\sim 200 - 400$ TW/g. Note that without the recent improvements to the hydro CRE model, the net line heating predicted by BUCKY would show no dependence on the external radiation temperature.

It is also interesting to compare results using a more “traditional” radiation transport model. Figure 6.3 shows results in which the individual lines were NOT transported using the CRE model (which includes resonant self-absorption effects), but instead were transported along with the continuum using the multigroup transport model (still 100 groups). Looking at the $T_e = 35$ eV, $T_R = 25$ eV case (bottom plot), one sees that the cooling rate is 2100 TW/g at 10^{20} ions/cc, and 1160 TW/g at 10^{19} ions/cc (by comparison, the NLTERT results were 814 and 178 TW/g, while the BUCKY/CRE results were 851 and

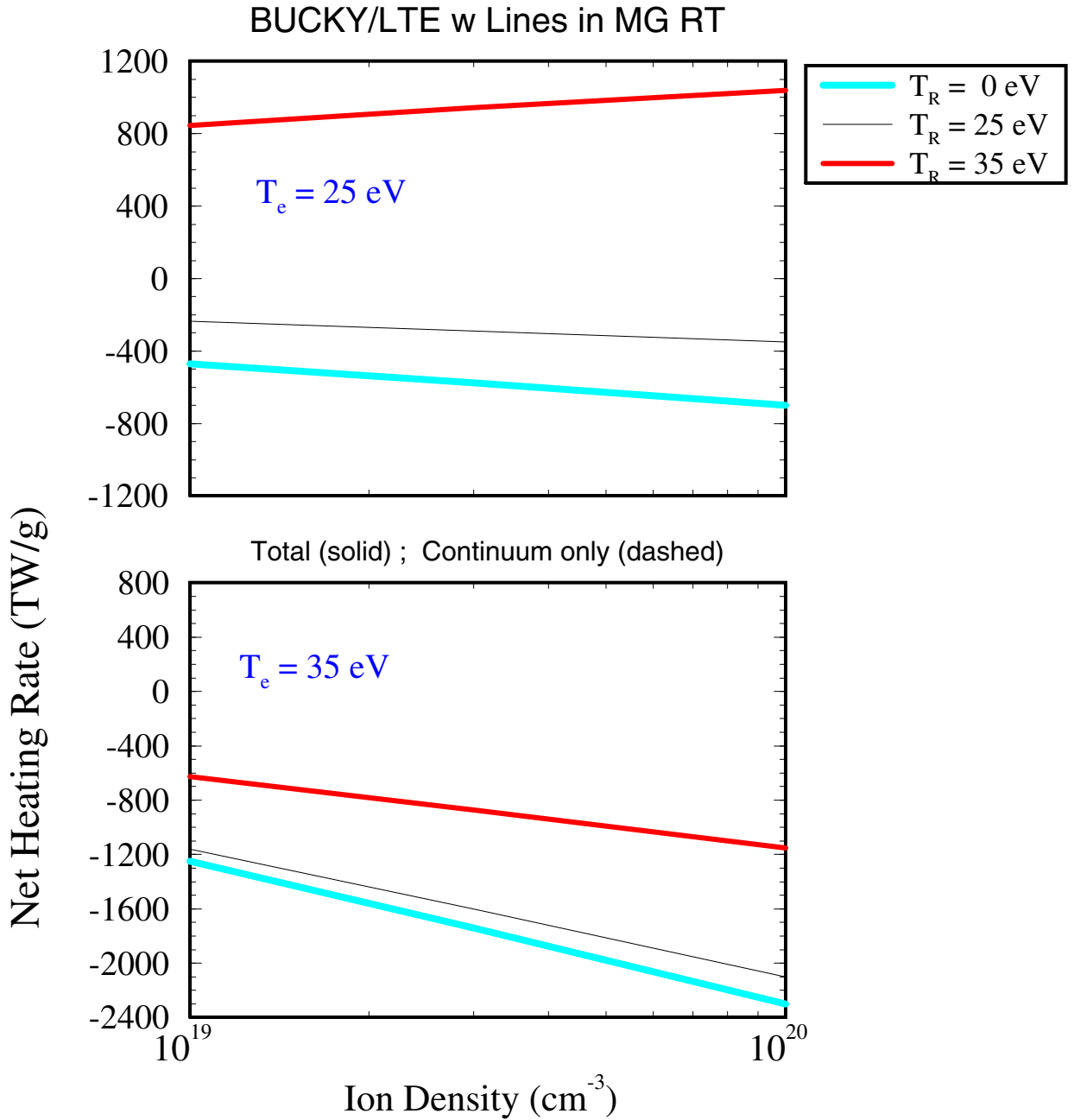


Figure 6.3. Same as Fig. 6.2, but with line opacities and emissivities both contained within multigroup opacities. This method of *not* transporting lines individually represents the more “traditional” approach to multigroup radiation transport used within many radiation-hydrodynamics codes.

109 TW/g). Clearly, the CRE line transport model represents a significant improvement over the traditional multigroup model in which line opacities/emissivities are grouped together with the continuum. Nevertheless, the radiation modeling must still be considered one of the important sources of uncertainty in the analysis of the K_α experiments due to the complexity of the atomic physics.

6.2. Improvements to Collisional-Radiative Modeling

We have upgraded our CRE and atomic models to include in detail dielectronic recombination processes. The primary purpose is to assess the effects of dielectronic recombination on K_α satellite spectra in light ion beam experiments. Also, we have attempted to understand why an emission feature appears just to the long-wavelength side of the He_α line in the experimental spectra, but has not appeared in our computed spectra. In this section, we also discuss: (1) what transitions this feature is likely due to; (2) under what conditions the feature “normally” appears (that is, when not in the presence of fast ions or electrons); and (3) possible explanations for the feature in the PBFA-II experiments.

Dielectronic recombination is modeled by computing the electron capture rate coefficient (β_{ec}) from the autoionization rates using the detailed balance relation:

$$\beta_{ec} = A_\ell^a n_e (1.66 \times 10^{-22} \text{ cm}^3 \text{ eV}^{3/2}) \left(\frac{g_\ell}{g_u} \right) T^{-3/2} e^{\Delta E_{u\ell}/T}$$

where A^a is the autoionization (Auger) rate from level ℓ , n_e is the electron density, g_ℓ and g_u are the statistical weights of the upper (i.e., higher ionization state) and lower states, respectively, T is the electron temperature and $\Delta E_{u\ell}$ is the energy separation of the two states. To test the reliability of the new model, we have compared our results with the previously published calculations of Duston and Davis [1]. Results are shown in Figure 6.4, where the ratio of the Li-like jk satellite ($1s^1 2p^2 \ ^2D \rightarrow 1s^2 2p^1 \ ^2P$) to the He_α line is plotted as a function of ion density for an optically thin Al plasma. Results are shown for two electron temperatures: $T = 300$ eV and $T = 1200$ eV. Our results are represented by the circles and squares, while the results of Duston and Davis are indicated by the solid curves. Except for ion densities $\gtrsim 10^{-1} n_{\text{solid}}$ ($n_{\text{solid}} = 6 \times 10^{22}$ ions/cm³ for Al), the predicted line ratios are in reasonably good agreement. Differences in the two calculations could be due to differences in the Auger rates, fluorescence yields, collisional excitation rates, and/or the degree of atomic level coupling in the atomic models. Note that the agreement is good for the ion densities in the PBFA-II K_α experiments ($n \sim 10^{-3} n_{\text{solid}}$).

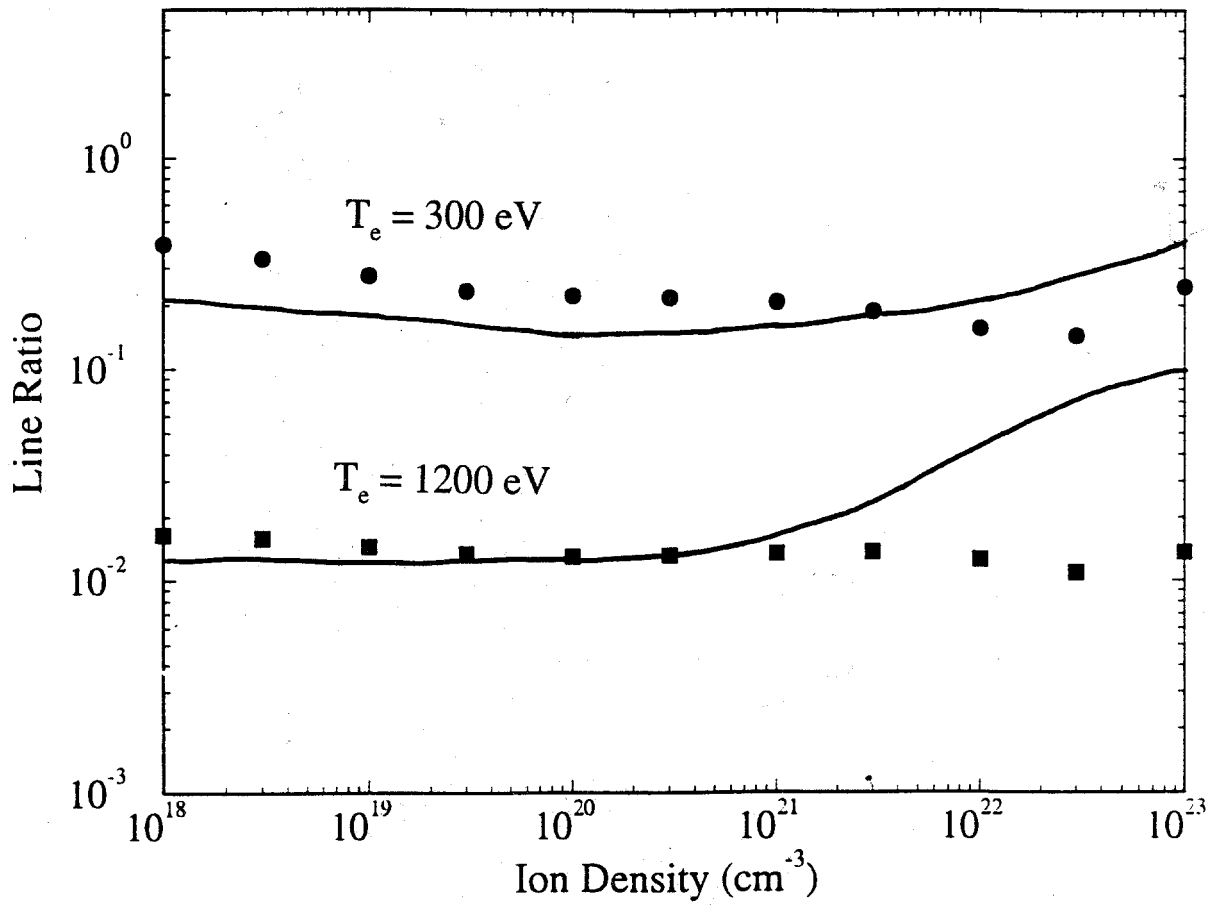


Figure 6.4. Comparison between computed line intensity ratios for the Li jk satellite to He $_{\alpha}$. Filled symbols: UW results; solid curve: Duston and Davis (1980).

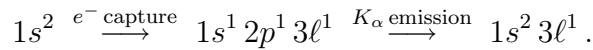
Table 6.1. Transition Data for Al He $_{\alpha}$ Spectral Region

Upper State	Lower State	$f_{\ell u}$	$\lambda(\text{\AA})$
1s ¹ 2p ¹ ¹ P	1s ² ¹ S	.789	7.757
1s ¹ 2p ¹ 3d ¹ ² P	1s ² 3d ¹ ² D	.142	7.756
1s ¹ 2p ¹ 3d ¹ ² F	1s ² 3d ¹ ² D	.295	7.765
1s ¹ 2p ¹ 3p ¹ ² S	1s ² 3p ¹ ² P	.070	7.768
1s ¹ 2p ¹ 3d ¹ ² D	1s ² 3d ¹ ² D	.253	7.772
1s ¹ 2p ¹ 3s ¹ ² P	1s ² 3s ¹ ² S	.603	7.774
1s ¹ 2p ¹ 3p ¹ ² P	1s ² 3p ¹ ² P	.244	7.776
1s ¹ 2p ¹ 3p ¹ ² D	1s ² 3p ¹ ² P	.367	7.778

Figure 6.5 shows a calculated spectrum for an Al plasma at $T = 100$ eV and $n = 10^{-3} n_{\text{solid}}$. Note the appearance of several strong emission lines on the long wavelength side of the He $_{\alpha}$ line (which is a $1s2p^1P \rightarrow 1s^2^1S$ transition). In the calculation, besides He $_{\alpha}$ ($\lambda = 7.757$ Å) there are 7 strong emission lines (using a LS term split model) between $\lambda = 7.756$ Å and 7.778 Å. Table 6.1 lists some of the properties of these transitions. They are all of the type:

$$1s^1 2p^1 3\ell^1 \rightarrow 1s^2 3\ell^1, \quad \ell = s, p, d.$$

That is, these are He $_{\alpha}$ -like transitions with M-shell spectator electrons. The appearance of these features in this calculation is due to dielectronic recombination, which for these transitions originate from the He-like Al ground state:



It is worth noting that this feature has also appeared in laser-produced plasma spectra. Figure 6.6 shows a spectrum obtained from a recent paper by Renner et al. [2]. Note the M-shell spectator lines at 7.77 Å are clearly seen.

Note that the energy of the free electron colliding with the ion in the $1s^2$ state must have an energy at least as large as the energy difference between the 2 states (that is, $E(1s^1 2p^1 3\ell) - E(1s^2)$). This energy is 1.4 keV. Therefore, if the electron distribution is Maxwellian the electron temperature must be sufficiently high to have enough electrons with

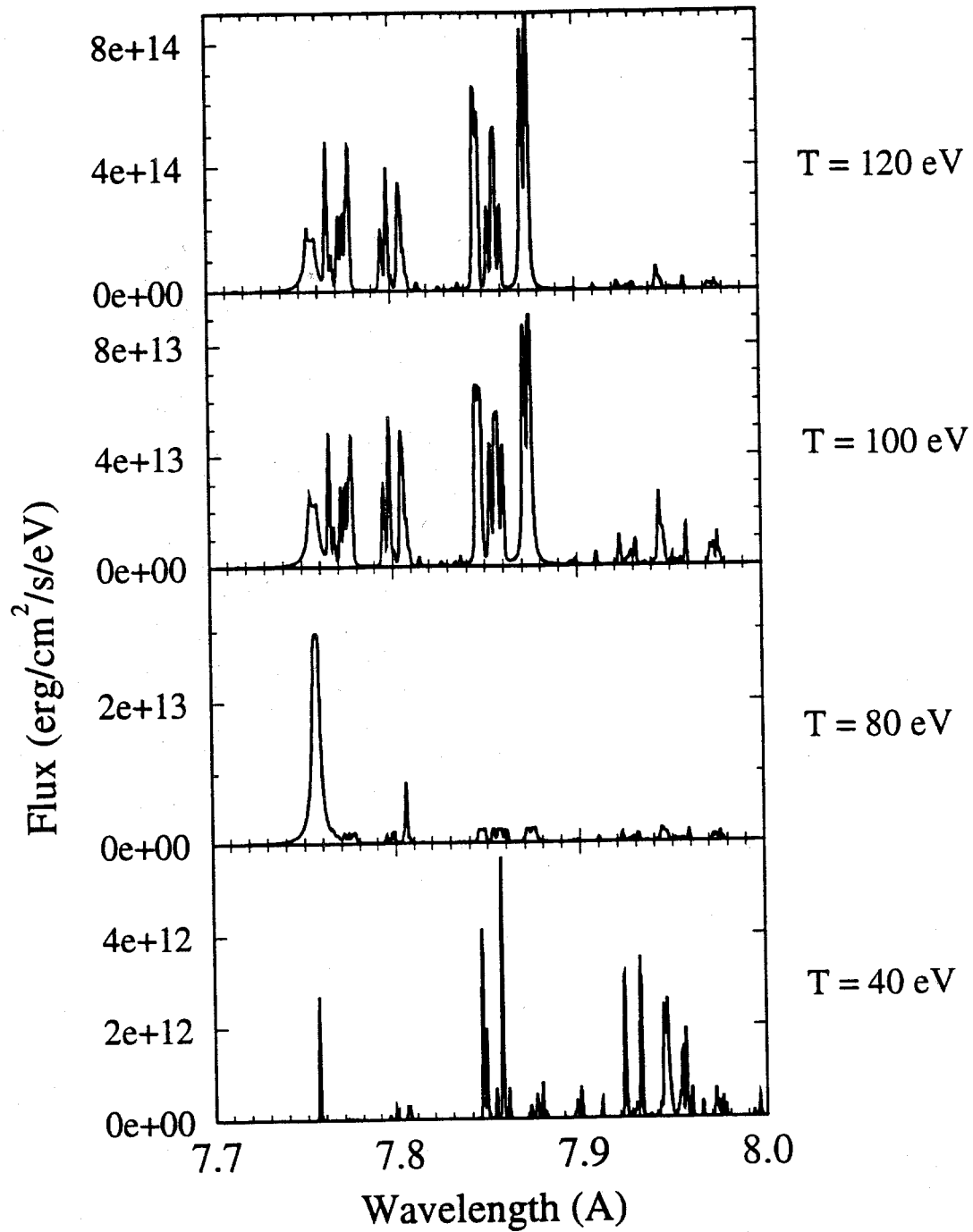


Figure 6.5. Calculated spectrum for Al at $T = 100 \text{ eV}$, $n = 10^{-3} n_{\text{solid}}$, and $\Delta L_{\text{orig}} = 2000 \text{ \AA}$.

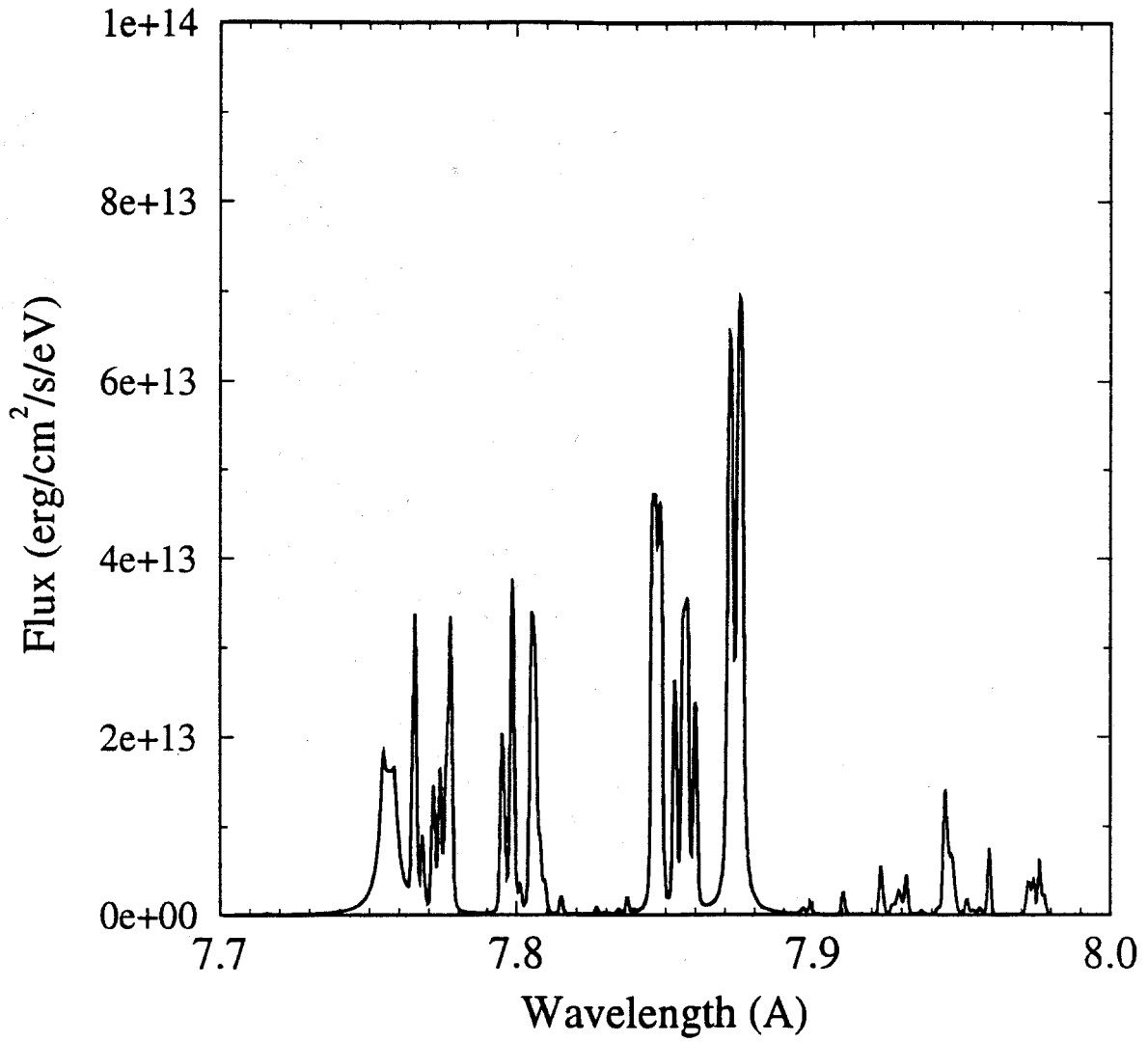


Figure 6.6. Experimental Al K-shell spectrum from a laser-produced plasma (from Ref. [2]).

energies $\gtrsim 1.4$ keV to electron capture into the $1s^1 2p^1 3\ell^1$ states. By simply integrating a Maxwellian distribution from 1.4 keV to infinity, one finds the fraction of electrons with energies > 1.4 keV is $\sim 10^{-6}$ for $T = 100$ eV and $\sim 10^{-15}$ for $T = 40$ eV.

Figure 6.7 shows results from CRE calculations at temperatures of $T = 40, 80, 100,$ and 120 eV. Note that at temperatures of 80 eV and below the M-shell satellites do not show any significant emission, while at $T \gtrsim 100$ eV the emission is much stronger. This suggests the possibility that the appearance of the feature at $\lambda = 7.77$ Å in the PBFA-II K_α satellite spectrum might be due to “hot” electrons: that is, at some location, at some time in the Al layer the number of electrons with energies $\gtrsim 1.4$ keV was characteristic of a Maxwellian plasma with a temperature of $\gtrsim 100$ eV. Thus, if produced by dielectronic recombination, two possible explanations of this feature are: (1) a small region of the Al target layer was heated to a temperature of ~ 100 eV; or (2) the temperature at all locations in the target was lower, but that the electron distribution is non-Maxwellian, with a “hot” component producing the electron capture events.

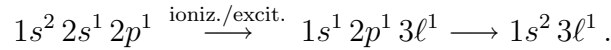
Another possible explanation of the appearance of the M-shell spectator satellite lines in the PBFA K_α spectra could be simultaneous ionization and excitation by the Li beam, or perhaps even by contaminants in the beam at late time. This is in some ways analogous to multiple ionization, which has been shown to be an important process in affecting the PBFA-II K_α spectra [3,4]. For instance, while He_α is produced by:



or



perhaps the M-shell spectator lines could be produced by:



Simultaneous beam-induced ionization-excitation processes are not included in our models because of the difficulties associated with computing reliable cross sections.

To conclude, in this section we have:

1. shown that significant emission from dielectronic recombination transitions could be observable for Al at temperatures $\gtrsim 100$ eV;
2. identified the transitions responsible for the emission feature observed just to the long-wavelength side of the Al He_α line;

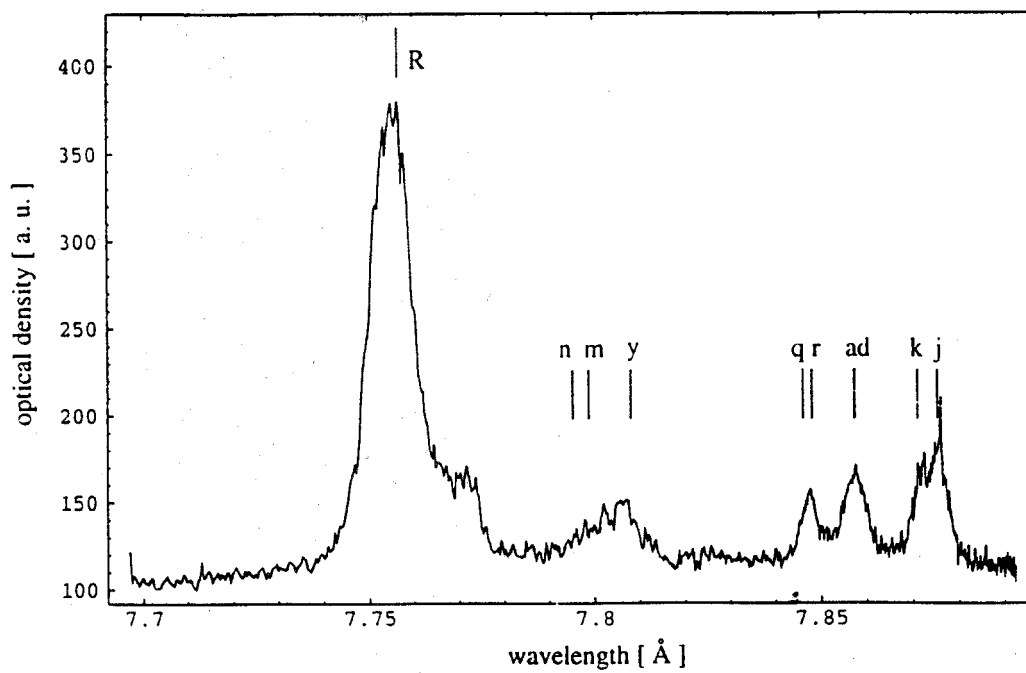


Figure 6.7. Calculated K_{α} spectra for $T = 40, 80, 100,$ and 120 eV. In each case $n = 10^{20}$ ions/cm³ and the original foil thickness was 2000 \AA .

3. discussed several possible explanations for the appearance of this feature in PBFA-II flat-foil experiments.

In regards to the last point, it is difficult with the existing set of data to determine definitively the reason for its appearance in PBFA-II experiments. However, it seems possible that in future PBFA-X experiments, perhaps with additional diagnostics (e.g., absorption spectroscopy), one might be able to determine the physical processes responsible for this feature.

6.3. Simulation of PBFA-II Experiments

In this section, we discuss results from the hydro simulations. In particular, we have focussed on the sensitivity of the Al plasma conditions and resultant K_α spectra to the Li beam conditions and radiation effects.

We have performed radiation-hydrodynamics simulations to study the effect of having a non-monoenergetic beam on heating the target. To do this, we take the beam parameters supplied to us by SNL; then at each timestep the ions are divided into several “bunches”. Results are shown in Figure 6.8 from a simulation in which the beam was divided into 3 components:

25% of the current with $V = 0.8 V_0(t)$

50% of the current with $V = 1.0 V_0(t)$

25% of the current with $V = 1.2 V_0(t)$,

where $V_0(t)$ is the time-dependent mean voltage. Note that using this model, the beam current and mean voltage are “conserved”. In Figure 6.8, two curves are shown for the Al temperature as a function of time, one from a calculation using a 3-component beam, the other from a calculation for a monoenergetic beam. Using a 3-component beam is seen to produce a slightly higher temperature than a monoenergetic beam (by $\sim 1 - 2$ eV). Thus, the low-V component more than compensates for the lower dE/dx of the higher-V components. This obviously is not a huge effect. If, however, the energy spread was larger than the 20% assumed above, the effect could become significant to the analysis.

Most of the recent calculations described below assume a 5-component beam with a smaller spread:

10% of the current with $V = 0.8 V_0(t)$

20% of the current with $V = 0.9 V_0(t)$

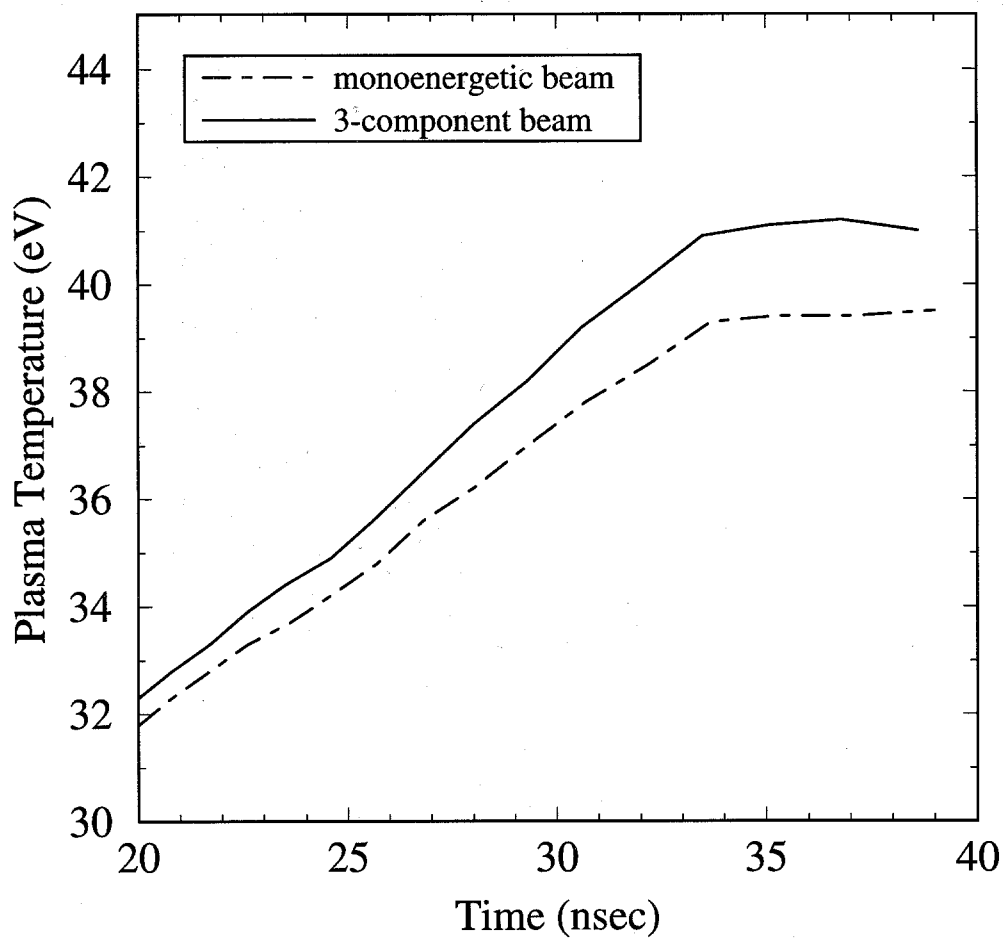


Figure 6.8. Comparison of calculated evolution of Al temperatures using a 3-component (i.e., 3 voltages) Li beam (solid curve) and a monoenergetic Li beam (dash-dotted curve).

40% of the current with $V = 1.0 V_0(t)$

20% of the current with $V = 1.1 V_0(t)$

10% of the current with $V = 1.2 V_0(t)$.

Figures 6.9 through 6.11 show results from several radiation-hydrodynamics simulations with and without CRE line transport. Figure 6.9 shows the mean temperature in each layer (CH/Au/Al/CH) as a function of time in two simulations: one in which lines were ignored (curves with circles), the other in which lines were transported using the CRE model. Note that the temperature in the Al layer drops significantly due to the addition of cooling by lines. Although the reduction of the line cooling rates due to the Au radiation field is included, this effect is small. At $t = 30$ ns (approximately the time during which the He/Li satellites form), the mean Al temperatures are 39 eV without line emission, and 33 eV when lines are included.

Figure 6.10 shows the mean Al temperature for a variety of simulations. The curves labeled “no mult” correspond to the curves shown on Figure 6.9. Two additional curves are shown for enhanced beam cases with CRE line transport: both labeled “w/ lines”. The “20% mult” refers to the current enhancement at $t = 10$ ns. This is a linearly increasing enhancement, so that the multiplier is 1.2 at 10 ns, 1.4 at 20 ns, 1.6 at 30 ns,.... Note that Al temperature for this case exceeds all other cases. This enhancement probably produces too much He/Li K_α emission. The curve labeled 15% is probably more consistent with the observed spectra. So one question is: is a beam which is enhanced by 1.3 at $t = 20$ ns, and 1.45 at $t = 30$ ns inconsistent with the experimental ion beam diagnostics?

Figures 6.11 through 6.13 show the time-dependent beam parameters used for the nominal, 15% enhancement, and 20% enhancement cases. Again, a key question in the analysis is what is the uncertainty in the beam data at $t \sim 20 - 30$ ns.

To summarize, when using the nominal beam data, our best radiative models, and the “standard” stopping power model, we get a synthetic spectrum which will produce the He- and Li-like K_α satellite intensities which are lower than those observed for Shot 5851. Possible sources of error include:

A) the beam data at late times;

B) uncertainties in dE/dx ; either for Au or Al. The Al dE/dx would probably have to be $\sim 30\%$ higher than the values predicted by both the Mehlhorn [5] and Wang and Mehlhorn [6] models. Alternatively, if the gold dE/dx was larger, the voltage of the ions in the Al would be lower and the Al dE/dx would be higher.

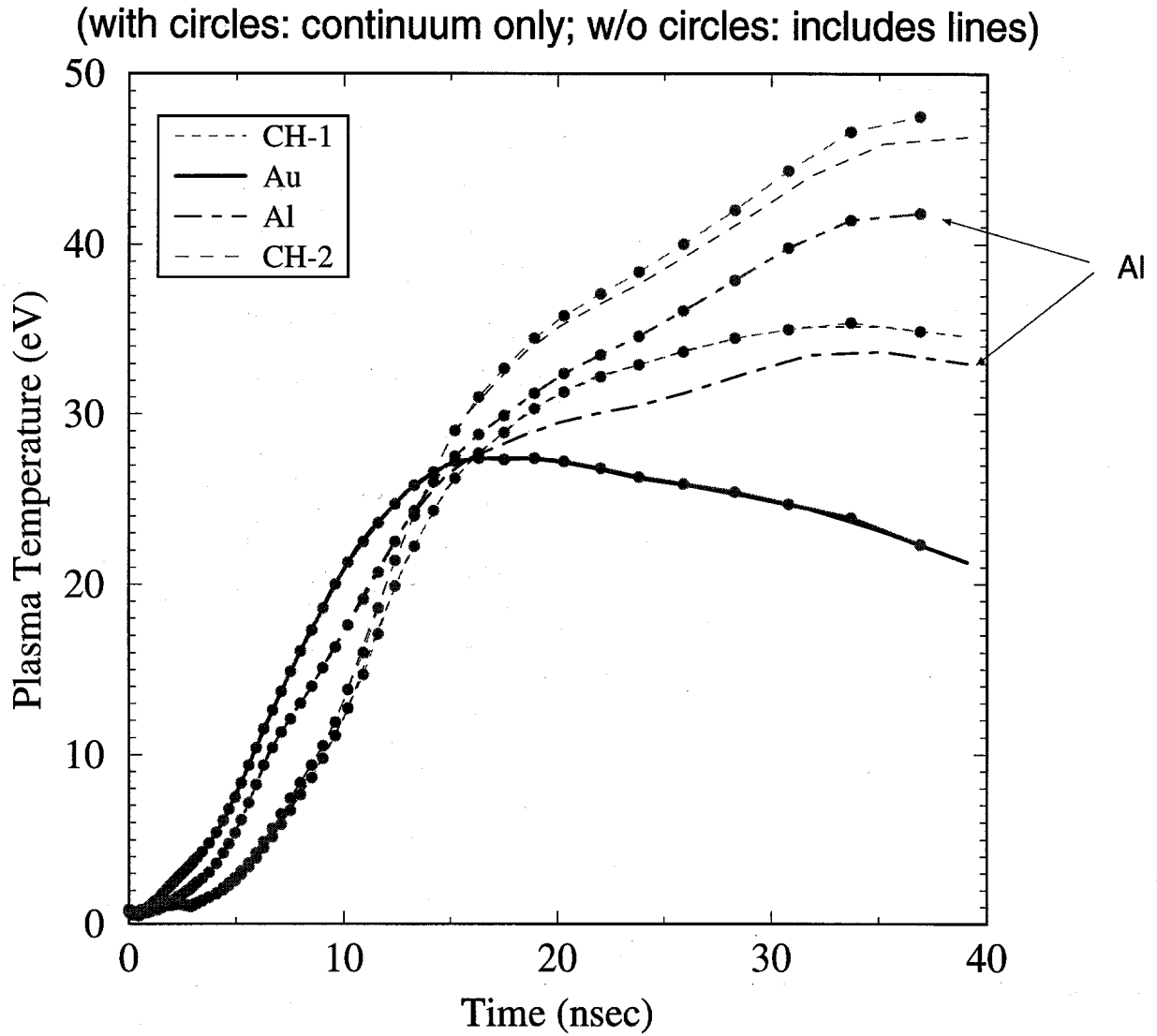


Figure 6.9. Comparison of mean temperatures in CH/Au/Al/CH target regions calculated using radiation model with continuum opacities and emissivities only (curves with circles), and a model which includes detailed line radiation transport (curves without circles).

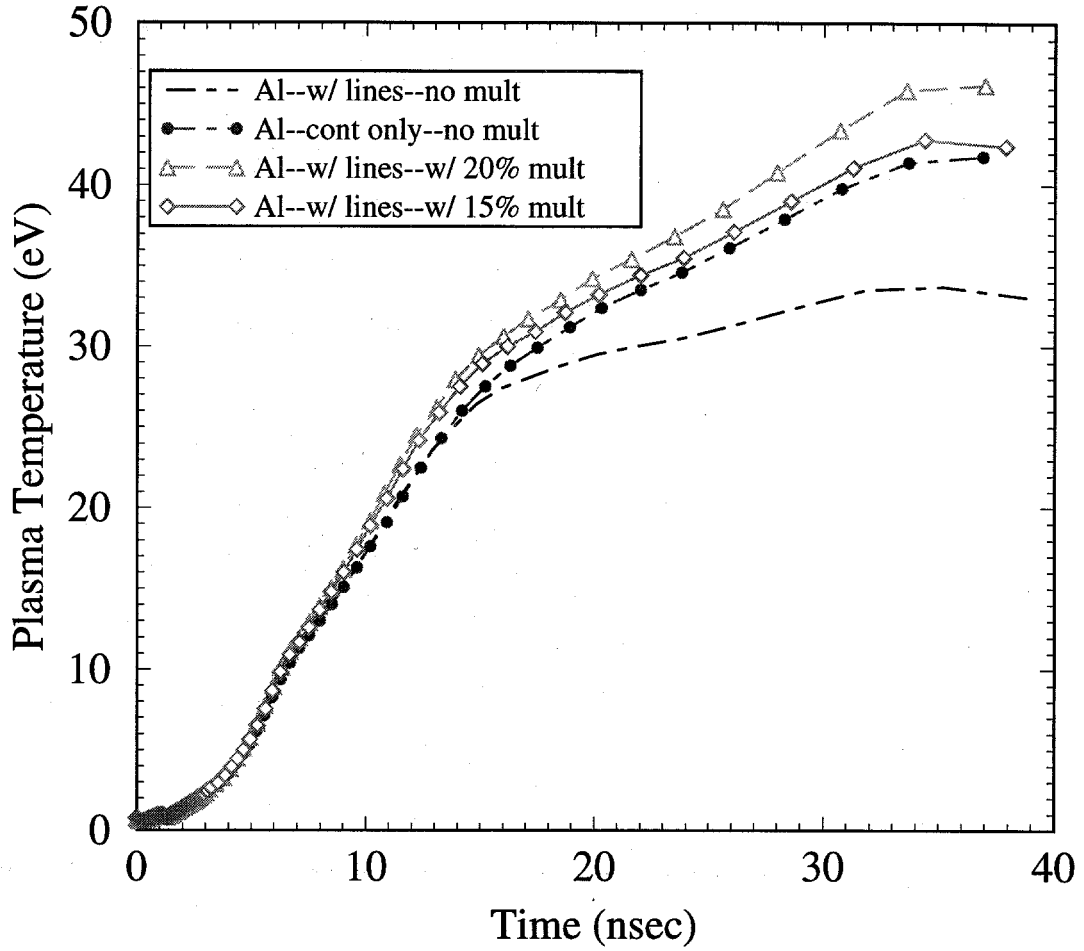


Figure 6.10. Evolution of mean temperature in Al layer for different radiation and beam models. Refer to text for explanation of curves.

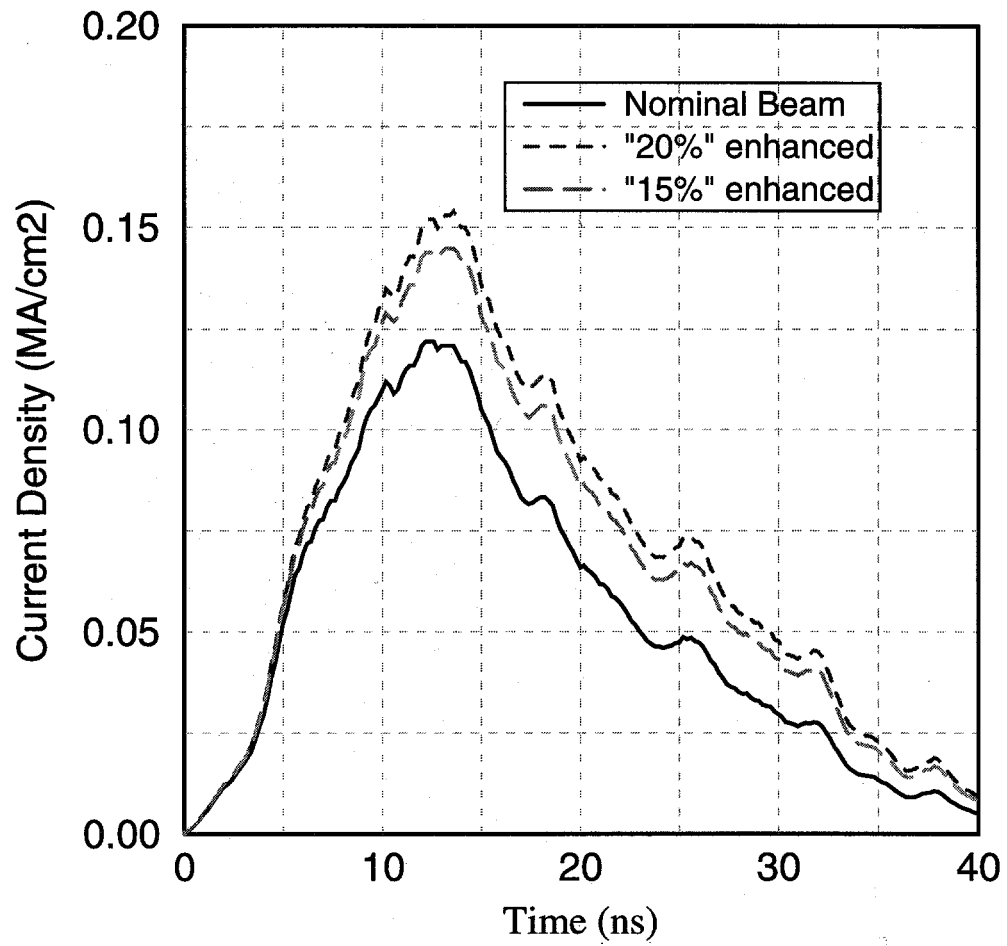


Figure 6.11. Time-dependent Li beam current densities on target used in radiation-hydrodynamics simulations.

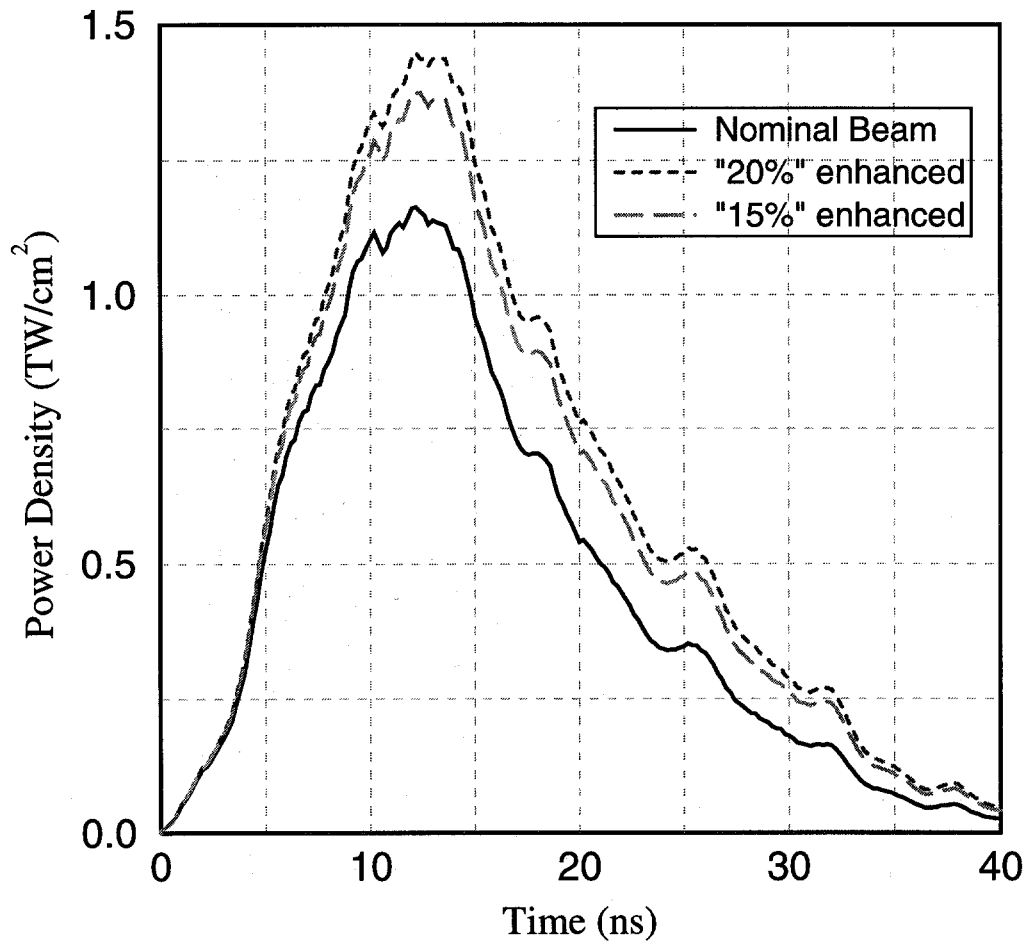


Figure 6.12. Time-dependent Li beam power densities on target used in radiation-hydrodynamics simulations.

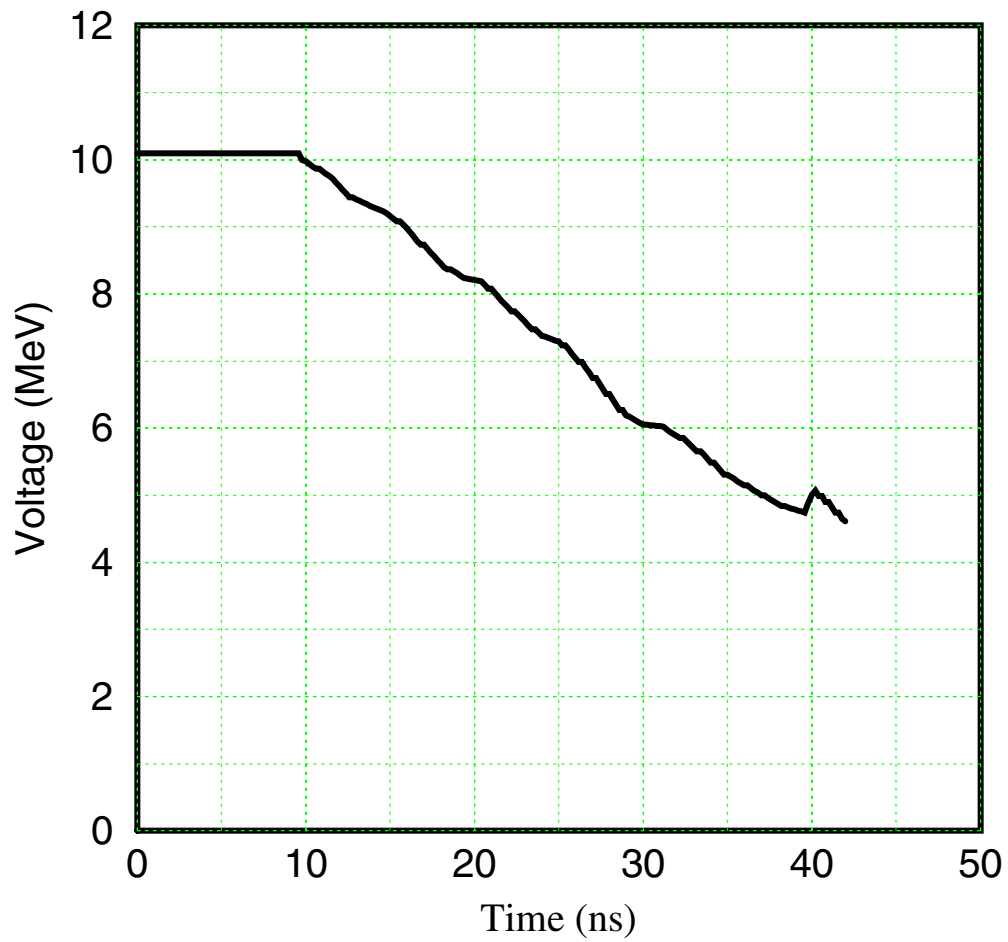


Figure 6.13. Time-dependent Li beam voltage on target used in radiation-hydrodynamics simulations.

C) 2-D effects: If the densities were lower than what is predicted by the 1-D hydro calculations, the radiative cooling could change significantly. From looking at the different 1-D hydro calculations for the different (A, B, C, D, E) spatial regions, the thickness of the Al at $t = 30$ ns is:

A: 0.93 mm

B: 0.83 mm

C: 0.78 mm

D: 0.66 mm

E: 0.40 mm.

That is, the Al moves ~ 1 mm. But because the beam spot size is ~ 8 mm one could argue that this would be a $\lesssim 10 - 15\%$ effect.

D) Non-uniformities in the beam. If there were non-uniformities in the beam which were small compared to the spatial resolution of the detector, one could get localized hot regions. Again, the beam would have to be enhanced several tens of percent for this to be a contributor.

Figures 6.14–6.17 show time-integrated K_α spectra computed for PBFA-II Shot 5851 using 4 beam intensities. In these simulations we used the beam parameters sent to UW by Tom Hail [7]. The calculated spectra are obtained first by running radiation-hydrodynamics simulations for a given set of Li beam parameters, and then performing CRE calculations using the temperature, density, Li voltage, and Li current density distributions in the Al layer at 3 ns time intervals. Note that using the “nominal” beam intensities (Fig. 6.14), the calculated Al K_α spectrum shows relatively weak emission for He_α ($\lambda = 7.76$ Å) and the Li-like satellites ($\lambda \approx 7.85$ Å). This is weaker than observed for PBFA-II shots 5851, 5846, and 6347. (The observed spectrum for 5851 is shown in Figure 6.18.)

Figures 6.15 through 6.17 show simulated K_α spectra for enhanced beam intensities. Here, we simply multiplied the nominal beam current density used in the rad-hydro simulations by some factor (1.25, 1.5, and 2.0). This obviously results in higher temperatures in the target, which in turn shows up in the synthetic time-integrated spectra as higher intensities for the satellites of relatively high ionization stages. Note that when using a multiplier of 1.25 (Figure 6.15) that the overall agreement with the experimental spectrum is good. Given the uncertainties in the actual beam conditions, these results

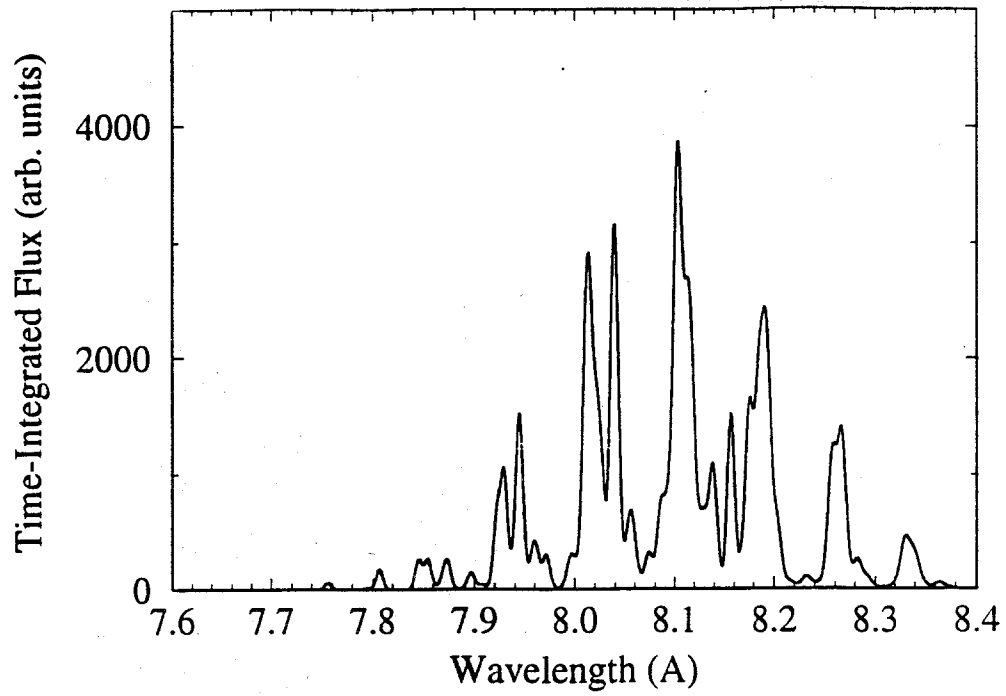


Figure 6.14. Time-integrated Al K_{α} satellite spectrum calculated using “nominal” Li beam intensity.

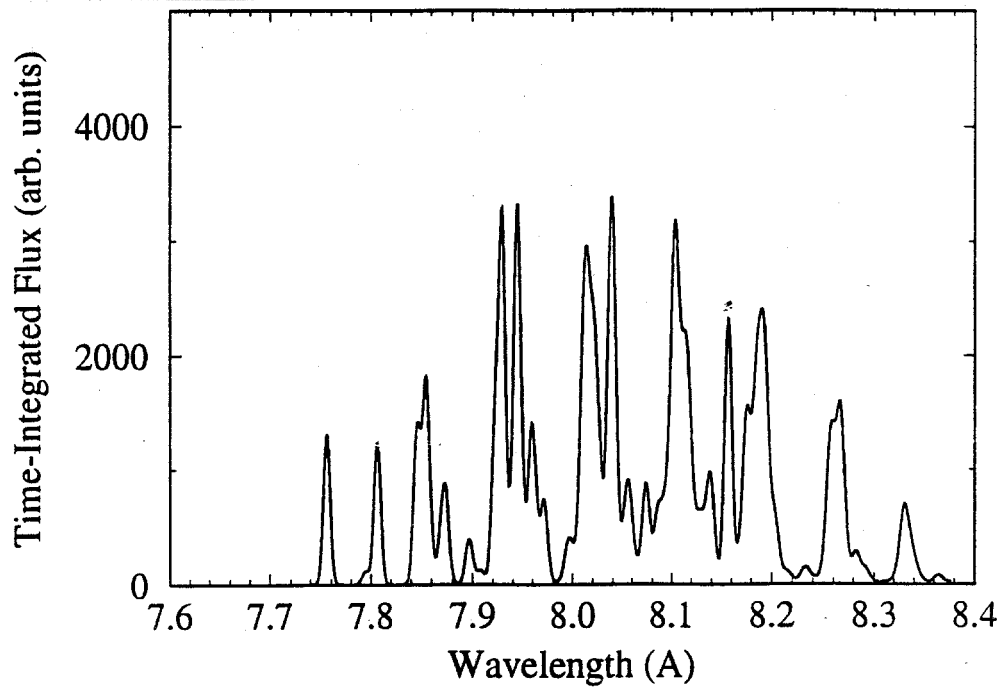


Figure 6.15. Same as Figure 6.14, but with Li beam current density enhanced by a factor of 1.25.

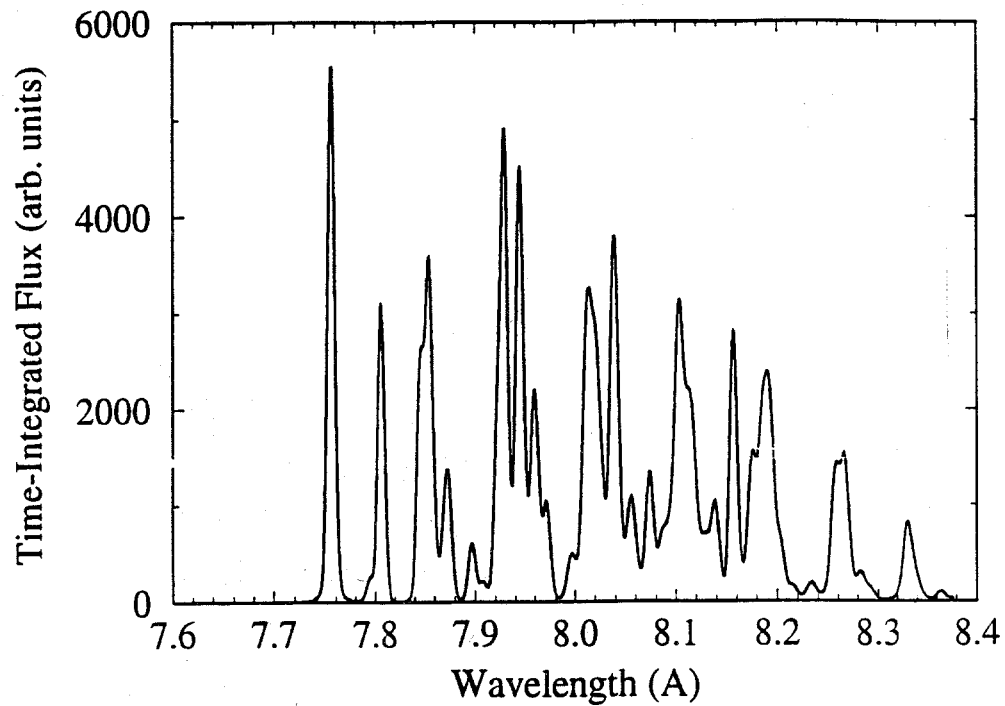


Figure 6.16. Same as Figure 6.14, but with Li beam current density enhanced by a factor of 1.5.

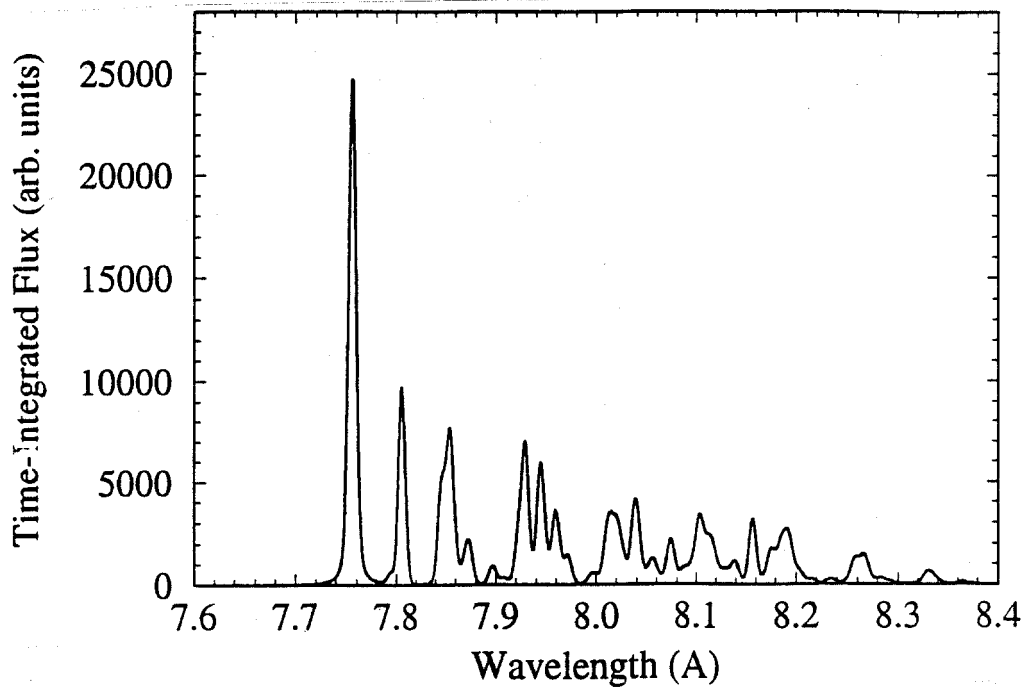


Figure 6.17. Same as Figure 6.14, but with Li beam current density enhanced by a factor of 2.0.

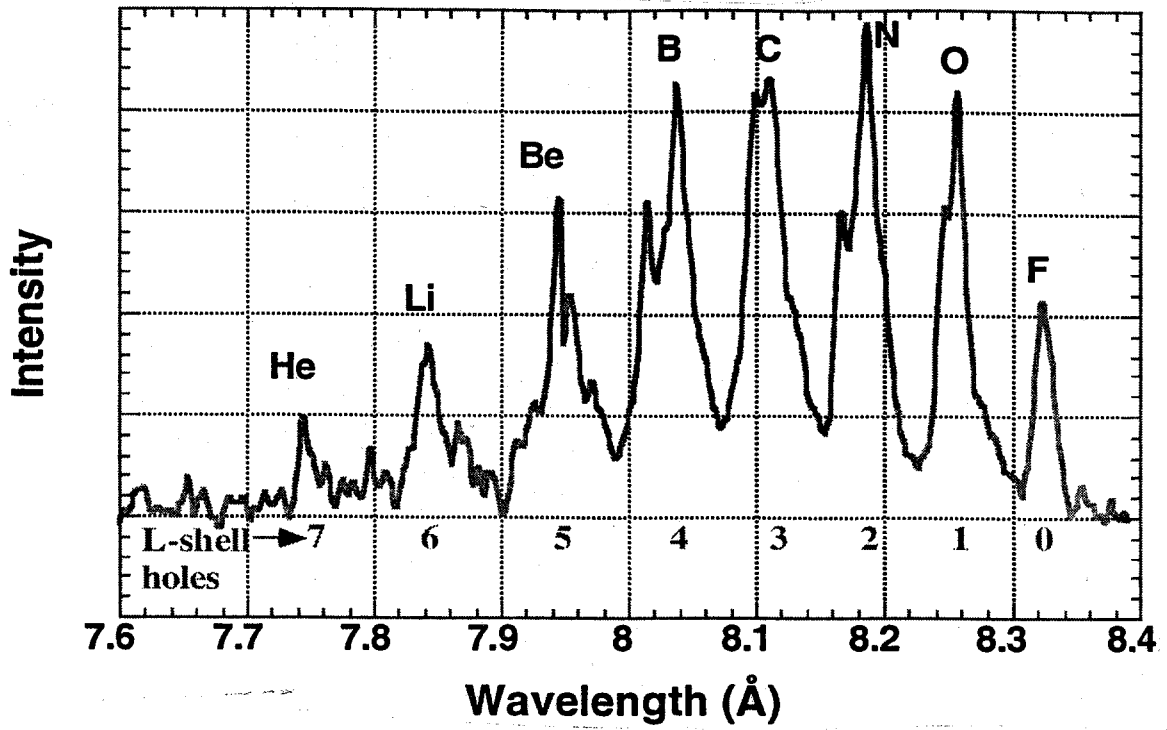


Figure 6.18. Experimental time-integrated Al K α satellite spectrum for Shot 5851.

suggest a reasonably good overall understanding of the target heating, as well as the atomic processes which influence the spectrum.

Figures 6.16 and 6.17 show synthetic time-integrated K_α spectra for Li beam current density multipliers of 1.5 and 2.0. In these cases the He- and Li-like emission ($\lambda \approx 7.75 - 7.90 \text{ \AA}$) is significantly stronger than that of the satellites of the lower ionization stages, which is not at all in agreement with the experimental spectra.

To conclude, although the agreement between simulation and the data is not perfect, a good understanding of the physical processes which affect the resulting spectra has been achieved. It appears that the beam data needs to be accurately diagnosed throughout the entire pulse to constrain the problem. On the other hand, one could turn the problem around to use K_α data to constrain the beam.

6.4. Absolute Flux Estimate for K_α Satellites

In this section we estimate the absolute K_α flux from the Al layer in PBFA-II experiments. In our analysis, fluxes are calculated using the short characteristics model (integral radiation transport). Results from NLTERT (CRE) are in units of $\text{erg}/\text{cm}^2/\text{s}/\text{eV}$. Time-dependent NLTERT results are then post-processed to do time-integration and add instrumental response ($\lambda/\Delta\lambda$ is typically ~ 1000). Checks are performed on energy/flux conservation in the post-processing to make sure we do not “lose photons.” Units at the end of the time-integration post-processor are $\text{erg}/\text{cm}^2/\text{eV}$. All results are into 2π , as the K_α spectra are for planar targets. The flux is out of the Al surface adjacent to the CH tamper (not the Au-facing side).

The time-integrated results for the 4 series of calculations (J_B multiplier = 0.98, 0.82, 0.51, and 0.11) are then “space-integrated using the areal weights suggested by J. Bailey:

	Shots 5846, 51,81	Shot 6347
J_B multiplier	Areal Weight (cm^2)	Areal Weight (cm^2)
0.98	0.031	0.031
0.82	0.204	0.097
0.51	0.183	0.090
0.11	0.417	0.173

The flux at the end of the space-integration calculation is in erg/eV , again into 2π .

Typically, we get numbers like:

$$F_{\max} \sim 1000 \text{ erg/eV for } C, N \text{ ions .}$$

For C and N , integrating in frequency we get

$$F = 4 \times 10^3 \text{ erg into } 2\pi$$
$$\Rightarrow \frac{1.7 \times 10^{12} \text{ photons}}{2\pi} = \boxed{2.6 \times 10^{11} \text{ photons/steradian}}$$

One could imagine this could be off by a factor of several tens of percent due to geometry (2-D) effects, cross sections, etc. But it is likely to be accurate to within a factor of 2.

References for Section 6

1. Duston, D., and Davis, J., *Phys. Rev.* **A21**, 1664 (1980).
2. Renner, O., et al., *Laser and Particle Beams* **12**, 539 (1994).
3. Wang, P., MacFarlane, J.J., and Moses, G.A., *Laser and Particle Beams* **13**, 191 (1995).
4. MacFarlane, J.J., Wang, P., Bailey, J.E., Mehlhorn, T.A., and Dukart, R.J., *Laser and Particle Beams*, **13**, 231 (1995).
5. Mehlhorn, T.A., *J. Appl. Phys.* **52**, 6522 (1981).
6. Wang, P., and Mehlhorn, T.A., see Section 5 of this report.
7. Hail, T.A., private communication (1995).